

Dynamical Mean Field Theory
of
inhomogeneous correlated systems



Inaugural-Dissertation
zur Erlangung des Doktorgrades der
Mathematisch–Naturwissenschaftlichen Fakultät
der Universität zu Köln

vorgelegt von

Rolf Helmes

aus Siegen

Köln 2008

Berichterstatter: Prof. Dr. Achim Rosch
Prof. Dr. Matthias Vojta

Tag der mündlichen Prüfung: 14.01.2008

Abstract

In the last one and a half decade, the Dynamical Mean Field Theory (DMFT) allowed to get insight into the Mott metal-insulator transition (MMIT) and many long-standing questions about the nature of the transition could be answered, at least in the limit of infinite dimensions. In this thesis, the adaption of the DMFT to inhomogeneous systems is studied, opening the possibility to study a rich variety of systems and challenging physical questions. Firstly, the basic problem is studied, how a metal penetrates into a Mott insulator, where analytically found power-laws at the critical point can be confirmed with numerics. Secondly, the phase separation between metal and insulator is investigated, which can occur since the MMIT is a first order transition. The spontaneous build up of domains is observed in numerical simulations and the domain walls are examined. Finally, the MMIT of fermionic atoms in an optical lattice is studied.

Kurzzusammenfassung

Die Dynamical Mean Field Theory (DMFT) hat in den letzten 15 Jahren einen Einblick in den Mott-Metal-Isolator Übergang (MMIT) ermöglicht, und viele lang ausstehende Fragen über die Art des Übergangs konnten beantwortet werden, zumindest im Limes von unendlich vielen Dimensionen. In dieser Arbeit wird die Adaption der DMFT auf inhomogene Systeme untersucht. Dies eröffnet die Möglichkeit, eine Reihe an interessanten physikalischen Fragestellungen zu bearbeiten. Zunächst wird das grundlegende Problem untersucht, wie ein Metall in einen Mott-Isolator eindringt, wobei analytisch gefundene Potenzgesetze am kritischen Punkt numerisch bestätigt werden können. Anschließend wird die Phasenseparierung zwischen Metall und Isolator studiert, die aufgrund der Natur des MMIT als Übergang erster Ordnung auftreten können. Die spontane Ausbildung von Domänen wird in numerischen Simulationen beobachtet und die Domänenwände werden analysiert. Schließlich wird der MMIT von fermionischen Atomen in einem optischen Gitter untersucht.

Contents

1	Introduction	7
2	Model and Method	11
2.1	The Hubbard model	11
2.2	Dynamical Mean-Field Theory (DMFT)	13
2.2.1	Method	13
2.2.2	Results	16
2.3	Dynamical Mean-Field Theory for inhomogeneous systems	19
2.4	Impurity solvers	24
2.4.1	Iterated Perturbation Theory (IPT)	24
2.4.2	Numerical Renormalization Group	30
3	Heterostructures	37
3.1	Inhomogeneous DMFT for a layer structure	38
3.2	Analytical Study of the Heterostructure	41
3.2.1	Simplified DMFT equations: Landau equation for the quasi-particle weight	41
3.2.2	Application of the simplified DMFT to the Heterostructure	43
3.2.3	Results	46
3.3	DMFT/NRG results	51
4	Phase separation	57
4.1	Maxwell construction for first order phase transitions	58
4.1.1	Fluid-gas transition	58
4.1.2	Mott transition away from half filling	60
4.2	Microphase separation	63
5	Metal-Insulator Transition in Optical Lattices	71
5.1	Experimental Background: Optical Lattices	71
5.2	Group Theory of the Cubic Lattice	74
5.3	Mott metal-insulator transition in an optical lattice	79
	Bibliography	93

Danksagung

97

Chapter 1

Introduction

The fermionic Mott transition at temperature $T = 0$ is simple to explain on a very basic level. It is the consequence of the competition of the two parts of the fermionic Hubbard model. One part describes the hopping of fermions – let us consider spin-1/2 electrons – on a lattice. Focusing on three dimensions and pushing aside issues like superconductivity or nesting, one can identify the eigenstates of the hopping term as a Fermi liquid, i.e. a metal. The second part of the Hubbard Hamiltonian accounts for the on-site repulsion U of two electrons with opposite spin on the same site. Allowing only for a uniform hopping t and restricting the system to be half filled, it is intuitively clear that upon increasing U/t a transition from the Fermi liquid to an insulating state must occur. For $U/t \gg 1$, the on-site repulsion suppresses the hopping and one obtains the Mott insulator.

Regarding the transition at finite temperatures $T > 0$, the situation becomes more complex. In contrast to $T = 0$, no clear differentiation between the metal and the insulator is possible. However, if one considers phases at temperatures T sufficiently below the critical temperature T_c of the second order end point and close to the transition line, one can clearly distinguish between two different thermodynamic phases, a “bad metal” and a “bad insulator”. The “bad insulating” state is thermally activated and has a finite density of states at the chemical potential. In this thesis we will be rather sloppy and refer to the “bad metal” as “metal” and to the “bad insulator” as “Mott insulator”. Here, a too intuitive picture might be misleading. The concept of the Mott insulator as a half-filled lattice, where the isolated electrons are localized since the cost U of hopping to an occupied neighboring site is too high, is too naive and neglects the strongly correlated nature of the state. If this concept proved true, adding a single electron to the Mott-insulator would result in the metallic state, since the electron could move freely on top of the other electrons. At $T > 0$, this concept is oversimplified. The statistic ensemble of the Mott-insulating state always contains double occupied sites, yet it can clearly be distinguished from a thermodynamically different metallic state. Furthermore, at $T > 0$, the Mott insulator is stable against a small doping.

From this discussion one already realizes that rich and interesting physics appears from the innocent looking Hubbard model, which is the prime example and also the minimal model for materials where strong correlations play a role. In three dimensions, no exact

analytic method exists to describe the Mott transition. In the late 1980s and early 90s the Dynamical Mean Field Theory (DMFT) was developed which is able to analyze the transition in the approximation of neglecting spatial fluctuations. The method becomes exact in the limit of infinite dimensions d . In analogy to the Weiss mean-field theory of the Ising model, the DMFT singles out one site of the lattice and absorbs all other sites into a non-interacting bath coupled to the considered site. While in the Weiss mean-field theory the bath is described by a single parameter, the effective magnetic field, the bath in the DMFT is described by a frequency-dependent bath function which represents an effective density of states for an electron tunneling out of the single considered site. Thereby dynamic processes as electrons tunneling away and back to sites are captured by the DMFT. The effective model is the Anderson impurity model, consisting of an impurity – the singled out site – which is coupled to a non-interacting bath. The DMFT was able to elucidate the transition for $d = \infty$. For the paramagnetic case where magnetic ordering is neglected, the Mott transition turns out to be a first order transition, which has two second order endpoints: one at $T = 0$ and one at critical temperature $T = T_c$. The resulting phase diagram is artificial. Regarding generic materials, below a certain critical temperature the system will pass over into an antiferromagnetic ordered Mott insulator below the Neel temperature T_N . However, T_N can be lowered by frustrating the lattice which suppresses the magnetic ordering.

Let us return to the question raised above: how does a Mott insulator react to adding electrons, i.e. doping? The issue was only settled recently for a uniform system in the DMFT approximation and neglectation of Coulomb forces, see Chapter 4. At $0 < T < T_c$ and increasing doping, the system passes through the first order phase transition at a critical chemical potential μ_c , displaying the typical physics of phase separation. Since particle-hole symmetry is broken by finite doping, the metallic and the insulating phase have different fillings. Thus a macroscopic separation of domains is impeded by the Coulomb force. To treat the possible scenario of a microphase separation in Chapter 4, the usual DMFT method needs to be generalized to treat inhomogeneous systems, as explained in Chapter 2. In contrast to the homogeneous DMFT, where all sites are assumed to be in the same state, in the inhomogeneous case the sites of the lattice are intrinsically different, resulting in different bath functions for different sites. Thus many instead of one Anderson impurity models need to be solved.

The idea of neighboring metallic and insulating domains raises the very basic question of how a metal penetrates into a Mott insulator. Considering an explicit inhomogeneous system consisting of a metal with $U_{\text{met}} < U_c$ and a Mott insulator with $U_{\text{ins}} > U_c$, where U_c is the critical interaction for a given hopping t , the behavior of the system close to the junction has not been clarified so far. In Chapter 3, we investigate this problem. We find that the relevant energy scales in the Mott insulator are the coupling $J \propto t^2/U$ of the spins of the localized electrons, which competes with the quasi-particle weight Z of the penetrating metal, corresponding to the Kondo temperature T_K in the impurity model. Since we neglect magnetic order and regard a paramagnetic system with $J = 0$, we find that the metal penetrates infinitely deep into the Mott insulator. By varying the interaction U_{ins} and the temperature T , we study the universal scaling behavior around the second

order end point $U_{\text{ins}} = U_c$ and $T = 0$.

In Chapter 5, the Mott transition of fermionic atoms in an optical lattice is studied. In order to confine the atoms, an external potential is needed which makes the problem inhomogeneous. Naturally the occupation vanishes approaching the border of the trap. Hence the bordering regions can be conceived as a strongly doped material and are certainly metallic. Depending on the depth of the trap, the center will be double occupied and band insulating. The band insulator will be surrounded by a strongly doped metallic region. If the on-site interaction is strong enough, a half-filled Mott-insulating region appears between the two metallic regions. Here the issue discussed in Chapter 3 is very relevant: since the metallic regions penetrate into the insulating regions, the results presented in Chapter 5 differ considerably from calculations done in a local density approximation, a method widely used in the literature.

Chapter 2

Model and Method

2.1 The Hubbard model

The physics of electrons in a solid is described by the general Hamiltonian $\mathcal{H} = \mathcal{H}_0 + \mathcal{H}_{ee}$ [1,2], where

$$\begin{aligned}\mathcal{H}_0 &= \int d^d r a_\sigma^\dagger(\mathbf{r}) \left[\frac{\hat{\mathbf{p}}^2}{2m} + V(\mathbf{r}) \right] a_\sigma(\mathbf{r}), \\ \mathcal{H}_{ee} &= \frac{1}{2} \int d^d r d^d r' V_{ee}(\mathbf{r} - \mathbf{r}') a_\sigma^\dagger(\mathbf{r}) a_{\sigma'}^\dagger(\mathbf{r}') a_{\sigma'}(\mathbf{r}') a_\sigma(\mathbf{r}).\end{aligned}\tag{2.1}$$

Here, the degrees of freedom of the ions of the lattice have been neglected and the interaction of the ions with the electrons has been simplified by introducing an effective lattice potential $V(\mathbf{r})$. The first part \mathcal{H}_0 describes the one-particle physics of electrons moving in the lattice potential while \mathcal{H}_{ee} describes their interaction via the Coulomb force. Despite its innocent appearance, the Hamiltonian 2.1 describes an abundance of solid state physics phenomena. Unfortunately, it is impossible to make further progress without simplifying it by making further approximations. For many materials, the following approach is very successful. Using the density functional theory [3] combined with the local density approximation (LDA), one can absorb the ionic potential $V(\mathbf{r})$ and the electron-electron Coulomb interaction \mathcal{H}_{ee} into an effective potential v_{eff} , arriving at the Kohn-Shahn equation, a one-particle Schrödinger equation for the electrons,

$$\mathcal{H}_{\text{eff}} \phi_j(\mathbf{r}) = \left(-\frac{\nabla^2}{2m} + V_{\text{eff}}(\mathbf{r}) \right) \phi_j(\mathbf{r}) = \varepsilon_j \phi_j(\mathbf{r}).\tag{2.2}$$

Here $\phi_j(\mathbf{r})$ is a complete basis set of one-particle states. By Fourier transforming to \mathbf{k} -space one obtains the band-dispersion $\epsilon_{\mathbf{k}}$ of the electrons. Then \mathcal{H}_{eff} takes the form $\sum_{\mathbf{k}} \epsilon_{\mathbf{k}} c_{\mathbf{k}\sigma}^\dagger c_{\mathbf{k}\sigma}$. If one rewrites \mathcal{H}_0 in the Wannier state basis,

$$|\psi_{\mathbf{R}n}\rangle \equiv \frac{1}{\sqrt{N_{\text{sites}}}} \sum_{\mathbf{G} \in B.Z.} e^{-i\mathbf{G}\cdot\mathbf{R}} |\psi_{\mathbf{k}n}\rangle,\tag{2.3}$$

one obtains

$$\mathcal{H}_{\text{eff}} = \sum_{i,i'} t_{ii'} c_{i\sigma}^\dagger c_{i'\sigma}, \quad (2.4)$$

where $t_{ii'} = \frac{1}{N_{\text{sites}}} \sum_{\mathbf{k}} e^{i\mathbf{k}(\mathbf{R}_i - \mathbf{R}_{i'})} \epsilon_{\mathbf{k}}$ and N_{sites} is the number of sites in the lattice. Here we consider only a single band and neglect all others, thus we have dropped the band index. This Hamiltonian has the simple interpretation of electrons hopping between lattice sites, where $t_{ii'}$ is the amplitude for hopping between the lattice sites i and i' .

For materials where the true electron-electron interactions play an important role, the approach above is insufficient and needs to be extended. In 1963, Hubbard, Gutzwiller and Kanamori introduced the celebrated fermionic Hubbard model [4–6],

$$\mathcal{H} - \mu \hat{N} = -\mu \sum_{i,\sigma} c_{i,\sigma}^\dagger c_{i,\sigma} + \sum_{\langle i,j \rangle, \sigma} t_{ij} c_{i,\sigma}^\dagger c_{j,\sigma} + U \sum_i n_{i,\uparrow} n_{i,\downarrow}, \quad (2.5)$$

where we have introduced the chemical potential μ and the particle number operator \hat{N} . Here the interaction term $U n_{i,\uparrow} n_{i,\downarrow} = U c_{i,\sigma}^\dagger c_{i,\sigma}^\dagger c_{j,\sigma} c_{j,\sigma}$ has been introduced to model the Coulomb repulsion of two electrons on the same site. The Hubbard model is the prime example and also the minimal model for highly correlated electrons on a lattice. By “correlated” one does not refer to the usual symmetry correlations of fermions but to correlations between the electrons caused by the interaction term, which is crucial for the displayed physics of the model. In the following we will only consider lattices with dimensions higher than one, since physics in one dimension exhibits many peculiarities compared to physics in higher dimensions (Fermi-liquid theory is not applicable and replaced by Luttinger liquid theory, including spin-charge separation, etc.). At $U/t = 0$ the Hubbard model describes a metal with independent Bloch electrons moving in a band determined by the dispersion $\epsilon_{\mathbf{k}} = \sum_{i,j} e^{i\mathbf{k}(\mathbf{R}_i - \mathbf{R}_j)} t_{ij}$. This in principle easy problem might get more complicated if one desires to describe materials where band structure calculations are necessary to compute the dispersion $\epsilon_{\mathbf{k}}$. However, here we will make the further simplification of assuming a uniform hopping, $t_{ij} \equiv t$, and consider simple lattices where the dispersion can be calculated analytically. The Hubbard model studied in this thesis thus takes the form

$$\mathcal{H} = t \sum_{\langle i,j \rangle, \sigma} c_{i,\sigma}^\dagger c_{j,\sigma} + U \sum_i n_{i,\uparrow} n_{i,\downarrow}. \quad (2.6)$$

If nesting is neglected and assuming that one is far from instabilities like superconductivity, for small $U/t \ll 1$ the free electrons are renormalized according to Fermi liquid theory developed by Landau in 1956-58, see, e.g. Ref. [7, 8]. In the other limit, i.e. $U/t \gg 1$ and in the case of a lattice with half filling $n = 1/2$, the Hubbard model describes the so-called Mott insulator as hopping is suppressed by the large Coulomb repulsion of the electrons [9]. The only degrees of freedom left are the spins of the electrons at each site and the Hubbard model can be mapped to the Heisenberg model,

$$\mathcal{H}_{\text{Heisenberg}} = J \sum_{\langle i,j \rangle} \hat{\mathbf{S}}_i \cdot \hat{\mathbf{S}}_j, \quad (2.7)$$

with $J \propto t^2/U$ [2]. This is a problem of quantum magnetism, where spin wave theory can be applied around the anti-ferromagnetic ground state. Thus for both limits $U/t \ll 1$ and $U/t \gg 1$ theories and methods exist to describe the Hubbard model. However, we already see that at some intermediate interaction a transition from metal to insulator, termed 'Mott-Hubbard metal-insulator transition', must occur. So far, an analytical method to describe this transition is not in sight and the best way to tackle the physics of the transition is a numerical method called 'Dynamical Mean Field Theory' which will be described in the next section.

In Chapters 3 and 4 we will be concerned with two physical problems motivated by experiments with highly correlated electrons, which can be described by the Hubbard model. Chapter 5 deals with a completely different physical scenario, optical lattices. Here, the Hubbard model is realized by fermionic atoms confined in an optical lattice, see Section 5.1.

2.2 Dynamical Mean-Field Theory (DMFT)

2.2.1 Method

As mentioned above, an analytic solution for the Hubbard model (2.6) is out of sight and one has to retreat to numerical methods to investigate the Mott-Hubbard metal-insulator transition. A breakthrough has been achieved with the 'Dynamical Mean Field Theory' (DMFT), which is able to resolve the first order transition from metal to insulator, see Fig. 2.1 for the case of a half-filled lattice. In the following we will only consider paramagnetic solutions and any magnetic order will be neglected. This can either be seen as a crude approximation calling for redemption at a later stage of the theory or one could argue that one regards a completely frustrated lattice. We will therefore drop the spin indices of the Green's functions. The DMFT method and its approximations will shortly be described in this section.

The DMFT was developed in the late 1980s and early 1990s. Pioneering work was done by Metzner and Vollhardt [11] and Müller-Hartmann [12–14]. Further development was made by Georges and Kotliar [15] and Jarrell [16]. For a comprehensive review see Ref. [10]. Let us start presenting the DMFT by shortly sketching the idea, presented in Fig. 2.2: in the interacting lattice, one site is singled out and all other sites are mapped into a bath. Thus the lattice model is mapped to an "impurity" model, consisting out of one single interacting site ("impurity"), which is coupled to the non-interacting bath. By solving the impurity model, one obtains the state of the single site. Assuming a translational invariant lattice, the state of the single site is now assumed to hold for all sites, thus defining the state of the lattice. The procedure is repeated until a self-consistent solution is reached.

The Hubbard model, the lattice model considered in this thesis, will be mapped to an Anderson impurity model (AIM) in the DMFT self-consistency loop. Before explaining the DMFT algorithm in more detail, let us first present the AIM, see also, e.g., Ref. [17]

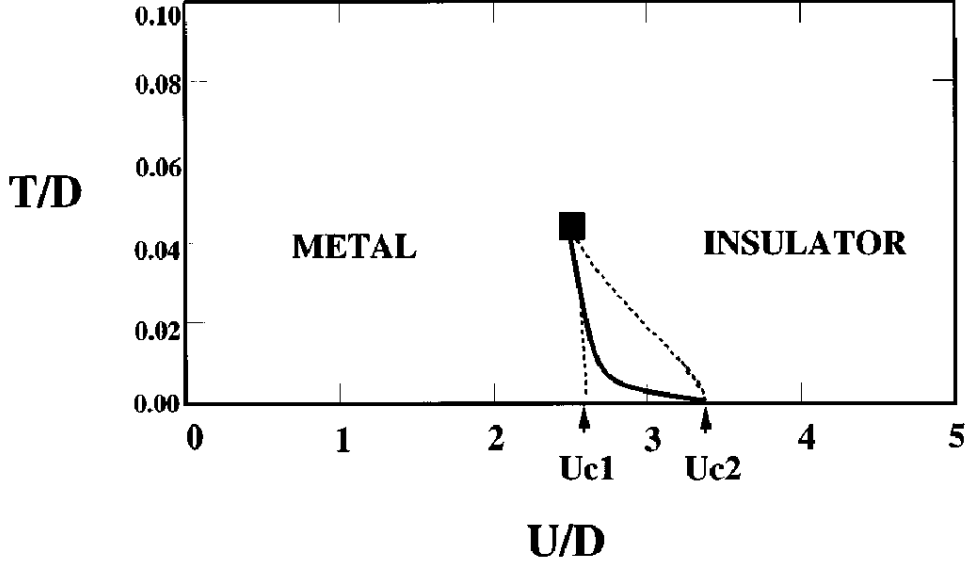


Figure 2.1: Generic phase diagram (as a function of temperature T and interaction U in units of half the bandwidth D) for the Mott-Hubbard metal-insulator transition for a half-filled, fully frustrated lattice. The transition is first order, the two phases are separated by a coexistence region between U_{c1} and U_{c2} (dashed lines) where hysteresis effects can occur. The actual first-order transition takes place at the solid line, which terminates in two second-order end points (the end-point at $T = 0$ is also second order). Picture taken from Ref. [10].

for more details. The AIM is represented by the Hamiltonian

$$\mathcal{H}_{\text{Anderson}} = \sum_{\sigma} \epsilon_{0\sigma} c_{0\sigma}^{\dagger} c_{0\sigma} + U n_{0\uparrow} n_{0\downarrow} + \sum_{\mathbf{k}, \sigma} V_{\mathbf{k}} \left(c_{\mathbf{k}, \sigma}^{\dagger} c_{0\sigma} + c_{0\sigma}^{\dagger} c_{\mathbf{k}\sigma} \right) + \sum_{\mathbf{k}, \sigma} \tilde{\epsilon}_{\mathbf{k}} c_{\mathbf{k}\sigma}^{\dagger} c_{\mathbf{k}\sigma}, \quad (2.8)$$

where in the first two terms describe the local level with energy $\epsilon_{0\sigma}$ and Coulomb interaction U . The third term describes the coupling of the impurity to a non-interacting band, which is given by the last term. The coupling of the impurity to the band can be described by the hybridization function $\Delta(\omega)$ [17], where

$$\Delta(\omega) = \sum_{\mathbf{k}, \sigma} \frac{|V_{\mathbf{k}}|^2}{\omega - \tilde{\epsilon}_{\mathbf{k}}}. \quad (2.9)$$

The local free ($U = 0$) Green's function $\mathcal{G}_0(\omega)$ can be written as

$$\mathcal{G}_0^{-1}(\omega) \equiv \omega + \mu - \Delta(\omega). \quad (2.10)$$

Thus the interacting Green's function G_{Anderson} takes the form

$$G_{\text{Anderson}} = \frac{1}{\omega + \mu - \Delta(\omega) - \Sigma(\omega)}, \quad (2.11)$$

where the local self-energy $\Sigma(\omega)$ has been introduced. The AIM can be solved numerically, see Section 2.4.

The self-consistency loop can be written as

$$\Sigma \xrightarrow{1.} G_{\text{lat}} \xrightarrow{2.} \mathcal{G}_0 \xrightarrow{3.} \Sigma, \quad (2.12)$$

which will now be explained in more detail. We start from the solution of the AIM, which is contained in the self-energy $\Sigma(\omega)$. Now the approximation of the DMFT enters by assuming that the lattice self-energy is local and thus \mathbf{k} -independent and can be set equal to the self-energy of the impurity, $\Sigma_{\text{lattice}}(\mathbf{k}, \omega) \approx \Sigma(\omega)$. Thus the on-site lattice Green's function is given by (first step of (2.12))

$$G_{\text{lat}}(\omega) \equiv G_{\text{lat}}(\mathbf{x} = 0, \omega) = \sum_{\mathbf{k}} e^{i\mathbf{x}\mathbf{k}} G_{\text{lat}}(\mathbf{k}, \omega) = \int d\epsilon \frac{\rho(\epsilon)}{\omega + \mu - \epsilon - \Sigma(\omega)}, \quad (2.13)$$

where $\rho(\epsilon) = \sum_{\mathbf{k}} \delta(\epsilon - \epsilon_{\mathbf{k}})$ is the density of states of the band. The self-consistency condition can be phrased as $G_{\text{lat}} = G_{\text{Anderson}}$, i.e. one demands the lattice and the impurity Green's functions to be equal, which defines the mapping of the lattice to the impurity model. The self-consistency equation can be written as

$$G_{\text{lat}}^{-1}(\omega) = \mathcal{G}_0^{-1}(\omega) - \Sigma(\omega). \quad (2.14)$$

The free Green's function of the impurity model $\mathcal{G}_0(\omega)$ encodes the information of the bath of the single site, constituted by all other lattice sites. It corresponds to the effective Weiss field in the Weiss mean-field theory for the Ising model. Instead of the static Weiss field, our effective field has the form of a function, hence the method was termed dynamical mean-field theory. The 'Weiss-function' $\mathcal{G}_0(\omega)$ will be referred to as 'bath function' in the following. By Eq. (2.14), the bath of the Anderson impurity model, defined by \mathcal{G}_0^{-1} , can be computed with G_{lat} and Σ (second step of (2.12)). In Section 2.4 two "impurity solvers" will be introduced, that can be fed with $\mathcal{G}_0^{-1}(\omega)$ and will finally calculate $\Sigma(\omega)$ (third step of (2.12)). Thus the loop is closed and can now be iterated until a self-consistent solution is reached.

Two approximations have been made. Firstly, the solution has been assumed to be homogeneous and translational invariant. In the next section we will show how the method can be generalized to deal with inhomogeneous systems and solutions. Secondly, the self-energy has been assumed to be local, $\Sigma(\omega, \mathbf{x}_i, \mathbf{x}_j) = \Sigma(\omega)\delta_{i,j}$. Metzner and Vollhardt [11] showed that this approximation becomes exact in the limit of infinite dimensions, $d \rightarrow \infty$. To ensure that kinetic and interaction energy in the Hubbard model stay of the same order of magnitude while taking the limit, one has to scale the hopping as $t \rightarrow \frac{t^*}{\sqrt{z}}$, where z is the connectivity of the lattice, which also goes to infinity as $d \rightarrow \infty$. In this limit it can be shown that all non-local contributions are suppressed by a factor $\frac{1}{\sqrt{d}}$. This result was obtained from a diagrammatic perturbation expansion of the self-energy in real space [11] and in momentum-space [13], see also [10].

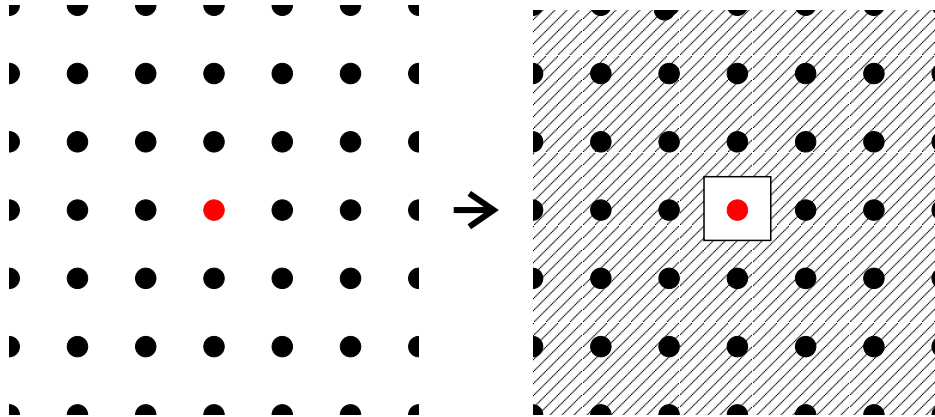


Figure 2.2: Dynamical-Mean-Field Theory: one site (red) of the interacting lattice is singled out. All other sites of the lattice are mapped to a bath coupled to the single site, thus the procedure maps the lattice model to an Anderson impurity model. In case of a homogeneous, translational invariant system the procedure is the same for every lattice site.

Another limitation of the method is the solution of the Anderson impurity model. Since no analytical solution exists, one has to retreat to numerical methods. Therefore DMFT can only be pursued numerically. Furthermore, all available impurity solvers are limited by their individual approximations, which affect the whole DMFT procedure, see section 2.4.

Regarding computational demands, DMFT can be done nowadays on a usual desktop PC (AMD Athlon, 3 GHz, 2 GByte RAM). The bottleneck concerning computational time and precision is step three of the self-consistency loop (2.12), which depends on the choice of the impurity solver. In the case of Numerical Renormalization Group (NRG), see section 2.4.2, which is one of the most accurate methods, the solution of the Anderson impurity model takes 1-2 minutes. In order to reach a self-consistent solution, the DMFT self-consistency loop has to be iterated around 100-1000 times, which results in a total computational time of several hours up to a day in the case of NRG. In contrast to NRG, which requires only very little memory, other impurity solvers like exact diagonalization require not only computational time but also much memory, i.e. one is either limited by computational time or memory. The other steps in (2.12) neither require a significant time nor memory.

2.2.2 Results

DMFT makes it possible to study the metal-insulator transition quantitatively. Results computed with the Numerical Renormalization Group (see Section 2.4.2) as impurity solver are shown in Fig. 2.3 and Fig. 2.4. As mentioned above, for small values of the interaction U we expect a Fermi liquid state with a quasi-particle resonance. The low-frequency

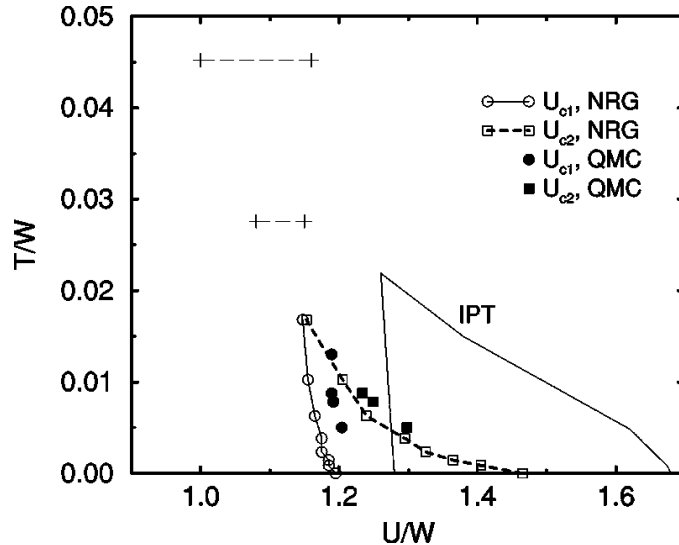


Figure 2.3: Phase diagram of the paramagnetic Mott metal-insulator transition. The temperature T and interaction U are given in units of the full bandwidth $W = 2D$. Regarding the critical interactions U_{c1} and U_{c2} , the agreement between the DMFT/NRG and DMFT/Quantum Monte Carlo results is rather good, while DMFT/IPT overestimates the U_{c1} and U_{c2} . Picture taken from [18].

behavior of the self-energy is then given by

$$\begin{aligned} \text{Re}\Sigma(\omega + i0) &= Un + \left(1 - \frac{1}{Z}\right)\omega + \mathcal{O}(\omega^3), \\ \text{Im}\Sigma(\omega + i0) &\propto -\omega^2 + \mathcal{O}(\omega^4), \end{aligned} \quad (2.15)$$

c.f. Fig. 2.3, where n is the filling and Z is the weight of the quasi-particle peak [10].

Note that at zero temperature $T = 0$, the height of the peak is pinned to the noninteracting value of the density of states,

$$A(\omega = 0) = \rho(\mu_0), \quad (2.16)$$

where μ_0 is the chemical potential at $U = 0$ which is determined by the filling. This was shown by Müller-Hartmann [12] by the following argument. In the limit of infinite dimensions, i.e. in the DMFT limit, the Luttinger theorem [12] takes the simple form

$$\mu = \mu_0 + \Sigma(\omega = 0). \quad (2.17)$$

Note that $\text{Im}\Sigma(\omega = 0) = 0$ at $T = 0$. If this result is plugged into Equation (2.13), $A(\omega) = (-1/\pi)\text{Im}G_{\text{lat}}(\omega + i\delta) = \text{Im} \int d\epsilon \rho(\epsilon)/(\omega + \mu - \epsilon - \Sigma(\omega))$, one obtains Equation (2.16). Thus, at $T = 0$, Z is proportional to the width of the peak.

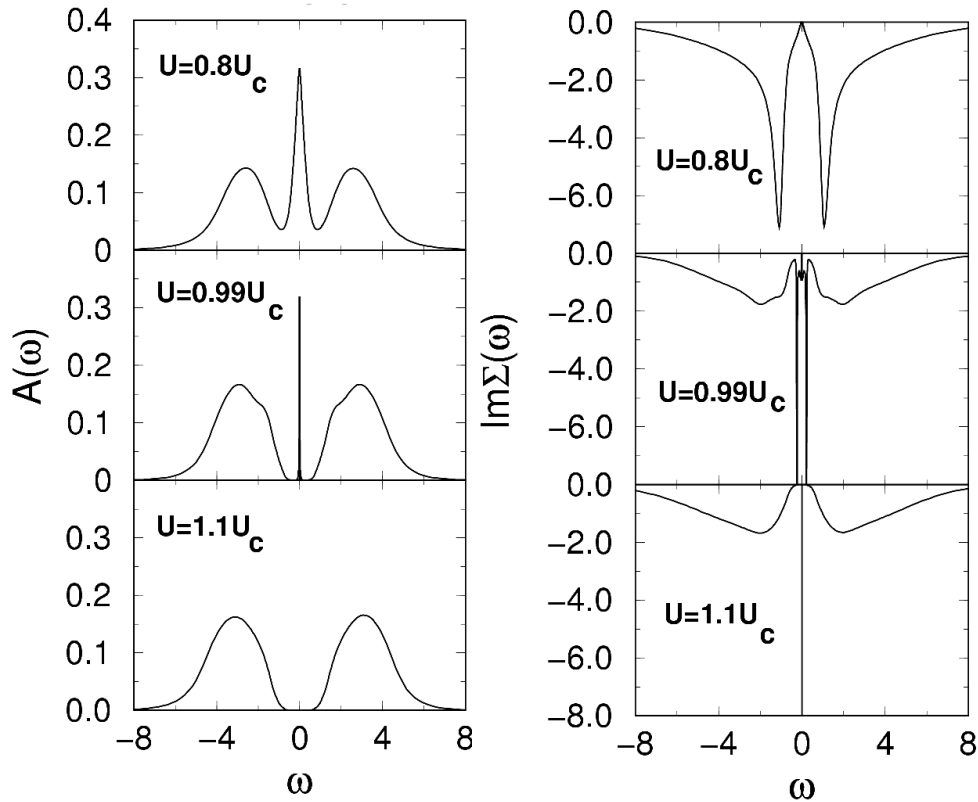


Figure 2.4: Metal-insulator transition at zero temperature calculated with DMFT and the Numerical Renormalization Group as impurity solver, see Section 2.4.2. In the left panel the spectral densities $A(\omega)$ for half filling and increasing values of the interaction U are shown. The top panel shows the metallic state with the quasi-particle peak at the Fermi-energy. Close to the transition (middle panel) the quasi-particle peak has almost vanished, whereas in the bottom panel the insulating state is reached. In the right panel the corresponding imaginary parts of the self-energies are depicted. Picture taken from [19].

By the mapping of the lattice onto the Anderson impurity model in the self-consistency loop, the energy scale ZD (where D is half the bandwidth) is translated into the Kondo temperature T_K of the defined impurity problem. If the temperature $T < T_K$, the Kondo resonance appears, which translates back into the quasi particle peak in the lattice model. Thus whether $T < T_K$ or not decides if the considered system is metallic or insulating, respectively. Through the self-consistency loop, the Kondo resonance enhances itself, since the quasi-particle peak also appears in the bath coupled to the impurity and T_K increases with the width of the quasi-particle peak in the bath. This fact is important to understand the hysteresis in the first order metal-insulator transition, see Fig. 2.1. If one starts in the metallic regime and increases U , Z and accordingly T_K decrease until a critical value U_{c2} is reached where $Z = 0$ and $T_K = 0$. However, if one starts in the insulating regime and

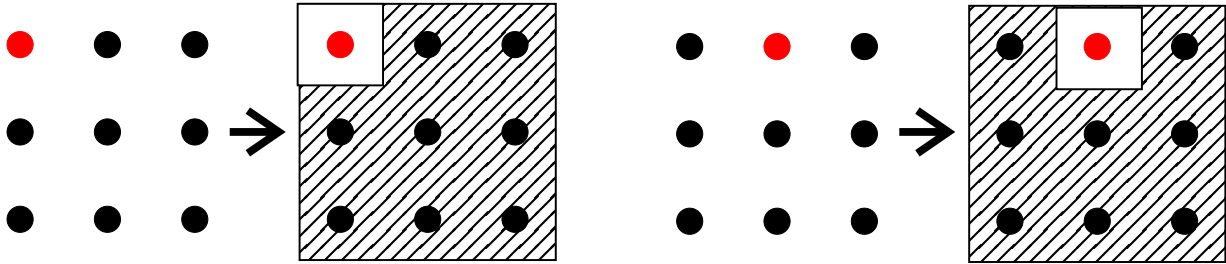


Figure 2.5: Inhomogeneous Dynamical-Mean-Field Theory: for an inhomogeneous system without translational invariance the mapping from the lattice to the impurity model is different for each site. However, one still can use symmetries of the inhomogeneous lattice. In this very simple example, the four sites at the corners and the four sites between the corner sites are equivalent. Thus there are only three different impurity models.

decreases U , no quasi-particle peak appears at U_{c2} since there is no sufficient density of states at the chemical potential. The state stays metallic until the lower critical value U_{c1} is reached. The real first order transition line lies in between, where the free energies of the metallic and insulating state are the same, $F_{\text{metallic}} = F_{\text{insulating}}$.

2.3 Dynamical Mean-Field Theory for inhomogeneous systems

If one considers an inhomogeneous Hubbard-like model (see Sections 3 or 5) or an inhomogeneous solution of the homogeneous Hubbard model (see Section 4), the DMFT procedure has to be generalized in a way suggested by Potthoff and Nolting [20]. Before presenting Potthoff's derivation of the mean-field equations [21], let us first explain the algorithm below. Furthermore, the approach was used by Okamoto and Millis [22]. The mapping procedure from the lattice to the impurity model becomes now different for each site, see Fig. 2.5. Thus, one generally obtains a different impurity model for each lattice site. Depending on the specific problem under consideration, the number of impurity problems can be significantly reduced by using symmetries of the lattice. In the toy example of the 9 lattice sites in Fig. 2.5, there are only three types of inequivalent lattice sites: the four sites at the corners, the four sites between the corner sites and the one in the middle. The self-consistency loop can now be written as

$$\{\Sigma_i\} \xrightarrow{1.} \hat{G}_{\text{lat}}(i, j) \xrightarrow{2.} \mathcal{G}_{0,i} \xrightarrow{3.} \{\Sigma_i\}. \quad (2.18)$$

Instead of only one self-energy we have now a set of self-energies $\{\Sigma_i\}$, one for each inequivalent site. Since translational invariance is broken, the Green's function of the lattice can not be diagonalized by Fourier transform. In the Wannier state basis $|i\rangle$, where i labels the site, the inverse of the free Green's function is given by $G_{0,\text{lat}}^{-1}(i, j, \omega) = \langle i | \omega + \mu - H_0 | j \rangle$. Here H_0 is the non-interacting part of the Hubbard model. This can be written in matrix

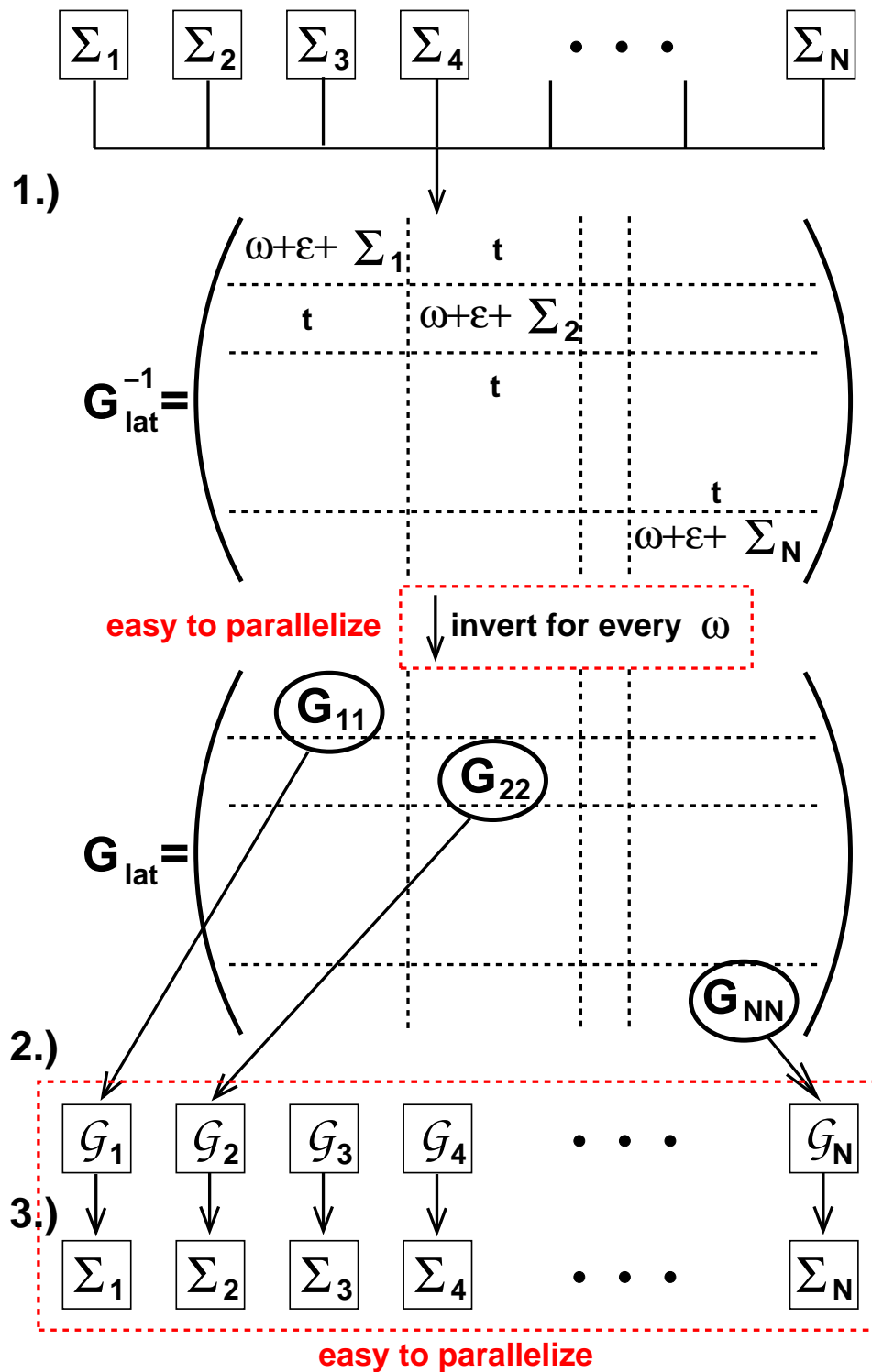


Figure 2.6: DMFT flow: the three steps of equation (2.18) are visualized. In a numerical realization of the DMFT self-consistency loop, the computations in the dashed boxes are the bottle-necks of the algorithm. Since they are independent of each other, they can be implemented very efficiently with almost no numerical overhead using parallel computing.

form

$$\hat{G}_{0,\text{lat}}^{-1}(\omega) = \begin{pmatrix} \omega + \mu & t & t & & & \\ t & \omega + \mu & t & & & \\ & t & \cdot & & & \\ t & & & \cdot & & \\ & & & & \cdot & t \\ & & & & t & \omega + \mu \end{pmatrix}, \quad (2.19)$$

where the rows and columns correspond to the lattice sites and neighboring sites are connected by the hopping amplitude t . In the interacting case a self-energy matrix $\hat{\Sigma}(i, j)$ has to be subtracted. Now again the approximation enters that the self-energy is local, $\hat{\Sigma}(i, j) \equiv \Sigma_i \delta_{i,j}$, i.e. off-diagonal terms of the self-energy are neglected. Thus the full Green's function can be written as the following matrix,

$$\hat{G}_{\text{lat}}^{-1}(\omega) = \begin{pmatrix} \omega + \mu - \Sigma_1(\omega) & t & t & & & \\ t & \omega + \mu - \Sigma_2(\omega) & t & & & \\ & t & \cdot & & & \\ t & & & \cdot & & \\ & & & & \cdot & t \\ & & & & t & \omega + \mu - \Sigma_N(\omega) \end{pmatrix}, \quad (2.20)$$

where N is the total number of sites. In this notation the self-energies of symmetry related sites are the same, i.e. the self-energy of the inequivalent site i might enter the matrix several times, according to the degeneracy of site i . However, using group symmetry the matrix can be reduced such that the self-energies $\{\Sigma_i\}$ of the inequivalent sites appear only once. This accomplishes the first step of the self-consistency loop (2.18) and presents the generalization of Eq. (2.13). The self-consistency condition (2.14) of the homogeneous case now takes the form $G_{\text{lat}}(i, i, \omega) = G_{\text{Anderson},i}$, i.e. the Green's function of the Anderson impurity model of the inequivalent site i is set equal to the diagonal term of the lattice Green's function at site i . With the help of the definitions (2.11) and (2.9) this can be written as

$$G_{\text{lat}}^{-1}(i, i, \omega) = \mathcal{G}_{0,i}^{-1}(\omega) - \Sigma_i(\omega), \quad (2.21)$$

which presents step two of (2.18). To close the self-consistency loop, we need to solve the Anderson impurity models defined by the bath functions $\mathcal{G}_{0,i}(\omega)$. This will give us a new set of self-energies $\{\Sigma_i\}$ (step three of (2.18)).

In contrast to the homogeneous case, the DMFT procedure for inhomogeneous systems described here is from a computational point of view very demanding, see Fig. 2.6, representing a visualization of the self-consistency loop (2.18). There are two bottlenecks. Firstly, the computational time needed to invert the lattice Green's function matrix Eq. (2.20), which needs to be done for each value of the discretized ω interval, grows as N^3 , where N is the dimension of the matrix. Depending on the problem under consideration specifying the form and the size of the matrix, the inversion needs several seconds. For a typical discretization of the ω interval with 1000-4000 values, a total time of order of hours is needed. Secondly, the number of Anderson models which needs to be solved is

now equal to the number of inequivalent sites, typically a number about 100. In the case of NRG as impurity solver, this amounts up to several hours. Altogether, one iteration of the self-consistency loop now takes typical between four and six hours. Thus a complete run now takes a time of order of weeks. However, looking at the flow diagram Fig. 2.6, one sees that both bottlenecks can easily be tackled by parallelizing the program. Since the amount of computational time spent in the bottlenecks almost sums up to the complete computational time, the parallelization overhead is very little and the total time can be divided by the numbers of nodes used on the parallel cluster.

A very nice derivation of the DMFT mean-field equations and an illuminative view on the DMFT in general can be found in Ref. [21] by Potthoff. He introduces a general Hamiltonian $\mathcal{H} = \mathcal{H}_0(\mathbf{t}) + \mathcal{H}_1(U)$ with the first part describing the hopping \mathbf{t} and the second part describing the interaction,

$$\mathcal{H} = \sum_{\alpha,\beta} t_{\alpha,\beta} c_{\alpha}^{\dagger} c_{\beta} + \frac{1}{2} \sum_{\alpha,\beta,\gamma,\delta} c_{\alpha}^{\dagger} c_{\beta}^{\dagger} c_{\gamma} c_{\delta} U_{\alpha,\beta,\gamma,\delta}, \quad (2.22)$$

where α, β, \dots are an orthonormal and complete set of one-particle basis states. The corresponding one-particle Green's function takes the matrix form $G_{\alpha\beta}(i\omega) = \langle\langle c_{\alpha}; c_{\beta}^{\dagger} \rangle\rangle$. It can be calculated from the self-energy $\Sigma_{\alpha,\beta}(i\omega)$ via the Dyson equation, which in matrix notation reads $\mathbf{G} = \mathbf{G}_0 + \mathbf{G}_0 \mathbf{\Sigma} \mathbf{G}$, where also the free Green's function $\mathbf{G}_0 = 1/(i\omega + \mu - \mathbf{t})$ has matrix form, due to the hopping matrix \mathbf{t} . Using the Legendre transform $F[\mathbf{\Sigma}] \equiv \phi[\mathbf{G}[\mathbf{\Sigma}]] - \text{Tr}(\mathbf{\Sigma} \mathbf{G}[\mathbf{\Sigma}])$ of the so-called Luttinger-Ward functional $\phi[\mathbf{G}]$, one can write the grand potential of the system as

$$\Omega_{\mathbf{t}}[\mathbf{\Sigma}] \equiv \text{Trln} \left(-(\mathbf{G}_0^{-1} - \mathbf{\Sigma})^{-1} \right) + F[\mathbf{\Sigma}]. \quad (2.23)$$

Here the subscript \mathbf{t} indicates that Ω explicitly depends on \mathbf{t} via the free Green's function \mathbf{G}_0 . One can show that the grand potential $\Omega_{\mathbf{t}}[\mathbf{\Sigma}]$ is stationary at the exact physical self-energy,

$$\frac{\partial \Omega_{\mathbf{t}}[\mathbf{\Sigma}]}{\partial \mathbf{\Sigma}} = 0 \Leftrightarrow \mathbf{G}[\mathbf{\Sigma}] = (\mathbf{G}_0^{-1} - \mathbf{\Sigma})^{-1}. \quad (2.24)$$

If one knew the grand potential explicitly, the self-energy could be determined by Eq. (2.24). However, in general the functional $F[\mathbf{\Sigma}]$ is not known explicitly. The idea is the following: one constraints the domain of $\Omega_{\mathbf{t}}[\mathbf{\Sigma}]$ to a subspace of self-energies for which one can find an explicit expression for $\Omega_{\mathbf{t}}[\mathbf{\Sigma}]$. On that subspace, $\Omega_{\mathbf{t}}[\mathbf{\Sigma}]$ is minimized to find the best approximation to the exact self-energy. One can derive an explicit form of $\Omega_{\mathbf{t}}[\mathbf{\Sigma}]$ on a constrained subspace in the following way. If one wishes to find an approximation of the self-energy for the Hamiltonian (2.22), one chooses a subspace $\Sigma(\mathbf{t}')$, where the $\Sigma(\mathbf{t}')$ parametrize the exact self-energies of a set of Hamiltonians of reference systems $\mathcal{H}' = \mathcal{H}_0(\mathbf{t}') + \mathcal{H}_1(U)$ with the same interaction but different hopping as in (2.22). The crucial observation is that $F[\mathbf{\Sigma}]$ does only depend on the interaction $\mathcal{H}_1(U)$ [21]. Thus the grand potential $\Omega_{\mathbf{t}'}[\mathbf{\Sigma}]$ of the reference system has the form

$$\Omega_{\mathbf{t}'}[\mathbf{\Sigma}] = \text{Trln} \left(-(\mathbf{G}'_0^{-1} - \mathbf{\Sigma})^{-1} \right) + F[\mathbf{\Sigma}], \quad (2.25)$$

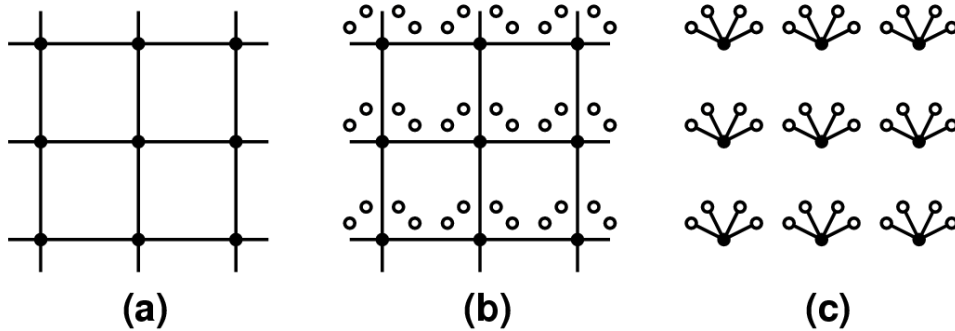


Figure 2.7: (a) Schematic representation of the Hubbard model. (b) By introducing n_s (here $n_s = 4$) decoupled sites per lattices site, on can ceate an equivalent model. (c) By changing the hopping but keeping the same interaction, a reference system can be set up. For $n_s \rightarrow \infty$, one obtains a model consisting out of decoupled Anderson impurity problems. Picture taken from [20]

with the same $F[\Sigma]$ as in (2.23). Thus $F[\Sigma]$ can be eliminated by taking the difference,

$$\Omega_t[\Sigma] = \Omega_{t'}[\Sigma] + \text{Trln} \left(-(\mathbf{G}_0^{-1} - \Sigma)^{-1} \right) - \text{Trln} \left(-(\mathbf{G}'_0^{-1} - \Sigma)^{-1} \right). \quad (2.26)$$

On the subspace of the $\Sigma(\mathbf{t}')$, which are the correct self-energies of the reference systems $\mathcal{H}' = \mathcal{H}_0(\mathbf{t}') + \mathcal{H}_1(U)$, $\Omega_{t'}[\Sigma]$ is the exact grand potential Ω' of the system. Furthermore $(\mathbf{G}'_0^{-1} - \Sigma)^{-1} = \mathbf{G}'$, the exact Green's function of the reference system,

$$\Omega_t[\Sigma(\mathbf{t}')] = \Omega' + \text{Trln} \left(-(\mathbf{G}_0^{-1} - \Sigma(\mathbf{t}'))^{-1} \right) - \text{Trln}(-\mathbf{G}'). \quad (2.27)$$

This is the main result. Note that $\Omega_t[\Sigma(\mathbf{t}')] only involves quantities from the reference system, apart from the free Green's function \mathbf{G}_0 . If the reference system is chosen such that quantities can be calculated easier than in the original system, one can find an approximation for $\Sigma(\mathbf{t})$ by determining the stationary point of $\Omega_t[\Sigma(\mathbf{t}')]$, $\partial\Omega_t[\Sigma(\mathbf{t}')]/\partial\mathbf{t}' = 0$, which gives$

$$T \sum_{\omega} \sum_{\alpha,\beta} \left(\frac{1}{\mathbf{G}_0^{-1} - \Sigma(\mathbf{t}')} - \mathbf{G}' \right)_{\alpha,\beta} \frac{\partial \Sigma_{\alpha,\beta}(\mathbf{t}')}{\partial \mathbf{t}'} = 0. \quad (2.28)$$

In our case the original system is the Hubbard model (2.6), depicted in Fig. 2.7 a. Introducing a number n_s of decoupled non-interaction sites per original lattice site creates an equivalent model (Fig. 2.7 b, where $n_s = 4$). By changing the hopping, a possible reference system can be obtained (Fig. 2.7 c). Note that for $n_s \rightarrow \infty$, the reference system consists out of decoupled Anderson impurity models. The self-energy is local, hence $\partial\Sigma_{ij}(\mathbf{t}')/\partial\mathbf{t}' \propto \delta_{ij}$. Thus (2.28) reduces to

$$\left(\frac{1}{\mathbf{G}_0^{-1}(i\omega) - \Sigma(i\omega)} \right)_{ii} = G'_{ii}(i\omega). \quad (2.29)$$

For a homogeneous system, the equation is independent of i and corresponds to the DMFT self-consistency equation (2.14). For an inhomogeneous system, (2.29) represents the set of self-consistency equations introduced in (2.21).

2.4 Impurity solvers

As explained above, to implement the DMFT self-consistency loop, one must solve the Anderson impurity model for arbitrary bands. No analytical solution exists, so to make further progress one has to deal with numerical methods with different approximations. Various choices exist, Quantum Monte Carlo (QMC), exact diagonalization (ED) and the Numerical Renormalization Group (NRG) are among the most important ones. QMC is a rather expensive method [10,23] and thus not well suited for our purposes, since we need to solve the Anderson impurity problems many times per iteration, see above. Furthermore, one cannot access the low temperature regime and one is limited by the ‘‘sign problem’’ if one desires to study magnetic solutions.

Using ED, one discretizes the bath which is then approximated by a set of sites with energies ϵ_j and couplings V_j . Arriving at step three of the self-consistency loop (2.14), the set $\{\epsilon_j, V_j\}$ is chosen such that a ‘distance function’ between the continuous bath function $\mathcal{G}_0(i\omega_n)$ and the discretized bath function $\mathcal{G}_0^{\text{discrete}}(i\omega_n) = i\omega_n + \mu - \sum_{j,\sigma} \frac{|V_j|^2}{i\omega_n - \epsilon_j}$ is minimized. The distance function is not unique and different popular choices exist, see Ref. [10,24]. The discretized Anderson model defined by the interacting impurity coupled to the set of sites is then solved exactly to determine the self-energy. ED works particularly well at zero temperatures, where one is able to use up to twelve ‘bath sites’. For finite temperatures, the method gets more expensive. We implemented a DMFT + ED version for inhomogeneous systems at finite temperatures using up to five ‘bath sites’. It turned out that this method had not the needed precision to obtain satisfactory results.

The NRG is one of the most accurate methods available and will be described in the second part of this section. In the ‘early days’ of DMFT the iterated perturbation theory method (IPT) turned out to be very useful. It is a rather simple method, based on second order perturbation theory in U in the Anderson model. It is numerically very inexpensive and also turned out to be useful for the DMFT for inhomogeneous systems implemented here. It will be described in the next section.

2.4.1 Iterated Perturbation Theory (IPT)

IPT at half-filling

Iterated perturbation theory bears on computing the self-energy of the Anderson model up to second order in U . The Hartree term of the self-energy is Un , where n is the average occupation of the impurity, $n = \langle n_\uparrow \rangle = \langle n_\downarrow \rangle$. As already mentioned, here we will stick to the paramagnetic solution $\langle n_\uparrow \rangle = \langle n_\downarrow \rangle$. Let us first consider the case of half-filling $n = 1/2$, the case of arbitrary filling will be treated below. The Fock term does not exist. Hence,

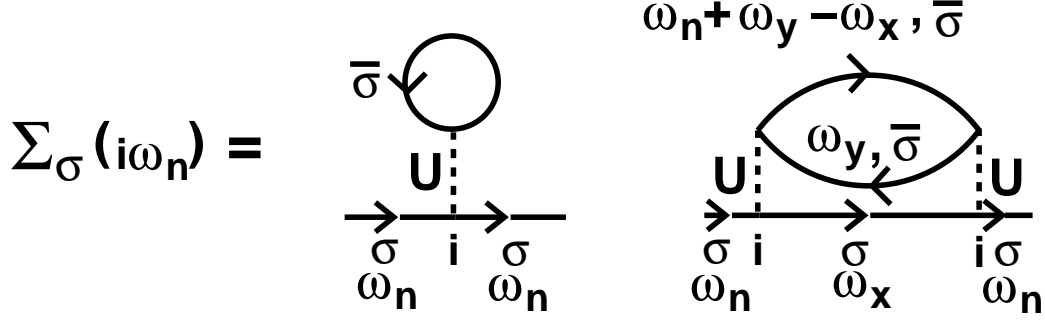


Figure 2.8: Contribution to the impurity self-energy in the iterated perturbation theory (IPT) approximation.

the only important contributions up to second order are the ones depicted in Fig. 2.8, and the self-energy takes the form

$$\Sigma(i\omega_n) = Un + U^2 \int_0^\beta d\tau e^{i\omega_n \tau} \mathcal{G}_0(\tau)^3 + \mathcal{O}(U^3), \quad (2.30)$$

which presents one of the simplest implementations of step three in the self-consistency loop (2.12). To be precise, \mathcal{G}_0 in the formula above does not exactly coincide with the definition (2.10), because the Hartree term of the self-energy is included in the calculation,

$$\mathcal{G}_0 \equiv \frac{1}{\omega + \mu - Un - \Delta(\omega)}. \quad (2.31)$$

Following Ref. [25], one can rewrite the self-energy in the following way. After Fourier transforming to Matsubara frequencies,

$$\Sigma(i\omega_n) = Un - U^2 T^2 \sum_{\Omega_1, \Omega_2} \mathcal{G}_0(i\Omega_1) \mathcal{G}_0(i\Omega_2) \mathcal{G}_0(i\Omega_1 + i\Omega_2 - i\omega_n),$$

and using a spectral representation of the bath function,

$$\mathcal{G}_0(z) = -\frac{1}{\pi} \int d\zeta \frac{\text{Im}\mathcal{G}_0(\zeta + i0)}{z - \zeta}, \quad (2.32)$$

one arrives at

$$\begin{aligned} \Sigma(i\omega_n) = & Un - \frac{U^2}{\pi^3} \int d\zeta_1 \text{Im}\mathcal{G}_0(\zeta_1 + i0) \int d\zeta_2 \text{Im}\mathcal{G}_0(\zeta_2 + i0) \int d\zeta_3 \text{Im}\mathcal{G}_0(\zeta_3 + i0) \\ & \frac{f(\zeta_1)f(\zeta_2)(1 - f(\zeta_3)) + (1 - f(\zeta_1))(1 - f(\zeta_2))f(\zeta_3)}{i\omega_n - \zeta_1 - \zeta_2 + \zeta_3}, \end{aligned} \quad (2.33)$$

where $f(\zeta)$ is the Fermi-function. Making use of

$$\frac{1}{z - \zeta_1 - \zeta_2 + \zeta_3} = -i \int_0^\infty d\lambda \exp[i\lambda(z - \zeta_1 - \zeta_2 + \zeta_3)] \quad (2.34)$$

the self-energy can be rewritten as

$$\Sigma(z) = \frac{U}{2} - iU^2 \int_0^\infty d\lambda e^{i\lambda z} (A^2(\lambda)B(\lambda) + B^2(\lambda)A(\lambda)). \quad (2.35)$$

Here an analytic continuation $i\omega_n \rightarrow z$ has been performed and

$$\begin{aligned} A(\lambda) &= -\frac{1}{\pi} \int d\zeta f(\zeta) \text{Im}\mathcal{G}_0(\zeta + i0) e^{-i\lambda\zeta}, \\ B(\lambda) &= -\frac{1}{\pi} \int d\zeta (1 - f(\zeta)) \text{Im}\mathcal{G}_0(\zeta + i0) e^{-i\lambda\zeta}. \end{aligned} \quad (2.36)$$

This formula for the self-energy can be used for $z \rightarrow \omega + i0$, such that the entire DMFT algorithm can be implemented on the real frequency axis $\omega + i\delta$. The advantage of calculating the self-energy via equation (2.35), instead of using equation (2.30), is the possibility of using the numerical very efficient Fast Fourier Transform algorithm for equations (2.35) and (2.36) which scales like $N \log N$, where N is the number of points on the frequency axis. In contrast, the direct evaluation of equation (2.30) in frequency space gives a threefold integral which scales like N^3 .

For the half-filled particle-hole symmetric case, DMFT+IPT turned out to be a very successful method, describing the metal-insulator transition qualitatively correctly, see Fig. 2.9, while being numerically inexpensive. Early works on the half-filled Anderson model at weak couplings showed that second order perturbation theory in U is a very good approximation up to values $U/\Delta(0) \sim 6$, [26–29]. Not only the physics of the Kondo resonance but also incoherent features of the upper and lower Hubbard band are captured by this approach. An important point to mention is that at half-filling, IPT exactly reproduces the atomic limit $U \rightarrow \infty$. In this limit, the lattice Green's functions can be written as (keeping in mind that the Hartree shift $-U/2$ is included in \mathcal{G}_0)

$$\begin{aligned} G_{\text{lat}}(i, i, i\omega_n) &= \sum_{\sigma} \left\langle i, \sigma \left| \frac{1}{i\omega_n - \mathcal{H}} \right| i, \sigma \right\rangle \\ &= \frac{1/2}{\mathcal{G}_0^{-1}(i\omega_n) - U/2} + \frac{1/2}{\mathcal{G}_0^{-1}(i\omega_n) + U/2} \\ &= \frac{1}{\mathcal{G}_0^{-1}(i\omega_n) - (U/2)^2 \mathcal{G}_0(i\omega_n)}, \end{aligned} \quad (2.37)$$

i.e. $\Sigma(i\omega_n) = (U/2)^2 \mathcal{G}_0(i\omega_n)$, which is just the Fourier transform of Equation (2.30), as shown in Ref. [30]. Thus the IPT provides an interpolation scheme between the exactly captured limits $U/D \rightarrow 0$ and $U/D \rightarrow \infty$. It is also worth mentioning that the self-energy (2.30) is always analytic in U , irrespective of the form of the bath \mathcal{G}_0 . The non-analyticities of the transition, see Fig. 2.9, are brought in by the DMFT self-consistency relation.

IPT away from half-filling

Away from half filling, the strong coupling limit $U/D \rightarrow \infty$ is not reproduced correctly by the self-energy (2.30) any more and the method has to be generalized. The first proposal

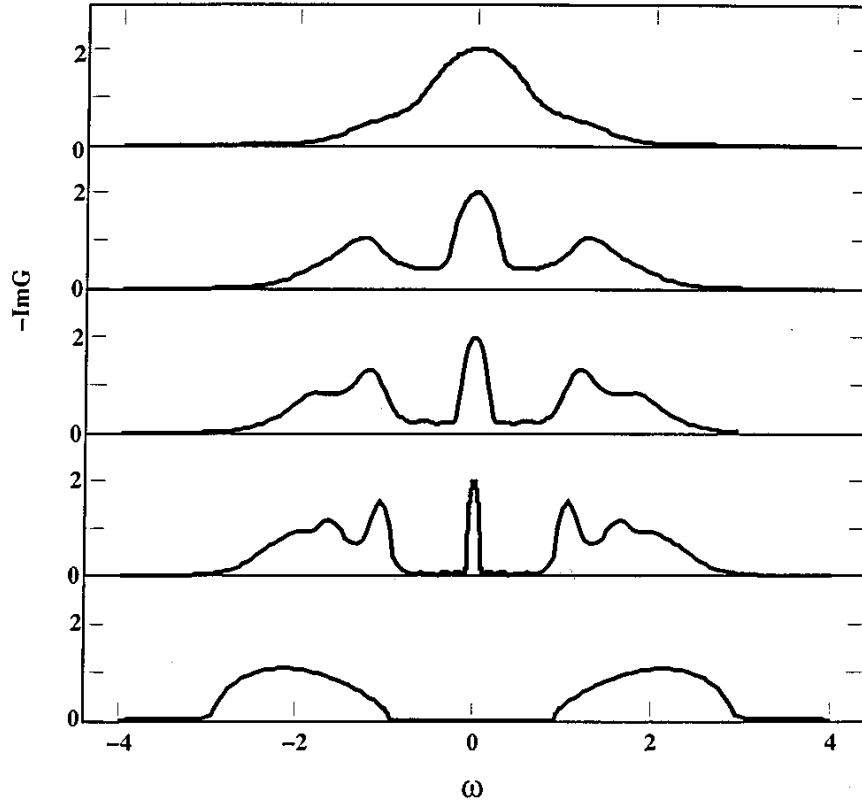


Figure 2.9: Mott Metal-insulator transition computed with DMFT+IPT: spectral density $A(\omega)$ at temperature $T = 0$ for several values of $U/D = 1.0, 2.0, 2.5$ and 3.0 (top to bottom). One clearly sees the transition from metal to insulator in the last panel. Picture taken from [10]

was made by Kotliar et al. [31, 32]. They made the following ansatz for the self-energy:

$$\Sigma(\omega) = Un + \frac{A\Sigma^{(2)}(\omega)}{1 - B\Sigma^{(2)}(\omega)}. \quad (2.38)$$

Here $\Sigma^{(2)}(\omega)$ is the second order contribution of Eq. (2.30), where, however, a new chemical potential $\tilde{\mu}$ is introduced in the bath function, c.f. Eq. (2.10),

$$\mathcal{G}_0^{-1}(\omega) \equiv \omega + \tilde{\mu} - Un - \Delta(\omega). \quad (2.39)$$

Again the Hartree shift is included in the definition of the bath function, c.f. Eq. (2.31). The three new free parameters $A, B, \tilde{\mu}$ are fixed in the following way. The moments $M^{(m)}$ of the spectral density of the on-site lattice Green's function, $A(\omega) = -\frac{1}{\pi}\text{Im}G_{\text{lat}}(\omega)$, are defined by

$$M^{(m)} = \int_{-\infty}^{\infty} d\omega \omega^m A(\omega). \quad (2.40)$$

They can be calculated along the lines of Ref. [33]. These moments appear in the large-frequency expansion of the lattice Green's function,

$$G_{\text{lat}}(\omega) = \int_{-\infty}^{\infty} \frac{A(\epsilon)}{\omega - \epsilon} d\epsilon \stackrel{\omega \gg 1}{\approx} \sum_{m=0}^{\infty} \frac{1}{\omega^{m+1}} M^{(m)}. \quad (2.41)$$

If one also expands the self-energy $\Sigma(\omega)$ in $1/\omega$,

$$\Sigma(\omega) = \sum_{m=0}^{\infty} \frac{1}{\omega^m} C^{(m)}, \quad (2.42)$$

one can plug in the expansions in the self-consistency condition

$$G_{\text{lat}}(\omega) \stackrel{!}{=} G_{\text{Anderson}} = \frac{1}{\omega + \mu - \Delta(\omega) - \Sigma(\omega)} \quad (2.43)$$

to obtain the moments of the self-energy $C^{(m)}$ from the moments of the lattice Green's function $M^{(m)}$, where one can use Equations (2.14) and (2.10), $\Delta(\omega) = \omega + \mu - \Sigma(\omega) - G_{\text{lat}}(\omega)$, to also expand $\Delta(\omega)$ in terms of $M^{(m)}$ and $C^{(m)}$. One arrives at

$$\Sigma(\omega) = Un + U^2 n(1-n) \frac{1}{\omega} + \mathcal{O}\left(\frac{1}{\omega^2}\right). \quad (2.44)$$

This should be compared with the high frequency expansion of $\Sigma^{(2)}(\omega)$, c.f. Equation (2.33),

$$\Sigma^{(2)}(\omega) = U^2 n_0(1-n_0) \frac{1}{\omega} + \mathcal{O}\left(\frac{1}{\omega^2}\right), \quad (2.45)$$

where $n_0 = -\frac{1}{\pi} \int d\omega \text{Im} \mathcal{G}_0(\omega + i0)$. Thus we conclude

$$A = \frac{n(1-n)}{n_0(1-n_0)} \quad (2.46)$$

to guarantee that $\Sigma(\omega)$ is correct to first order and G_{lat} is correct up to second order in $1/\omega$. Using higher order correlation functions, Potthoff et al. found an ansatz for the self-energy which is accurate up to second order in $1/\omega$ [34]. The parameter B is chosen such that the atomic limit $V_k \rightarrow 0$ is reproduced correctly. In the atomic limit, we have

$$G_{\text{lat}} = \frac{n}{\omega + i0 + \mu - U} + \frac{1-n}{\omega + i0 + \mu}, \quad (2.47)$$

c.f. Eq. (2.37), which can be written as $G_{\text{lat}} = 1/(\omega + i0 + \mu - \Sigma_{\text{atomic}})$ with

$$\Sigma_{\text{atomic}} = Un + \frac{U^2 n(1-n)}{\omega + i0 + \mu - (1-n)U}. \quad (2.48)$$

This result has to be compared with the atomic limit of our ansatz (2.38), where we first note that the atomic limit of the second order contribution is

$$\Sigma^{(2)}(\omega) \xrightarrow{\Delta(\omega) \rightarrow 0} \frac{U^2 n_0 (1 - n_0)}{\omega + i0 + \tilde{\mu} - Un}, \quad (2.49)$$

c.f. Eq. (2.33). Thus, we fix B as

$$B = \frac{(1 - 2n)U - \mu + \tilde{\mu}}{n_0(1 - n_0)U^2}. \quad (2.50)$$

Note, that for this choice of A and B the ansatz of the self-energy (2.38) reduces to the original self-energy (2.30) at half filling. What is left to fix, is $\tilde{\mu}$. Potthoff et al. pointed out three possibilities [34]. The most natural choice would be

$$\tilde{\mu} = \mu. \quad (2.51)$$

However, comparison with exact diagonalization results revealed significant differences between the two methods [34], so this choice is not recommendable. Alternatively, Martin-Rodero et al. [35] proposed to fix $\tilde{\mu}$ by imposing

$$n = n_0. \quad (2.52)$$

A third option by Kotliar et al. [31] uses the Luttinger theorem [36] to fix $\tilde{\mu}$. As mentioned earlier, c.f. Eq. (2.17), Müller-Hartmann pointed out [12] that in the case of the Hubbard model in infinite dimensions, the Luttinger theorem takes the simple form

$$\mu = \mu_0 + \Sigma(\omega = 0). \quad (2.53)$$

Since zero temperature is a premise of the Luttinger theorem, here $\Sigma(\omega = 0)$ is real. Both options $n = n_0$ and $\mu = \mu_0 + \Sigma(\omega = 0)$ are in agreement with exact diagonalization results to an acceptable extent [34]. However, since the choice $\mu = \mu_0 + \Sigma(\omega = 0)$ is restricted to zero temperature, the alternative $n = n_0$ is used in this thesis. Admittedly, this way to fix $\tilde{\mu}$ has the undesirable effect that an unphysical drop of the spectral density is observed at the Fermi edge, but only in the case of very strong interactions [34]. Note that all three methods are correct in the weak coupling limit $U \rightarrow 0$.

To conclude, the ansatz for the self-energy (2.38) with the appropriate choice of the constants A and B is correct in the high frequency limit, in the atomic limit and in the weak coupling limit. Despite using $n = n_0$, the method does not violate the Luttinger theorem by more than a few percent [34], which can be seen as the zero-frequency limit. Between these limits, the ansatz (2.38) is assumed to yield a reasonable interpolation scheme.

For the choice $n = n_0$, a comment on the numerical implementation is appropriate. Arriving at step two of the self-consistency loop (2.12), see also Fig. 2.6 for the inhomogeneous case, one computes \mathcal{G}_0 via

$$\mathcal{G}_0(\omega) = \frac{1}{G_{\text{lat}}^{-1}(\omega) + \Sigma(\omega) + \tilde{\mu} - \mu}. \quad (2.54)$$

In order to have a stable convergence of the algorithm, it is important to repeat this step while adjusting $\tilde{\mu}$ until $n = n_0$ is fulfilled to a high numerical accuracy.

2.4.2 Numerical Renormalization Group

The Numerical Renormalization Group (NRG) is another method to tackle the Anderson impurity model. Here, we will only sketch the general procedure, details can be found in the references given below. One of the main obstacles encountered while solving the Anderson model is that all energy scales contribute to the solution. Overcoming this problem is the key to making further progress. The Anderson model is the microscopic model underlying the Kondo model put forward by Kondo in 1964 [37]. The Kondo model can be obtained from the Anderson model by a Schrieffer-Wolff transformation [38] in the limit of unit charge on the impurity and freezing charge fluctuations, see Ref. [17] for details. A first hint that all energy scales are important first showed up in Kondo's perturbation theory for the Kondo model. Second order perturbation theory diverges in the limit of infinite bandwidth $D \rightarrow \infty$, a first sign that high energy states are important, see Ref. [17]. Since the interacting impurity is coupled to a bath with arbitrarily small excitations energies, perturbation calculations are not only plagued by ultraviolet but also infrared divergencies. Thus one has to look for non-perturbational approaches. A first step in the solution was made by Anderson in 1970 [39] with his 'Poor Man's Scaling'. There he integrated out high energy degrees of freedom in a simple second order perturbation renormalization group procedure, showing that for temperatures T below the Kondo temperature T_K a 'strong coupling limit' exists. In this limit, the impurity is strongly coupled to the conduction band electrons. This limit could not be further investigated by his perturbational method. In 1975 Wilson invented the NRG [40] which finally allowed to study the strong coupling limit. As the name implies, the NRG can only be performed numerically. However, it is able to give a full solution of the problem. In the original paper [40], the NRG was designed to compute thermodynamical properties for the Kondo model. It was soon extended to treat the Anderson model [41, 42] and also to compute dynamical quantities first at zero temperature $T = 0$, [43–45], then at $T > 0$ [46]. See Ref. [17] and Ref. [47] for details and further references.

Since one needs to take all energy scales into account, Wilson proposed a division of the conduction band with half bandwidth D into logarithmic intervals, see (a) of Fig. 2.10. One chooses a constant $\Lambda > 1$ to obtain the intervals $[-\Lambda^0 D, -\Lambda^{-1} D, -\Lambda^{-2} D, \dots, -\Lambda^{-n} D]$ for negative energies and $[\Lambda^{-n} D, \dots, \Lambda^{-2} D, \Lambda^{-1} D, \Lambda^0 D]$ for positive energies, where $n \rightarrow \infty$. In a next step, the states are discretized, see (b) in Fig. 2.10. In each interval, one makes a Fourier transform to the basis

$$\psi_{np}^{\pm}(\omega) = \begin{cases} \frac{1}{\sqrt{d_n}} e^{\pm i \frac{2\pi p}{d_n} \omega} & \text{for } \Lambda^{-(n+1)} < \pm\omega < \Lambda^{-n} \\ 0 & \text{outside this interval} \end{cases}, \quad (2.55)$$

where d_n is the length of the n th interval, $d_n = \Lambda^{-n}(1 - \Lambda^{-1})$ and $p \in \mathcal{N}$. One now keeps only the $p = 0$ states. For a flat band this is a good approximation for two reasons. Firstly, the $p \neq 0$ states do not couple to the impurity; they are only coupled indirectly since they are coupled to the $p = 0$ states. Secondly, the coupling between the $p = 0$ and $p \neq 0$ states has a prefactor $(1 - \Lambda)$, thus the coupling goes to zero as $\Lambda \rightarrow 1$. For an arbitrary band as used in DMFT calculations, the situation becomes more involved. However, the

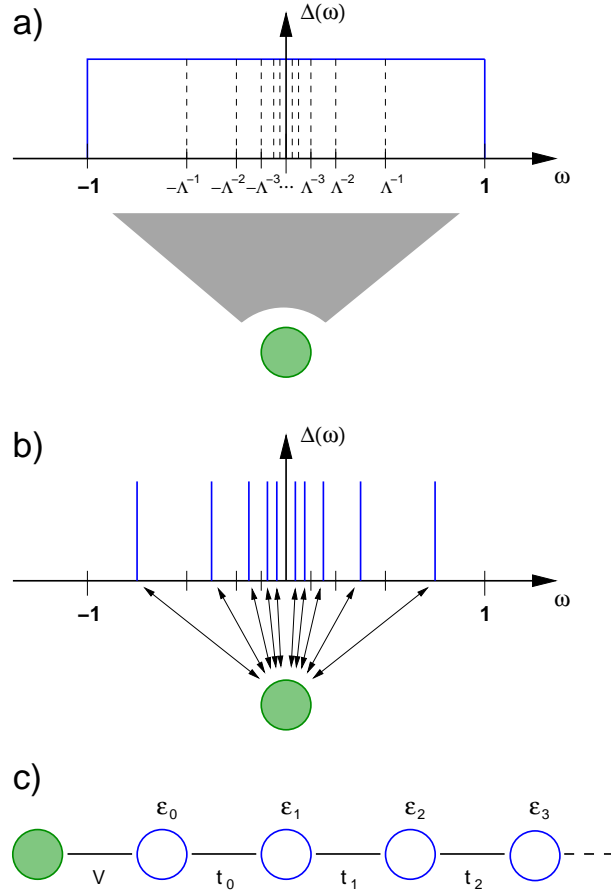


Figure 2.10: Mapping of the conduction band to a semi-infinite chain in the Numerical Renormalization Group (NRG) method; a) division of the conduction band into logarithmic intervals; b) discretization of the conduction band states; c) mapping to the semi-infinite chain. Picture taken from [47].

approximation made is still exact for $\Lambda \rightarrow 1$ [47]. After this 'logarithmic discretization', the $p = 0$ states are mapped to a semi-infinite chain, where the impurity is the first site, see part (c) of Fig. 2.10. The Hamiltonian describing the chain up to site N ,

$$\begin{aligned} \mathcal{H}_N = & \Lambda^{(N-1)/2} \left[\mathcal{H}_{\text{imp}} + \sqrt{\frac{\xi_0}{\pi}} \sum_{\sigma} \left(f_{\sigma}^{\dagger} c_{0\sigma} + c_{0\sigma}^{\dagger} f_{\sigma} \right) \right. \\ & \left. + \sum_{\sigma, n=0}^N \epsilon_n c_{n\sigma}^{\dagger} c_{n\sigma} + \sum_{\sigma, n=0}^{N-1} t_n \left(c_{n\sigma}^{\dagger} c_{n+1\sigma} + c_{n+1\sigma}^{\dagger} c_{n\sigma} \right) \right], \end{aligned} \quad (2.56)$$

approaches the Anderson Hamiltonian (2.8) in the limit $N \rightarrow \infty$,

$$\mathcal{H}_{\text{Anderson}} = \lim_{N \rightarrow \infty} \Lambda^{-(N-1)/2} \mathcal{H}_N. \quad (2.57)$$

Here \mathcal{H}_{imp} is the Hamiltonian of the impurity,

$$\mathcal{H}_{\text{imp}} = \sum_{\sigma} \epsilon_f f_{\sigma}^{\dagger} f_{\sigma} + U f_{\uparrow}^{\dagger} f_{\uparrow} f_{\downarrow}^{\dagger} f_{\downarrow}, \quad (2.58)$$

where $f_{\sigma}^{\dagger}(f_{\sigma})$ creates (destroys) an electron with spin σ on the impurity and U is the Coulomb repulsion between electrons on the impurity, as above. Furthermore $c_{n\sigma}^{\dagger}(c_{n\sigma})$ creates (destroys) an electron at site n with spin σ on the semi-infinite chain, ϵ_n is the energy of site n , $\sqrt{\xi_0/\pi}$ and t_n are the couplings between the impurity and the first site and between site n and $n+1$ respectively. For the relation of the operators $c_{n\sigma}^{\dagger}$ with the operators defined in (2.55) and the definition of ϵ_n and ξ_0 see Ref. [47]. For a flat band, the t_n are given by

$$t_n = \frac{(1 + \Lambda^{-1})(1 - \Lambda^{-n-1})}{2\sqrt{1 - \Lambda^{-2n-1}}\sqrt{1 - \Lambda^{-2n-3}}} \xrightarrow{n \rightarrow \infty} \frac{1}{2}(1 + \Lambda^{-1})\Lambda^{-n/2}. \quad (2.59)$$

Here the most important fact to notice about the semi-infinite chain is the exponential decrease of the coupling between the sites. A posteriori, this is one justification of the logarithmic discretization, because the division in ever smaller intervals for smaller energies is the reason for the exponential decay. The decay is important for the following reason. Two successive Hamiltonians are related by

$$\begin{aligned} \mathcal{H}_{N+1} &= \sqrt{\Lambda}\mathcal{H}_N + \Lambda^{N/2} \sum_{\sigma} \epsilon_{N+1} c_{N+1\sigma}^{\dagger} c_{N+1\sigma} \\ &\quad + \Lambda^{N/2} \sum_{\sigma} t_N \left(c_{N\sigma}^{\dagger} c_{N+1\sigma} + c_{N+1\sigma}^{\dagger} c_{N\sigma} \right). \end{aligned} \quad (2.60)$$

This relation can be understood as a renormalization group transformation R ,

$$\mathcal{H}_{N+1} = R(\mathcal{H}_N), \quad (2.61)$$

lying at the heart of the procedure. In contrast to a standard RG procedure, here the Hamiltonians before and after the RG transformation do *not* have the same form. Instead of renormalizing the coupling constants of the Hamiltonian, here directly the flow of the eigenenergies $E_N(r)$ is observed, with

$$\mathcal{H}_N |r\rangle_N = E_N(r) |r\rangle_N, \quad r = 1, \dots, N_{\mathcal{H}_N}, \quad (2.62)$$

where $|r\rangle_N$ are the eigenstates and $N_{\mathcal{H}_N}$ is the dimension of \mathcal{H}_N . Postponing the issue that the $N_{\mathcal{H}_N}$ is increased by a factor of four at each step, it is important to notice that the eigenenergies of the lowest lying eigenstates can flow to a fix point due to the exponential decreasing coupling constants t_N along the chain, since the factor $t_N \propto \Lambda^{-N/2}$ for large N cancels the factor $\Lambda^{N/2}$ in front of the last term in (2.60), guaranteeing that the lowest excited states always have energies of the order one. The procedure finally works as depicted in Fig. 2.11. After the eigenenergies $E_N(r)$ of \mathcal{H}_N are computed by numerical

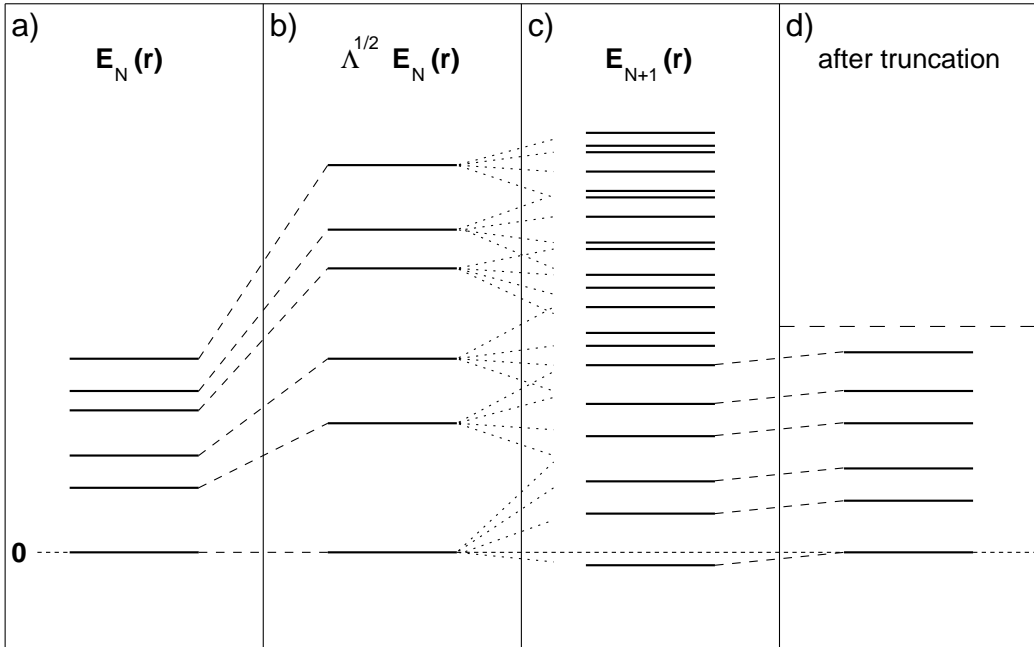


Figure 2.11: (a): Many-particle spectrum $E_N(r)$ of the Hamiltonian \mathcal{H}_N with the ground-state energy set to zero. (b): The relation between successive Hamiltonians, Eq. (recursionrelation), includes a scaling factor $\sqrt{\Lambda}$. (c) Many-particle spectrum $E_{N+1}(r)$ of \mathcal{H}_{N+1} . (d) The same spectrum after the truncation where only the N_s lowest-lying states are retained. The ground-state energy has again been set to zero. Picture taken from [47]

exact diagonalization (Fig. 2.11 a), the first term of the next Hamiltonian $\mathcal{H}_{N+\infty}$ in (2.60) is simply given by $\Lambda^{1/2}\mathcal{H}_N$ (Fig. 2.11 b). Now the next site is added to the chain, increasing the dimension $N_{\mathcal{H}_N}$ of the Hilbert space by four. Diagonalizing the Hamiltonian gives the eigenenergies $E_{N+1}(r)$. As just mentioned, the energy splittings are comparable to the splittings of $E_N(r)$ (Fig. 2.11 c). Since the procedure can only be performed numerically, the size of the Hamiltonian would exceed the available memory after only a few steps. Therefore the Hilbert space has to be truncated (Fig. 2.11 d) and only the N_s lowest-lying states are kept. Here the question arises how the neglect of the high-energy states effects the low energy sector. One can argue that by adding a new site to the chain one introduces a perturbation with relative strength $\Lambda^{-1/2} < 1$. Thus the truncation procedure becomes less exact for $\Lambda \rightarrow 1$. Accepting increasing numerical effort, this can be counterbalanced by increasing the number of kept states N_s . Thus, for fixed N_s , Λ must not be too small

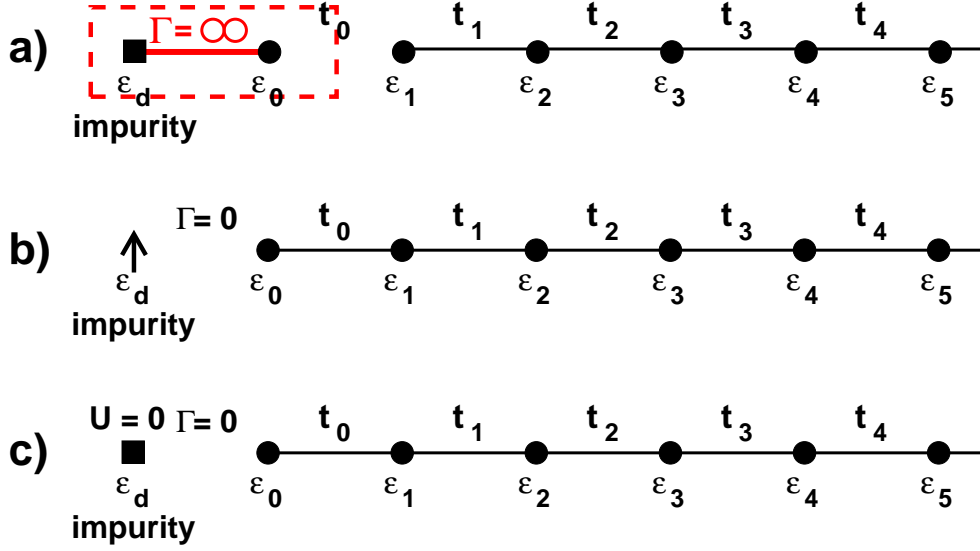


Figure 2.12: (a): Strong-coupling limit, where the effective hybridization Γ between the impurity and the first site is so strong that they are decoupled from the chain. The impurity and the first site build a singlet, the Kondo singlet, where the spin of the impurity is screened by the conduction electrons. (b): Local-moment limit, where the impurity is decoupled from the chain and is occupied by one electron due to the interaction U . Thus the degrees of freedom of the impurity are represented by a spin. (c): Free-orbital limit, where the impurity is decoupled and non-interacting. It thus has the four degrees of freedom of a free orbital.

on the one hand, on the other hand, if Λ is too large, the logarithmic grid becomes too crude and the approximation of neglecting the $p \neq 0$ states in (2.55) becomes worse.

The iteration of the algorithm is stopped when a fixed point is reached, i.e. when two successive Hamiltonians have the same eigenspectrum (actually, only \mathcal{H}_{N+2} and \mathcal{H}_N can have the same spectrum due to even-odd oscillations, see [47]). The three possible fixed points for the Anderson impurity model are depicted in Fig. 2.12. In these limits, the impurity is always decoupled from the rest of the chain (in the strong-coupling limit, the impurity and the first site are decoupled). Since the semi-infinite chain itself contains no interactions, it can easily be solved. The resulting eigenenergies can then be compared with the ones obtained in the NRG run.

In the NRG algorithm the thermal expectation values of operators can be calculated at each step. Since information about large frequency gets lost at large N due to the truncation of the Hilbert space of \mathcal{H}_N , the information from each step N , also called "shell" in the NRG community, has to be collected and put together at the end of the NRG run when a fixed point is reached, see Ref. [47] for details. The most important object to mention here is the Green's function of the Anderson impurity,

$$G_{\text{Anderson}}(t-t') \equiv -i\Theta(t-t')\langle [f_{\sigma}(t), f_{\sigma}^{\dagger}(t')]_{+} \rangle. \quad (2.63)$$

Its imaginary part, which is proportional to the spectral function, can be calculated with the help of the Lehmann representation using the computed matrix elements,

$$\begin{aligned} A_\sigma(\omega, T) &= -\frac{1}{\pi} \text{Im} G_{\text{Anderson}} \\ &= \frac{1}{Z(T)} \sum_{n,m} |\langle m | f_\sigma | n \rangle|^2 (e^{-E_n/T} + e^{-E_m/T}) \delta(\omega - (E_m - E_n)), \end{aligned} \quad (2.64)$$

where $|n\rangle$ are the eigenstates with eigenenergy E_n and Z is the partition function. However, due to the truncation, information about high energy states is lost during the algorithm. Hence, to determine the spectral function at $\sim \omega$, one either chooses to calculate matrix elements $\langle m | f_\sigma | n \rangle$ for $E_m - E_n \sim \omega$ at a stage where the information about the high energy state is still available but the lower lying state is not completely resolved yet or one chooses the following procedure by Hofstetter [48]. One runs through the iterative diagonalization twice. In the first step, one sets up the density matrix

$$\hat{\rho} = \sum_m e^{-E_m/T} |m\rangle \langle m|. \quad (2.65)$$

In the second step, one calculates at each length N of the semi-infinite chain the Green's function using

$$G_{\text{Anderson}}(t - t') = i\Theta(t) \text{Tr} \left(\hat{\rho}_{\text{red}} [f_\sigma(t), f_\sigma^\dagger(t')]_+ \right), \quad (2.66)$$

where the reduced density matrix $\hat{\rho}_{\text{red}}$ is obtained from the density matrix by tracing out the low energy degrees of freedom of shells greater than N .

To obtain the self-energy of the Anderson impurity model, our main object of interest within the DMFT, one can now in principle subtract the inverse of the non-interacting Green's function from the Green's function. However, numerical implementations of differences are always a source of error, so for the results produced in this thesis we follow the proposal of Bulla et al. to calculate the self-energy from the division of two correlation functions [49],

$$\Sigma(\omega) = U \frac{F(\omega)}{G_{\text{Anderson}}(\omega)}. \quad (2.67)$$

Here $G_{\text{Anderson}}(\omega)$ is the Green's function of the Anderson model, cf. Eq. (2.63), and $F(\omega)$ is a correlation function defined by

$$F(t - t') \equiv -i\Theta(t - t') \left\langle \left[f_\sigma(t) f_{\bar{\sigma}}^\dagger(t) f_{\bar{\sigma}}(t), f_\sigma^\dagger(t') \right]_+ \right\rangle. \quad (2.68)$$

Chapter 3

Heterostructures

In the last years, an enormous interest has arisen in heterostructures fabricated out of strongly correlated materials. Driven by the prospect of new effects and devices based on correlated electron compounds, a wide range of different systems has been studied theoretically and experimentally. One possible setup which has been largely investigated is the junction between two different insulators. Both Lee and McDonald [50] and Kancharla and Dagotto [51] showed that the region close to the junction between two different Mott insulators can exhibit metallic behavior. A similar behavior for the junction between a Mott and a band insulator was predicted by Okamoto and Millis [22, 52, 53]. They also demonstrated that there is a competition between the ferromagnetic metallic phase at the junction and the insulating anti-ferromagnetic phase in the bulk. Ohtomo et al. observed metallic behavior for a system made out of alternating atomic layers of $SrTi^{4+}O_3$, a band insulator, and $LaTi^{3+}O_3$, a Mott insulator. By increasing the thickness of the band- and Mott-insulating slices to five atomic layers, they recovered the bulk insulating behavior [54]. Also heterostructures made of metal and insulator have been investigated. Freericks analyzed the Friedel oscillation in the metal in a metal-Mott-insulator-metal heterostructure [55]. Oka and Nagaosa even proposed a mechanism for "colossal electroresistance" in systems consisting of metal and strongly correlated materials [56]. Also non-equilibrium currents in a metal-Mott-insulator-metal junction has been studied [57].

Not only heterostructures but also the relation between surface and bulk behavior of strongly correlated materials has given rise to considerable interest. Potthoff and Nolting studied the semi-infinite Hubbard model [20, 58]. They pointed out the possibility of a surface metal-insulator transition. Allowing for a stronger hopping t_{surface} in the surface layer than in the bulk, the surface can be metallic while the bulk is insulating. Liebsch studied surface effects of strongly correlated materials [59] where he finds stronger correlation effects at the surface compared with the bulk. This agrees with one's naive expectation since hopping in the surface layer is suppressed due to the missing neighboring layer. His results are in agreement with experiments [60, 61].

In this chapter we will investigate the junction of a metal and a Mott insulator and the very fundamental question will be studied how the metal penetrates the Mott insulator. At zero temperature, the quasi-particle weight is a good measure for metallic behavior. Here

we will consider a system with a semi-infinite metallic block at $z < 0$ with a defined quasi-particle weight in the bulk, placed in contact with an insulating semi-infinite block at $z > 0$ at an infinite surface at $z = 0$. The only microscopic information in the Hubbard model (2.6) is encoded in the parameters U and t . While we will consider a uniform hopping t , we will choose U for the sites with $z < 0$ in the lattice such that it corresponds to a metal with a finite quasiparticle weight in the homogeneous bulk solution. For sites with $z > 0$, we use $U \sim U_c$ to explore the region around the quantum critical point at $T = 0$ (remind that $U_c = U_{c2}$ at $T = 0$). The main questions are how the quasi-particle weight in the metal near the surface is affected by the presence of the insulator and particularly how the quasi-particle weight decreases in the insulator with increasing distance from the surface. At finite temperatures, the quasi-particle weight is ill-defined and no good measure for metallic behavior exists.

The work presented here, using the generalized DMFT in combination with NRG, represents an improvement for three-dimensional systems from the methodical point of view. Many of the works above studying three-dimensional heterostructures use the generalized DMFT algorithm. However, either simpler models such as the Falicov-Kimball model are considered [55] or more crude impurity solver are used, as, e.g., Potthoff's two-site dynamical mean field theory [62], a simplified exact diagonalization with just one bath site, which is used in Ref. [22, 50].

In the next section we will show how the inhomogeneous DMFT algorithm presented in Chapter 2 can be used to study a heterostructure. Before presenting and discussing the DMFT + NRG results in Section 3.3, we will present a simplified version of the method which can be used to analyze the problem analytically in Section 3.2.

3.1 Inhomogeneous DMFT for a layer structure

In this section we will show how to implement the self-consistency loop (2.18) of the inhomogeneous DMFT to the junction of a metal and a Mott insulator. Let us first specify the system we are going to study. We will consider a three-dimensional cubic lattice consisting out of a metal for ($z < 0$) and a Mott insulator for ($z > 0$), see Fig. 3.1. Thus along the z -axis translation invariance is broken. However, along the layers in x - and y -directions we still have translational invariant infinite planes. So each site in a layer has the same self-energy, which depends only on the z -coordinate.

Considering the self-consistency loop (2.18), we will start with an initial set of self-energies $\{\Sigma(z_i)\}$ for each layer. In the next step, we need to determine the lattice Green's function (2.20). We can perform a Fourier transformation in the x - and y - direction,

the following trick. Using the $N \times N$ unity matrix $\mathbb{1}$, we rewrite $\hat{G}_{\text{lat}}^{-1}(\omega, \epsilon_{\mathbf{k}^{2D}})$ as

$$\begin{aligned}
\hat{G}_{\text{lat}}^{-1}(\omega, \epsilon_{\mathbf{k}^{2D}}) &= \underbrace{\begin{pmatrix} \omega - \Sigma_1(\omega) & t_{\perp} & & & & \\ t_{\perp} & \omega - \Sigma_2(\omega) & t_{\perp} & & & \\ & t_{\perp} & \cdot & & & \\ & & & \cdot & & \\ & & & & t_{\perp} & \\ & & & t_{\perp} & \omega - \Sigma_N(\omega) & \end{pmatrix}}_{\equiv M(\omega)} - \epsilon_{\mathbf{k}^{2D}} \mathbb{1} \\
&= \hat{O}(\omega) M_D(\omega) \hat{O}^T(\omega) - \epsilon_{\mathbf{k}^{2D}} \mathbb{1} \\
&= \hat{O}(\omega) (M_D(\omega) - \epsilon_{\mathbf{k}^{2D}} \mathbb{1}) \hat{O}^T(\omega), \tag{3.2}
\end{aligned}$$

where we introduced the \mathbf{k}^{2D} -independent part $M(\omega)$ of the inverse Green's function's matrix and $\hat{O}(\omega)$ is the orthogonal matrix diagonalizing the complex and symmetric matrix $M(\omega)$, i.e. $M(\omega) = \hat{O}(\omega) M_D(\omega) \hat{O}^T(\omega)$. Now it is simple to invert the expression. We have

$$\begin{aligned}
\hat{G}_{\text{lat}}(\omega, \epsilon_{\mathbf{k}^{2D}}) &= (\hat{O}^T(\omega))^{-1} (M_D(\omega) - \epsilon_{\mathbf{k}^{2D}} \mathbb{1})^{-1} (\hat{O}(\omega))^{-1} \\
&= \hat{O}(\omega) \begin{pmatrix} \frac{1}{EV_1 - \epsilon_{\mathbf{k}^{2D}}} & & & & & \\ & \frac{1}{EV_2 - \epsilon_{\mathbf{k}^{2D}}} & & & & \\ & & \cdot & & & \\ & & & \cdot & & \\ & & & & \cdot & \\ & & & & & \frac{1}{EV_N - \epsilon_{\mathbf{k}^{2D}}} \end{pmatrix} \hat{O}^T(\omega), \tag{3.3}
\end{aligned}$$

where EV_i are the eigenvalues of the matrix $M(\omega)$. Note that since $M(\omega)$ is not hermitian, its eigenvalues will be complex. In the numerical implementation another obstacle exists. The standard available routines (e.g. lapack) for diagonalizing a general complex matrix return a unitary matrix for the change of basis instead of the desired orthogonal matrix. This leads to normalization problems and one is forced to implement the normalization condition $\vec{v} \cdot \vec{v} = 1$ instead of $\vec{v}^* \cdot \vec{v} = 1$ by hand. We have now successfully reduced the problem to diagonalizing the matrix $M(\omega)$ for each value of ω , which is numerically manageable. To obtain the Green's function in coordinate space, what is left to do is taking the Fourier transform in the \mathbf{k}^{2D} -space. Due to the translational invariance along the planes the Green's function does not depend on the position \vec{r}^{2D} in the plane, so we can drop the variable in the notation,

$$\hat{G}_{\text{lat}}(\omega) \equiv \hat{G}_{\text{lat}}(\omega, \vec{r}^{2D}) = \sum_{\mathbf{k}^{2D}} e^{i(\vec{r}^{2D}=0)\mathbf{k}^{2D}} \hat{G}_{\text{lat}}(\omega, \epsilon_{\mathbf{k}^{2D}}) = \int d\epsilon \rho^{2D}(\epsilon) \hat{G}_{\text{lat}}(\omega, \epsilon). \tag{3.4}$$

Here we have chosen $\vec{r}^{2D} = 0$ for the Fourier transformation and replaced the sum by an integral, where $\rho^{2D}(\omega) = \sum_{\mathbf{k}^{2D}} \delta(\omega - \epsilon_{\mathbf{k}^{2D}})$ is the density of states of the dispersion $\epsilon_{\mathbf{k}^{2D}}$. Thus the Green's function only depends on the positions z_i, z_j perpendicular to the

planes, given by the numbers i and j of the planes. Each element $\hat{G}_{\text{lat}}(\omega)_{i,j}$ is given by the (i, j) entry of the matrix

$$\hat{G}_{\text{lat}}(\omega)_{i,j} = \left(\hat{O}(\omega) \int d\epsilon \rho^{2D}(\epsilon) \begin{pmatrix} \frac{1}{EV_1 - \epsilon} & & & \\ & \frac{1}{EV_2 - \epsilon} & & \\ & & \ddots & \\ & & & \frac{1}{EV_N - \epsilon} \end{pmatrix} \hat{O}^T(\omega) \right)_{i,j}. \quad (3.5)$$

For each of the N diagonal entries $\hat{G}_{\text{lat}}(\omega)_{i,i}$ one can now determine the bath function $\mathcal{G}_{0,i}(\omega)$, which is the next step in the self-consistency loop (2.18). Finally one has to solve the N impurity problems defined by $\{\mathcal{G}_{0,i}(\omega)\}$. Here the microscopic parameter U enters the calculation. As already mentioned, we will choose a "metallic" $U_{\text{met}} < U_{c1}$ for the planes with $z < 0$ and a "insulating" U_{ins} for $z > 0$.

3.2 Analytical Study of the Heterostructure

3.2.1 Simplified DMFT equations: Landau equation for the quasi-particle weight

In this section we discuss how one can solve analytically the self-consistency loop discussed in the previous section by making a series of physical approximations. In fact, we will completely neglect the high energy degrees of freedom represented by the Hubbard bands. We will also reduce all low-energy degrees of freedom to only the quasi-particle weight Z of the quasi-particle peak.

The neglect of high energy degrees of freedom is motivated by the following observation. As shown in the left middle panel of Fig. 2.4, in the coexistence regime $U_{c1} < U < U_{c2}$ for $U \rightarrow U_{c2}$ at half-filling the metallic state has already developed a preformed gap. The low energy degrees of freedom, i.e. the quasi-particle resonance, seem to be separated from the high energy degrees of freedom, i.e. the Hubbard bands. In the DMFT self-consistency loop, the Kondo resonance in the impurity model reproduces itself in the sense that the finite value of the Kondo temperature T_K stems mainly from low energy degrees of freedom in the band $\Delta(\omega)$ which are again produced by the Kondo resonance. It is thus tempting to try to separate low and high energy degrees of freedom for $U \rightarrow U_{c2}$. Several works have been made in this direction.

Moeller, Kotliar et al. [63,64] used a Schrieffer-Wolff transformation to decouple the low energy degrees of freedom. By implementing the quasi-particle weight Z as an expansion parameter, anticipating that Z depends linearly on $U - U_{c2}$ as $U \rightarrow U_{c2}$, they arrived at self-consistency equations which they solved numerically. With this method (which they termed "projective self-consistent technique") they were able to determine susceptibilities as well as thermodynamic properties. However, they were not able to make a statement

about the region in which the assumption $Z \propto (U - U_{c2})$ is valid. Moreover, in this Section we are looking for a even simpler scheme where not only the high energy degrees of freedom are integrated out but also the low energy degrees of freedom are approximately described by only the quasi-particle weight Z . Zhang, Kotliar et al. [65] identified Z as the only relevant low-energy scale close to the transition, corresponding to the Kondo temperature T_K in the Anderson impurity problem. Clearly, $Z = 0$ in the insulator while it becomes finite in the metal. Since in the metallic Fermi liquid regime the quasi-particle peak is pinned, cf. Eq. (2.16), the quasi-particle weight Z is directly related to the width Δ of the peak. We will now present the derivation of Zhang, Kotliar et al. [65] of a simplified DMFT self-consistency equation, where only a single low energy degree of freedom is considered, represented by Δ . In Ref. [65], a Bethe lattice is considered, which, in the limit of infinite dimensions, has a semicircle density of states, $\rho(\epsilon) = (2/\pi D) [1 - (\epsilon/D)^2]^{1/2}$. In this particular case the DMFT self-consistency equation simplifies to [10]

$$\mathcal{G}_0^{-1}(i\omega_n) = i\omega_n - t^2 G_{\text{lat}}(i\omega_n). \quad (3.6)$$

In this chapter a heterostructure in a three-dimensional cubic lattice is studied, which has a density of states differing from $\rho(\epsilon)$. However, since we are focused on the low-energy limit we expect that the self-consistency equation will hold independent of the choice of the lattice. The authors of [65] proceed by using Eq. (3.6) with the spectral representation of the lattice Green's function,

$$\mathcal{G}_0^{-1}(z) = z - (D^2/4) \int \frac{A(\epsilon)}{z - \epsilon} d\epsilon, \quad (3.7)$$

where $A(\omega) = -(1/\pi)\text{Im}G_{\text{lat}}(\omega)$. The spectral function, looking at Fig. 2.4, can be approximated by a Lorentzian with width Δ . The weight of the Lorentzian is fixed by $\mathcal{G}_0^{-1}(0 + i\delta)$ which is given by $-\text{Im}\mathcal{G}_0(0 + i\delta) = \pi\rho(0) = 2/D$ in the case of the Bethe lattice. Neglecting the two Hubbard bands, one obtains

$$\mathcal{G}_0^{-1} = z - \frac{D\Delta}{z + i\Delta\text{sgn}z}, \quad (3.8)$$

which was checked to be a good approximation to full numerical solutions by the authors of Ref. [65]. The dependence of the self-energy on Δ is now determined with the help of Eq. (2.35) making use of the IPT approximation for the self-energy. For low frequencies one arrives at

$$\text{Re}\Sigma(\omega) = -\frac{U^2\omega}{9(D\Delta - \Delta^2/2)}, \quad (3.9)$$

see Ref. [65] for details. On the other hand, using equation (2.13) in case of the Bethe lattice, one can show that in linear order in ω [65]

$$\text{Re}\Sigma(\omega) = (D/\Delta)\omega. \quad (3.10)$$

Regarding the last two equations as a ‘‘self-consistency loop’’ for Δ , the authors of Ref. [65] obtain the final result

$$\Delta_{N+1} = \frac{9D}{U^2} (D\Delta_N - \Delta_N^2/2). \quad (3.11)$$

In the spirit of Landau's theory describing classical phase transitions, Eq. (3.11) represents the Ginzburg-Landau-functional describing the transition in terms of the "order parameter" Δ . However, Δ is no real order parameter and fails to describe the MMIT at finite temperatures, since it is directly related to the quasi-particle weight Z , which is ill-defined at finite temperatures. In Ref. [66], also Bulla and Potthoff managed to describe the MMIT in terms of the quasi-particle weight Z , which they refer to as "linearized DMFT". They use a single pole structure to parameterize the bath function, equivalent to Eq. (3.8), identifying the corresponding impurity model as a two-site Anderson impurity model which they solve analytically. They arrive at the following self-consistency equation for the quasi-particle weight,

$$Z_{N+1} = \frac{36t^2q}{U^2}Z_N, \quad (3.12)$$

where q is the connectivity of the lattice. Since Z converges to zero or to infinity for $U < 6t\sqrt{q}$ or $U > 6t\sqrt{q}$, corresponding to the metallic or insulating solution, respectively, one concludes that in the linearized DMFT $U_c \equiv 6t\sqrt{q}$, which turns out to be a good approximation compared with full numerical solutions [66]. Since one can only draw useful conclusions from Eq. (3.12) for $U = U_{c2}$, Potthoff and Nolting generalize it by simply considering the next term in an expansion in the "order parameter" Z in the Landau spirit [20]. They obtain

$$Z_{N+1} = \frac{U_c^2}{U^2}Z_N - aZ_N^2 \quad (3.13)$$

with a not yet defined constant a . Eqns. (3.11) and (3.13) are equivalent up to an important difference. Replacing Δ by Z in Eq. (3.11) and considering the metallic converged solution $Z_{N+1} = Z_N$, Eq. (3.11) gives $Z \propto (1 - U^2/U_c^2)$ while Eq. (3.13) gives $Z \propto \text{const} - U_c^2/U^2$. Thus for both equations the quasi-particle weight vanishes linear for $U \rightarrow U_{c2}$. However, for the former equation the second derivative of $Z(U)$ close to the transition is negative, contradicting several numerical results, see e.g. Ref. [19]. By expanding the solution of Eq. (3.13) around U_c , one obtains

$$Z = -\frac{2}{U_{c2}a}(U - U_c) + O((U - U_c)^2). \quad (3.14)$$

From DMFT/NRG results for a Bethe lattice one can extract $a \approx 7$ [19].

3.2.2 Application of the simplified DMFT to the Heterostructure

We will now apply a simplified version of the inhomogeneous DMFT described in Section 3.1 to the heterostructure, where we use the quasi-particle weight Z as the only degree of freedom, following the reasoning above. Considering our layer structure, we will have different quasi-particle weights $Z(i)$ for each layer. In the following we will first parameterize the self-energy $\Sigma(\omega)$ in terms of $Z(i)$. Since we are interested in the low-energy physics close to the transition where $Z(i) \rightarrow 0$ and the quasi-particle peak is sharply peaked at low frequencies, we will use a low-frequency expansion of the self-energy and keep only the

once can identify the c_n with the $(n - 1)$ th moment of the imaginary part of the Green's function, i.e. the quasi-particle peak, $c_n(i) = \int dx A_i(x) x^n$. The expansion (3.19) gives

$$\begin{aligned} c_0(i) &= Z(i), \\ c_1(i) &= Z^2(i) \int d\epsilon \rho^{2D}(\epsilon) \epsilon, \\ c_2(i) &= Z^2(i) \left(Z(i) \int d\epsilon \rho^{2D}(\epsilon) \epsilon^2 + t_{\perp}^2 (Z(i-1) + Z(i+1)) \right). \end{aligned} \quad (3.22)$$

These are the first three moments of the quasi-particle peak, which are captured correctly in the second order approximation (3.19). As claimed above, the zeroth moments $\{c_0(i)\}$, i.e. the quasi-particle weights, are unchanged by the inversion in comparison with the set $\{Z(i)\}$ parameterizing the self-energies. Since the density of states ρ^{2D} is symmetric, $\int d\epsilon_{\mathbf{k}^{2D}} \epsilon_{\mathbf{k}^{2D}} = 0$, which agrees with the fact that also the spectral function $A_i(\omega)$ is symmetric and thus the first moments vanish. As mentioned above, the second moments $\{c_2(i)\}$ do have contributions from the neighboring sites. Here $Z(i) \int d\epsilon \rho^{2D}(\epsilon) \epsilon^2 = Z(i) 4t_{\parallel}^2$ for the two-dimensional cubic lattice, where t_{\parallel} is the in-plane hopping. This represents the contributions of the four sites in the same plane with the same quasi-particle weight $Z(i)$.

If one considers a homogeneous material with quasi-particle weight Z and hopping t , one obtains $c_2 = Z^3 6t^2 \Leftrightarrow Z = c_2^{1/3} / (6t^2)$. To translate the second moments back to quasi-particle weights, we will thus use

$$Z'(i) = \frac{1}{4t_{\parallel}^2 + 2t_{\perp}^2} \left(Z^2(i) (4t_{\parallel}^2 Z(i) + t_{\perp}^2 (Z(i-1) + Z(i+1))) \right)^{1/3}. \quad (3.23)$$

The quasi-particle weights $\{Z'(i)\}$ can be used in order to parameterize the bath functions $\{\mathcal{G}_{0,i}\}$, cf. Eq. (3.8). Thus we can now finally apply Eq. (3.13) as an toy impurity solver to obtain a new set of quasi-particle weights $\{Z(i)\}$, which give a new set of self-energies $\{\Sigma_i\}$ via Eq. (3.15).

3.2.3 Results

Before presenting the full numerical results in the next section, we will study the solution of the analytical method presented in this section. As a first useful application, let us determine the critical exponent of the algebraic decay of the quasi-particle weight in an insulator at critical $U_{\text{ins}} = U_c$ (in the following we will use U_C since at $T = 0$, $U_c = U_{c2}$). Afterwards we will study the universal scaling behavior of the quasi-particle weight in the insulator for $U_{\text{ins}} < U_c$ and $U_{\text{ins}} > U_c$.

We will consider a system with uniform hopping $t_{\perp} = t_{\parallel} = t$, a semi-infinite block of metal with $U_{\text{met}} \ll U_c$ at $z < 0$ and a semi-infinite block of insulator with $U_{\text{ins}} = U_c$ at $z > 0$. Let us introduce the separate notation $Z_{\text{met}}(n)$ and $Z_{\text{ins}}(n)$ for the quasi-particle weight in the metal and in the insulator, respectively, where n is the numbers of layers, starting counting from the junction. Anticipating an algebraic decay of $Z_{\text{ins}}(n)$ in the

insulator at criticality, $Z_{\text{ins}}(n) = c/n^x$ with a constant c and exponent x , Eq. (3.23) gives

$$Z'_{\text{ins}}(n) = \frac{1}{6t^2} \left(\left(\frac{c}{n^x} \right)^2 \left(4\frac{c}{n^x} + \frac{c}{(n-1)^x} + \frac{c}{(n+1)^x} \right) \right)^{1/3}. \quad (3.24)$$

Using Eq. (3.13) to obtain the new quasi particle weight $Z_{\text{ins}}(n)$ and expanding in powers of $\frac{1}{n}$ around $n = \infty$, one obtains

$$\begin{aligned} Z_{\text{ins}}(n) &= Z'_{\text{ins}}(n) - a(Z'_{\text{ins}}(n))^2 \\ &= \frac{1}{6}n^{-2x} \left[n^x \left(6c + \frac{1}{3}cx(1+x) \left(\frac{1}{n} \right)^2 + O\left(\frac{1}{n} \right)^3 \right) + \right. \\ &\quad \left. \left(-6ac^2 - \frac{2}{3}(ac^2x(1+x) \left(\frac{1}{n} \right)^2 + O\left(\frac{1}{n} \right)^3) \right) \right]. \end{aligned} \quad (3.25)$$

The lowest order is c/n^x , as expected. In order for the next order to vanish,

$$\frac{1}{6}n^{-2x} \left(\frac{1}{3}cx(1+x)n^{x-2} - 6ac^2 \right) \stackrel{!}{=} 0. \quad (3.26)$$

We conclude that $x = 2$ and $\frac{2}{3}6c = 12ac^2 \Leftrightarrow c = \frac{1}{3a}$.

For a system with $U_{\text{met}}/U_c = 0.6$, $U_{\text{ins}} = U_c$ and 500 layers each of metal and insulator, the quasi-particle weight is shown in Fig. 3.2. While the quasi-particle weight in the metal $Z_{\text{met}}(n)$ is not affected by the presence of the insulator and corresponds to the bulk value, the quasi-particle weight in the insulator $Z_{\text{ins}}(n)$ decays as $1/(3an^2)$, in agreement with the prediction above. Thus, at $T = 0$, the metal penetrates infinitely deep into the insulator. This may be surprising, especially if one expects U to be the relevant scale in the insulator. One can understand this behavior by the following argument. Since we neglected magnetic ordering, the insulating phase consists out of free spins. After the mapping to the impurity model in the self-consistency loop, the free spins will be coupled to the different bathes representing the other sites. At zero temperature, a considered site will be metallic if the Kondo temperature T_K is finite. This is the case if one couples the metal to the insulator. The sites next to the metal will become metallic and provide a metallic bath for the next layer, and so on. One can understand the penetration as a decay of T_K , which becomes smaller going away from the junction since $U \geq U_c$ in the insulator.

If one considered magnetic ordering, the relevant scale in the insulator would be the coupling between the spins $J \propto t^2/U$. A site with metallic environment stays insulating, if the Kondo temperature in the impurity model is smaller than the coupling. In this case the penetration would stop if the Kondo temperature and the coupling become of the same order. This is also the case for finite temperatures in the paramagnetic solution, where the penetration stops when the temperature and the Kondo temperature are of the same order.

One expects to find universal scaling behavior in a region around U_c . For $U_{\text{ins}} \lesssim U_c$, one has, strictly speaking, two neighboring metals. However, let us keep the subscript ‘‘ins’’

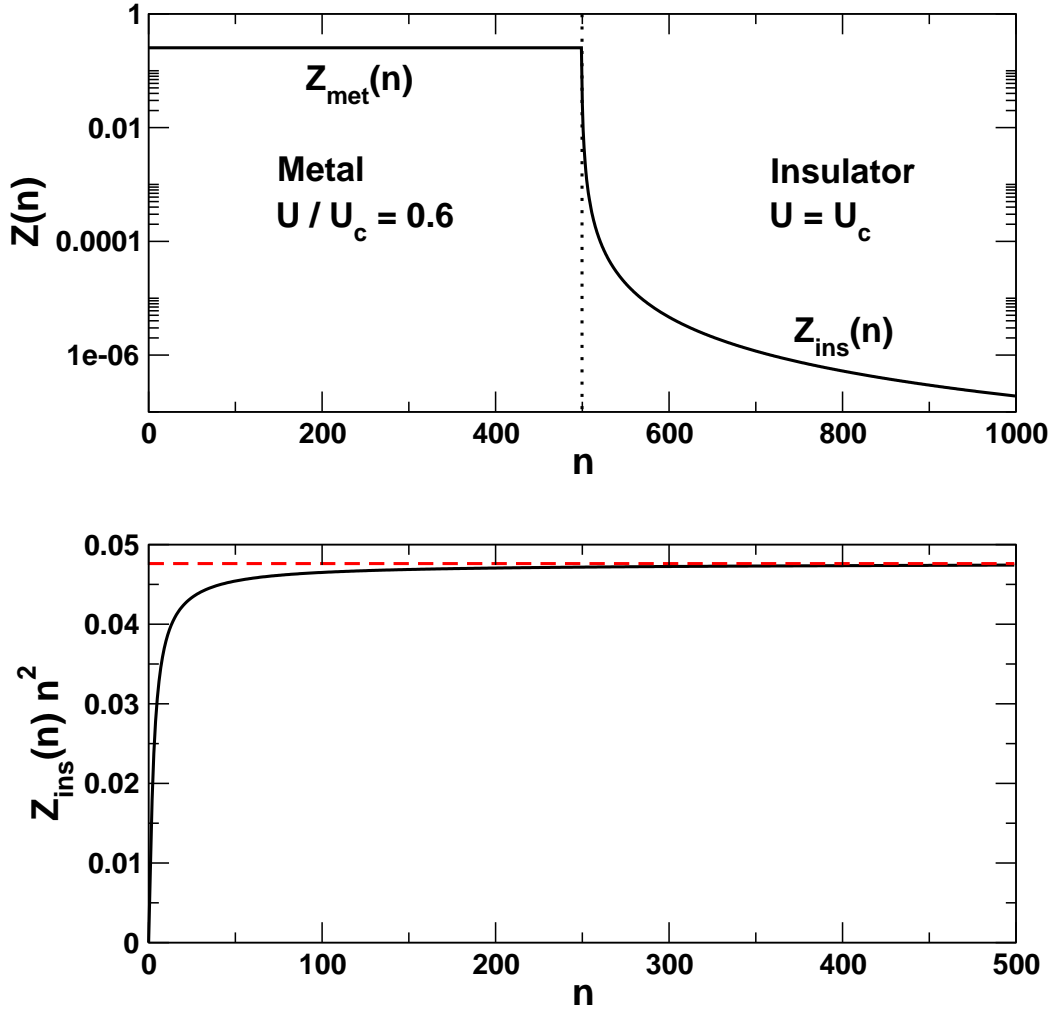


Figure 3.2: The quasi-particle weight $Z(n)$ for a system of 1000 layers, where the left 500 are metallic, $U_{\text{met}}/U_c = 0.6$, and the right 500 are insulating, $U_{\text{ins}} = U_c$, calculated with the simplified DMFT method with $a = 7$. (a) The constant quasi-particle weight $Z_{\text{met}}(n) = 0.25$ in the metallic regime agrees with the bulk value in a infinite system. The metallic regime penetrates into the insulator, where $Z_{\text{ins}}(n)$ decays algebraically. (b) $Z_{\text{ins}}(n)$ in the insulator, multiplied by n^2 . Sufficiently far in the insulator, where the sub-leading terms play no role, $Z_{\text{ins}}(n)n^2 = c = 1/3a$, in agreement with the predictions (see text).

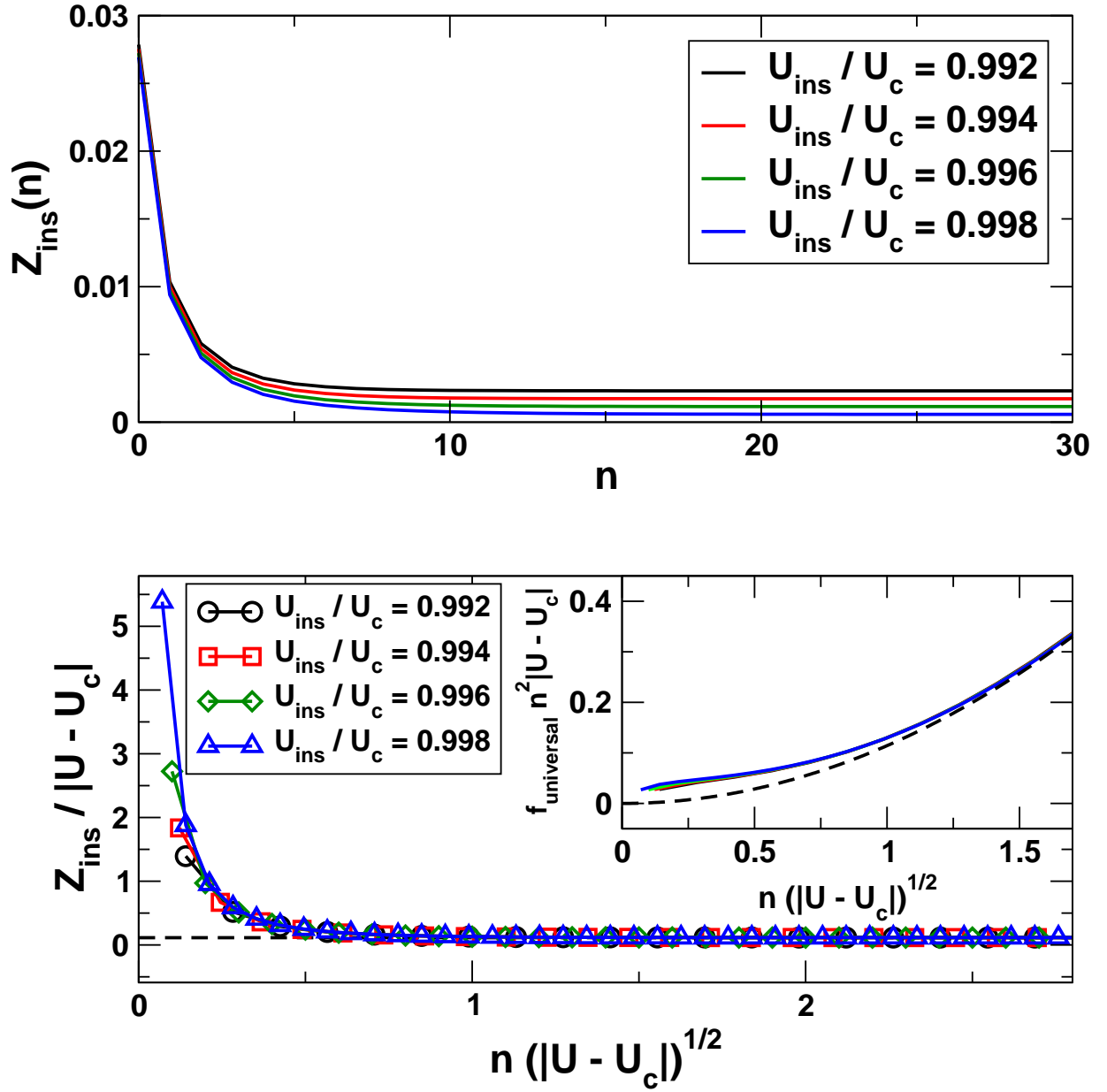


Figure 3.3: The quasi-particle weight Z for a system of 200 layers, where the left 100 are metallic, $U_{\text{met}}/U_c = 0.6$, and the right 100 are close to the insulating regime, $U_{\text{ins}} \lesssim U_c$, calculated with the simplified DMFT method with $a = 7$. Top panel: $Z_{\text{ins}}(n)$ decays as $1/n^2$ until the bulk value of the bad metal is reached. Bottom panel: The curves do collapse to one single curve $Z_{\text{ins}}/|U_{\text{ins}} - U_c| = f_{\text{universal}}$ if scaled according to Eq. (3.27). As predicted by Eq. (3.14), all curves reach the constant value $2/(aU_c) \approx 0.057/D$ (dashed line, $U_c = 2.5D$ in units of bandwidth). Inset: $(Z_{\text{ins}}/|U_{\text{ins}} - U_c|) n^2 |U_{\text{ins}} - U_c|$ reaches the constant $1/(3a) \approx 0.048$ for small n . For $n \gg 1$, $Z_{\text{ins}}/|U_{\text{ins}} - U_c| = f_{\text{universal}}$ converges to $2/(aU_c)n^2$ (dashed line).

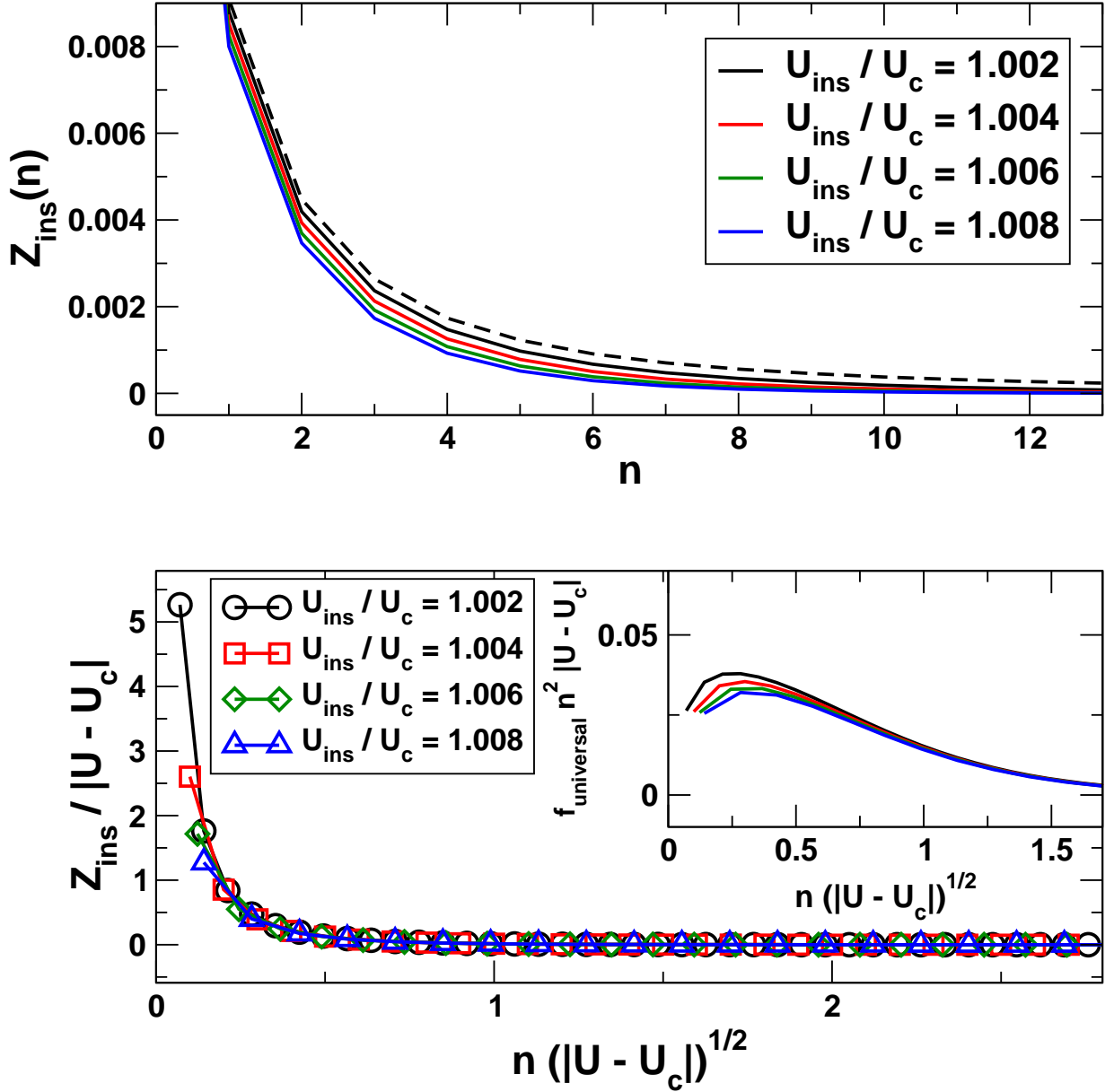


Figure 3.4: The quasi-particle weight Z for a system of 200 layers, where the left 100 are metallic, $U_{\text{met}}/U_c = 0.6$, and the right 100 are close to the insulating regime, $U_{\text{ins}} \gtrsim U_c$, calculated with the simplified DMFT method with $a = 7$. Top panel: $Z_{\text{ins}}(n)$ decays faster than the critical curve $1/(3an^2)$ (dashed line). Bottom panel: The curves do collapse to one single curve $Z_{\text{ins}}/|U_{\text{ins}} - U_c| = f_{\text{universal}}$ if scaled according to Eq. (3.27). Inset: $f_{\text{universal}} n^2 |U_{\text{ins}} - U_c|$ reaches the constant $1/(3a) \approx 0.048$ for small n .

for the “bad” metal at $z > 0$. The two metals have different quasi-particle weight bulk values Z_{met} and Z_{ins} . As in the case $U_{\text{ins}} = U_c$, one finds that $Z_{\text{met}}(n)$ is not affected by the presence of the bad metal. The good metal penetrates into the bad metal, where $Z_{\text{ins}}(n)$ decays as $1/n^2$ until the bulk value of the bad metal is reached, see Fig. 3.3. As shown in the lower panel of Fig. 3.3, curves for different values of U_{ins} do indeed collapse to one single curve $Z_{\text{universal}}$ if they are scaled. Close to U_c , $Z_{\text{ins}}/|U_{\text{ins}} - U_c| = 2/(aU_c) = \text{const.}$ according to Eq. (3.14). Since $y = \text{const. } 1/x^2 \Rightarrow y/c = \text{const. } 1/(xc^{1/2})^2$ for a constant c , we use the following scaling

$$Z_{\text{ins}} = |U_{\text{ins}} - U_c| f_{\text{universal}} \left(n \sqrt{|U_{\text{ins}} - U_c|} \right). \quad (3.27)$$

As expected the universal behavior also holds for $U_{\text{ins}} > U_c$, as shown in Fig. 3.4.

Since the insulating layers ($z > 0$) have no influence on the metallic layers ($z < 0$), the physics discussed in this Section are very similar to the results found by Potthoff et al. [20], who studied an insulating semi-infinite bulk with a metallic surface. Using Eq. (3.13), they investigate how the metallic regime at the surface penetrates into the bulk. However, they made no comments on the critical exponents and were not able to supplement their analytical results of their toy model with full numerical results.

3.3 DMFT/NRG results

The inhomogeneous DMFT method for the layer system of Section 3.1 was implemented with NRG as an impurity solver. To simulate the heterojunction of the metal and the insulator, 80 layers are used, where the left half is metallic with $U_{\text{met}} = 1.0D \ll U_c \approx 2.794D$. The numerics are plagued with severe convergence problems. One source of the problematic convergence behavior could be identified as the logarithmic divergence of the two-dimensional density of states $\rho^{2D}(\omega)$ of the planes. Since a finite number of 80 layers is considered, the logarithmic divergence is reproduced in the three-dimensional density of states $\rho(\omega) = \sum_{n_z=0}^{79} \rho^{2D}(\omega - \cos(2\pi n_z/80 - \pi))$, see Fig. 3.5. Since we are not interested in a particular choice of lattice but in the universal scaling behavior, we replace the two-dimensional density of states by a constant, $\rho^{2D} \equiv 3/(4D)$. This leads to a smooth three-dimensional density of states, which improves the convergence significantly, see Fig. 3.5. Another problematic issue is the difference of energy scales in the metal and in the insulator. The quasi-particle weight $Z(n)$ is determined by evaluating the slope of the real part of the self-energy at $\omega = 0$,

$$Z(n) = \left(1 - \frac{\partial}{\partial \omega} \text{Re} \Sigma_n(\omega) \Big|_{\omega=0} \right)^{-1}. \quad (3.28)$$

To evaluate the slope numerical, one has to discretize the derivation, $\frac{\partial}{\partial \omega} \text{Re} \Sigma_n(\omega) \Big|_{\omega=0} \approx \Delta \text{Re} \Sigma / \Delta \omega$. The choice of $\Delta \omega$ is problematic for the following reason. The NRG is not reliable for energies much smaller than the Kondo temperature [47], $\omega \ll T_K$, where all calculated quantities show unphysical behavior. In a single NRG run or in a bulk DMFT

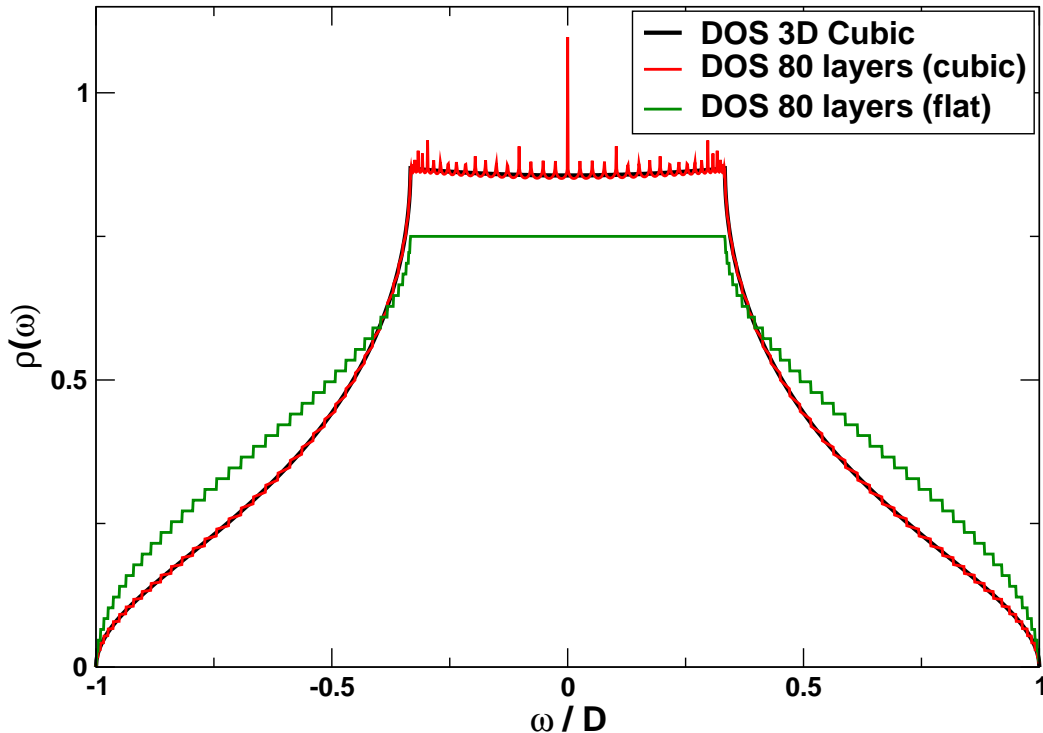


Figure 3.5: Densities of states (DOS) of the following 3 three-dimensional lattices. The black curve corresponds to a cubic lattice. The red curve refers to a system consisting of 80 layers, where the two-dimensional layers have a cubic lattice structure with the two-dimensional DOS $\rho_{\text{cubic}}^{2D}(\omega)$. The logarithmic divergence of $\rho_{\text{cubic}}^{2D}(\omega)$ is reproduced in the three-dimensional DOS of the 80 layers (red curve). All spikes are logarithmic divergencies, which are cut off in the figure. These divergencies seriously impede the convergence of the numerical DMFT solution. If one assumes that the layers have a flat two-dimensional DOS, $\rho_{\text{flat}}^{2D}(\omega) = 3/(4D)$, then the corresponding three-dimensional DOS of a system consisting out of 80 layers is smooth (green curve).

implementation one usually stops the algorithm by limiting the shells, once the strong coupling fixed point is reached. Since one impurity solver is used for all layers, this is not possible here. To obtain reliable results for Z , $\Delta\omega = 10^{-3}$ and $\Delta\omega = 10^{-7}$ are chosen for the metallic and the insulating regime, respectively. However, this does not resolve the problematic behavior of all quantities for $\omega \ll T_K$ in the metallic regime. Here oscillatory behavior appears to destabilize the convergence. Since, as in the simplified DMFT version, the quasi-particle weight Z_{met} in the metal for $z < 0$ is not affected by the presence of the insulator, in the numerical implementation the self-energies in the metallic regime are kept fixed for a certain number of DMFT loops and only the insulating regime are allowed to vary.

For the case $U_{\text{ins}} < U_c$, at least several hundreds DMFT iterations are needed to reach satisfactory convergence (results between two iterations differ only in the order of machine

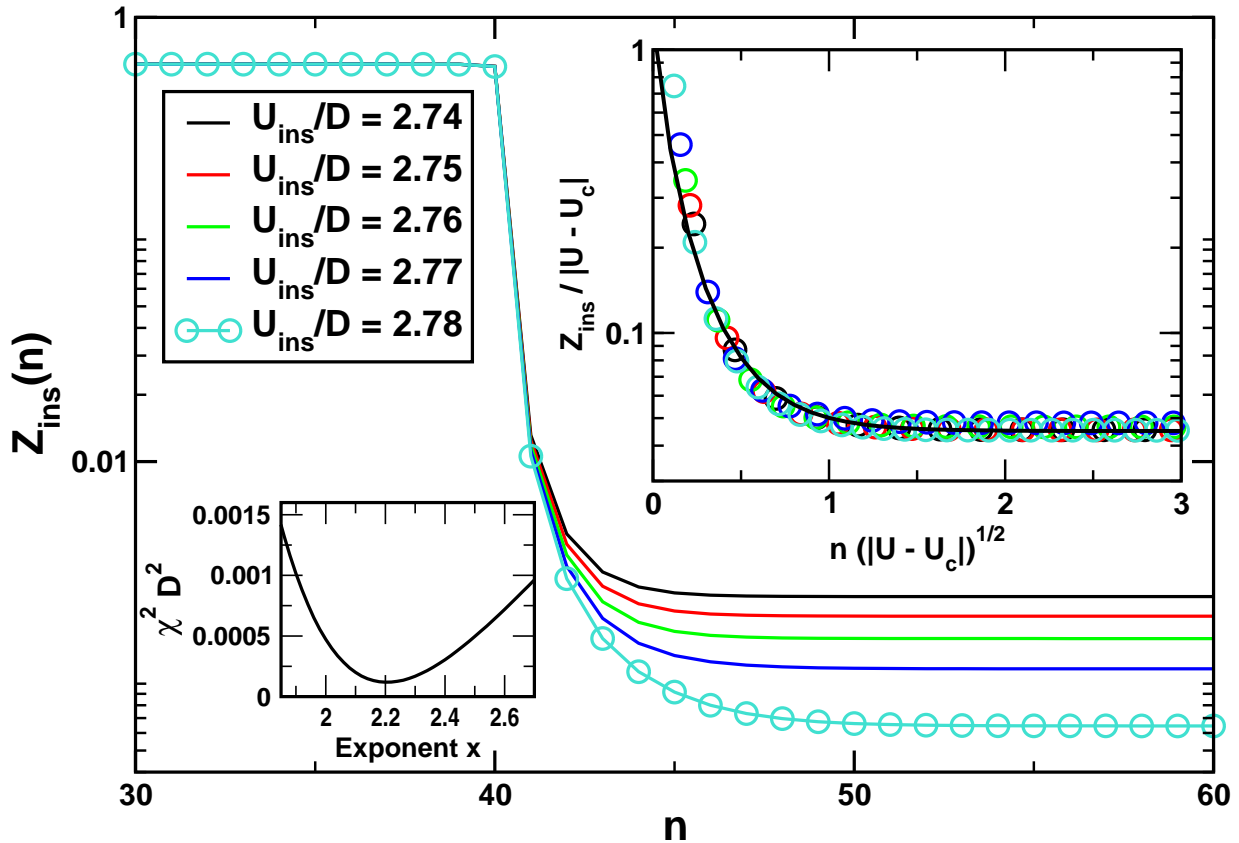


Figure 3.6: (corresponding to Fig. 3.3) The quasi-particle weight Z for a system of 80 layers, where the left 40 are metallic, $U_{\text{met}}/D = 1.0$, and the right 40 are close to the insulating regime, $U_{\text{ins}} \lesssim U_c$ ($U_c/D \approx 2.794$), calculated with DMFT/NRG ($\Lambda = 2.0$, 60 shells, 1600 kept states). Main panel: $Z_{\text{ins}}(n)$ decays as $1/n^2$ until the bulk value of the bad metal is reached. Top right inset: The curves do collapse to one single curve if scaled according to Eq. (3.27). The decay is slightly faster compared to the toy model calculation (black line, where $a = 16$ and $U_c = 2.79$ were extracted from the full numerical results). Bottom left panel: the exponent x of the decay $1/n^x$ is slightly larger than two, see text.

precision). The quasiparticle weights in the insulator Z_{ins} for $\Lambda = 2.0$, 60 shells, 1600 kept states and for different values of U_{ins} are shown in Fig. 3.6. The results nicely confirm the expectations from the toy model calculation, cf. Fig. 3.3. Close to the metallic boundary, Z_{ins} decays as $1/n^2$ until the bulk value of the “insulator” (i.e. the quasi-particle weight of the “bad” metal) is reached. From the linear behaviour in $U - U_c$ of these bulk values, one can extract $U_c = 2.794D$. If scaled according to Eq. (3.27), the curves collapse to one single curve with a high precision (upper right panel of Fig. 3.6). To verify the exponent $x = 2$ of the decay $1/n^x$, the curves are scaled according to

$$Z_{\text{ins}} = |U_{\text{ins}} - U_c| f_{\text{universal}} \left(n (|U_{\text{ins}} - U_c|)^{1/x} \right). \quad (3.29)$$

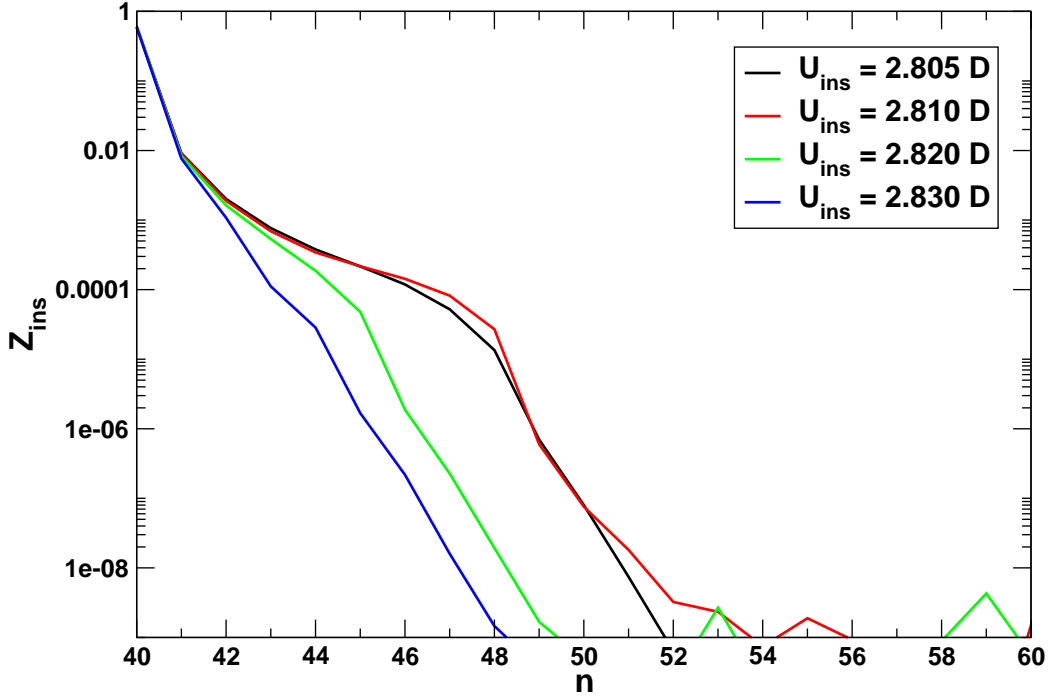


Figure 3.7: Figure corresponding to Fig. 3.4: The quasi-particle weight Z_{ins} for a system of 80 layers, where the left 40 are metallic, $U_{\text{met}}/D = 1.0$, and the right 40 are close to the insulating regime, $U_{\text{ins}} \gtrsim U_c$ ($U_c \approx 2.794D$), calculated with DMFT/NRG ($\Lambda = 2.0$, 60 shells, 1600 kept states). The qualitative behavior appears to be correct: $Z_{\text{ins}}(n)$ decays as $1/n^2$ until it starts to fall off exponentially. Since 60 shells were used, only energies down to approx. $10^{-8}D$ can be resolved. Values of Z below approx. 10^{-8} can thus be disregarded as numerical noise. Obviously the curves fail to collapse on a single curve if scaled according to Eq. (3.27).

The scaled data points $\{x_i, y_i\} = \{n(|U - U_c|)^{1/x}, Z_{\text{ins}}/|U - U_c|\}$ are fitted with a function $F(x_i)$ and the deviation of the data points from the fitting function is determined, $\chi^2 = \sum_i (y_i - F(x_i))^2$. The results are shown in the bottom left inset of Fig. 3.6. The optimal exponent x is slightly larger than two, $x \approx 2.2$.

For $U_{\text{ins}} > U_c$, the results appear to be qualitatively correct. The curves for different values of U_{ins} are depicted in Fig. 3.7. For values of U_{ins} close to U_c , $U_{\text{ins}} = 2.805D$ and $U_{\text{ins}} = 2.81D$, one observes the $1/n^2$ decay close to the junction until an exponential decay sets in. The curves for $U_{\text{ins}} = 2.82D$ and $U_{\text{ins}} = 2.83D$ seem to fall off exponentially and a power-law decay can, if at all, only be suspected. This meets one's expectations: deep in the insulating regime $U_{\text{ins}} \gg U_c$, one anticipates an exponential decay. In the spirit of the toy model, the quasiparticle weight $Z(n)$ in layer n , which translates to the Kondo temperature T_K in the corresponding impurity model, is both the result of the quasiparticle weight in the layer $n - 1$ and the source for the quasi-particle weight in layer $n + 1$. Since the Kondo temperature is exponentially suppressed for large U , the Kondo temperatures

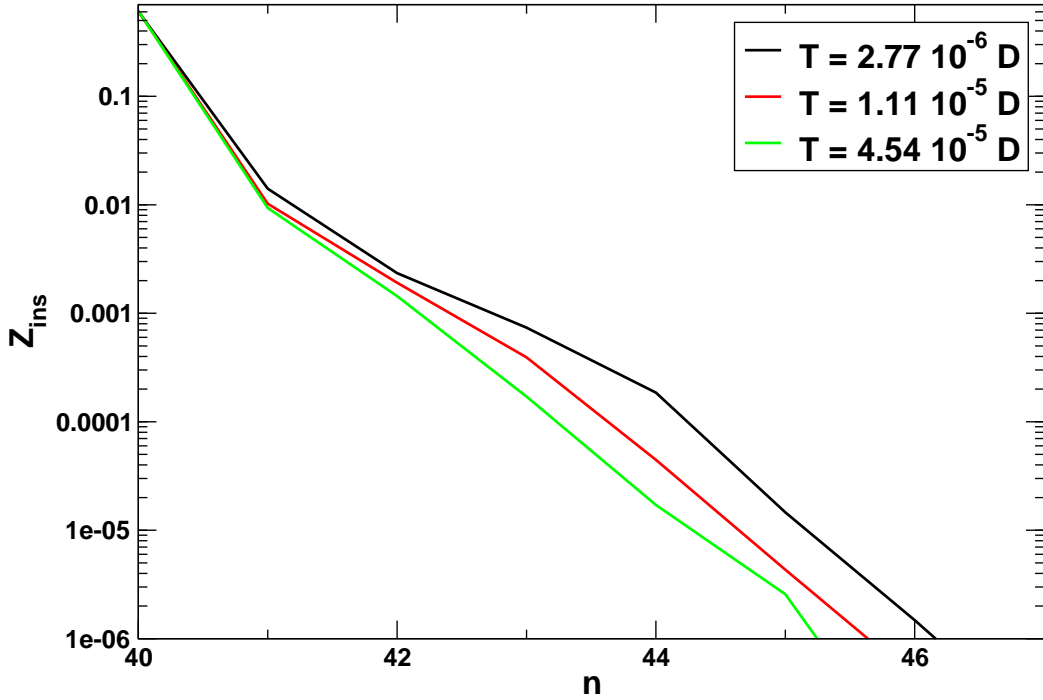


Figure 3.8: The quasi-particle weight Z_{ins} for a system of 80 layers (where the left 40 are metallic, $U_{\text{met}}/D = 1.0$) at $U_{\text{ins}} = U_c \approx 2.794D$ at finite temperatures, calculated with DMFT/NRG ($\Lambda = 2.0$, 60 shells, 1600 kept states). Similar to Fig. 3.7, the curves decrease as $1/n^2$ close to the junction before falling off exponentially. Obviously the curves fail to collapse on a single curve if scaled according to Eq. (3.27).

will decrease exponentially going along the layers, corresponding to an exponential decay of $Z(n)$. For $U_{\text{ins}} \rightarrow U_c$, one expects to recover the power-law decay. However, no scaling behavior could be found, see Fig. 3.7. Neither different choices of Λ , $\Lambda = 1.5, 2.0, 3.0$, nor varying the number of shells between 50 and 90 depending on Λ , nor increasing the number of kept states up to 2400 lead to a satisfactory solution. The same convergence problems are encountered at finite temperatures for $U_{\text{ins}} = U_c$. Here, in addition, the quasi-particle peak is smeared out and hence the quasi-particle weight is ill-defined. Since the Kondo temperature is suppressed exponentially by finite temperature, one expects the same behavior as in the $U_{\text{ins}} > U_c$ case. Curves for different temperatures are shown in Fig. 3.8.

Chapter 4

Phase separation

In Chapter 2, we have discussed the Mott metal-insulator transition (MMIT) at half filling $n = 1/2$. Since, at temperature $T > 0$, the MMIT is a first-order transition, it will be stable against a small doping δ of the filling, $n \rightarrow 1/2 \pm \delta$. As we will show in the following, this will lead to a phase separation between metallic and insulating domains, which have different fillings. The ionic background charge is uniform, hence long-range Coulomb forces will suppress the formation of macroscopic domains. This fact can be understood by considering the electrostatic energy

$$U_{\text{Coulomb}} = \int d^3r d^3r' \frac{\rho(\mathbf{r})\rho(\mathbf{r}')}{|\mathbf{r} - \mathbf{r}'|} = \frac{1}{8\pi} \int d^3r |\mathbf{E}(\mathbf{r})|^2. \quad (4.1)$$

Let us, e.g., regard a system of two plates infinitely extending into the x - and y -direction with infinite area A and thickness L in the z -coordinate. Assuming that both plates have opposite charge Q and $-Q$, respectively, where the charge is homogeneously distributed with charge density ρ_{const} , the electric field has the form

$$\mathbf{E}(z) = \begin{cases} 4\pi\rho_{\text{const}}(L - |z|) & \text{for } |z| < L \\ 0 & \text{elsewhere.} \end{cases} \quad (4.2)$$

Using Eq. (4.1), we see that the electrostatic energy diverges as L^5 in a macroscopic system. Thus, unlike boiling water in a pot, the electronic charge will not show macroscopic phase separation. A possible scenario is microphase separation of domains which are of the order of several lattice constants. The competition of the Coulomb force and the energy cost of domain walls will determine the size of the domains.

Since every reader is familiar with the van der Waal's gas, let us revisit the Maxwell construction for first order phase transitions using the example of the fluid-gas transition. Identifying the fluid with the metal phase, the gas with the insulating phase, the filling n with the volume per particle v and the chemical potential μ with the pressure P , it turns out that knowledge from the fluid-gas transition can directly be applied to the MMIT. Finally we study the domain structure with the inhomogeneous DMFT method, including the Coulomb forces.

4.1 Maxwell construction for first order phase transitions

4.1.1 Fluid-gas transition

As shown in every textbook on statistical mechanics and thermodynamics, see, e.g., [67], the virial expansion of the pressure P in the density up to second order gives the van der Waal's equation of state,

$$P + \frac{a}{v^2} = \frac{k_B T}{v - b}, \quad (4.3)$$

where P is the pressure, $v = V/N$ is the volume per particle, and a and b are positive parameters. Below a critical temperature $T = T_c$, the isotherm has a minimum, see Fig. 4.1. Since the compressibility at fixed temperature $\kappa_T = -\frac{1}{V} \left(\frac{\partial V}{\partial P} \right)_T$ must be positive, it follows that $\left(\frac{\partial P}{\partial V} \right)_T < 0$. Thus the part of the isotherm with positive slope corresponds to a mechanical unstable phase and hence is unphysical. In terms of the free energy per particle $f = F/N$,

$$f(T, v) = f(T, v_a) - \int_{v_a}^v dv' P(T, v'), \quad (4.4)$$

this condition translates to $\frac{1}{\kappa_T V} = - \left(\frac{\partial^2 F}{\partial V^2} \right)_{T, N} > 0$, i.e. the curvature of the free energy must be positive. If one plugs Eq. (4.3) into Eq. (4.4), one obtains curves with negative curvatures, cf. Fig. (4.1), corresponding to the regions with positive slope of $P(v)$. The way out is the well-known Maxwell construction. One identifies the steep slope of $P(v)$ at small v as the behavior of a fluid, whereas the part at large v represents the gaseous phase. The first order phase transition between the two phases takes place at a pressure P_0 . We know that the chemical potential μ stays constant, $\mu_{\text{fluid}}(T, P_0) = \mu_{\text{gas}}(T, P_0)$. Since $\mu = G/N = F/N + PV/N = f + Pv$, we have

$$f_{\text{fluid}} - f_{\text{gas}} = P_0(v_{0,\text{gas}} - v_{0,\text{fluid}}). \quad (4.5)$$

Using Eq. (4.4), we have $P_0(v_{0,\text{gas}} - v_{0,\text{fluid}}) = \int_{v_{0,\text{fluid}}}^{v_{0,\text{gas}}} P(T, v) dv$, which determines the value of P_0 . In the region $v_{0,\text{fluid}} < v < v_{0,\text{gas}}$ phase separation occurs, where the fraction $c_{\text{fluid}}(v)$ is in the fluid phase in the fraction $c_{\text{gas}}(v)$ is in the gaseous phase, with

$$c_{\text{fluid}}(v) = \frac{v_{0,\text{gas}} - v}{v_{0,\text{gas}} - v_{0,\text{fluid}}}, \quad c_{\text{gas}}(v) = \frac{v - v_{0,\text{fluid}}}{v_{0,\text{gas}} - v_{0,\text{fluid}}}. \quad (4.6)$$

The phase separation minimizes the free energy,

$$f(T, v) = c_{\text{fluid}}(v)f(T, v_{0,\text{fluid}}) + c_{\text{gas}}(v)f(T, v_{0,\text{gas}}) < f(T, v_{0,\text{fluid}}) - \int_{v_{c,\text{fluid}}}^v dv' P(T, v'), \quad (4.7)$$

see Fig. 4.1.

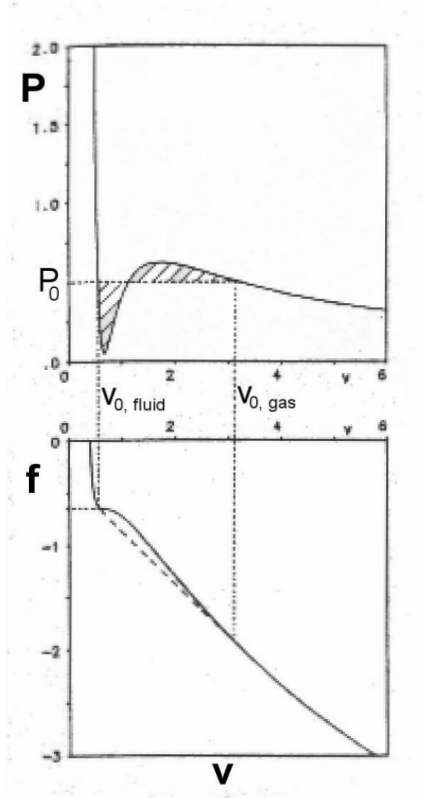


Figure 4.1: Illustration of the Maxwell construction at the example of the van der Waals gas. Upper panel: Pressure P (in units of P_c) as a function of $v = V/N$ (in units of v_c). The left part of the curve corresponds to a fluid, the right part to a gas. The first order transition takes place at $P = P_0$. For $v_{0,\text{fluid}} < v < v_{0,\text{gas}}$, the system is phase separated into a fluid with density $1/v_{0,\text{fluid}}$ and into a gas with density $1/v_{0,\text{gas}}$. While the part of the curve with positive slope is unphysical, the parts between $v_{0,\text{fluid}}$ and the minimum and between the maximum and $v_{0,\text{gas}}$ are thermodynamical unstable but realizable, corresponding to overheated fluid and undercooled gas, respectively. Lower panel: the free energy per particle $f = F/N$ (in units of $k_B T_c$) is minimized by the phase separation.

Differentiating $\mu_{\text{fluid}}(T, P_0) = \mu_{\text{gas}}(T, P_c)$ with respect to T and using $d\mu = -s dT + v dP$, one obtains the Clausius-Clapeyron Eq.,

$$\frac{dP_0(T)}{dT} = \frac{q}{T(v_{0,\text{fluid}} - v_{0,\text{gas}})}, \quad (4.8)$$

where $q = (s_{\text{fluid}} - s_{\text{gas}})T$. The equation relates the jump q in the entropy and the jump $v_{0,\text{fluid}} - v_{0,\text{gas}}$ in v to the slope of $P_0(T)$.

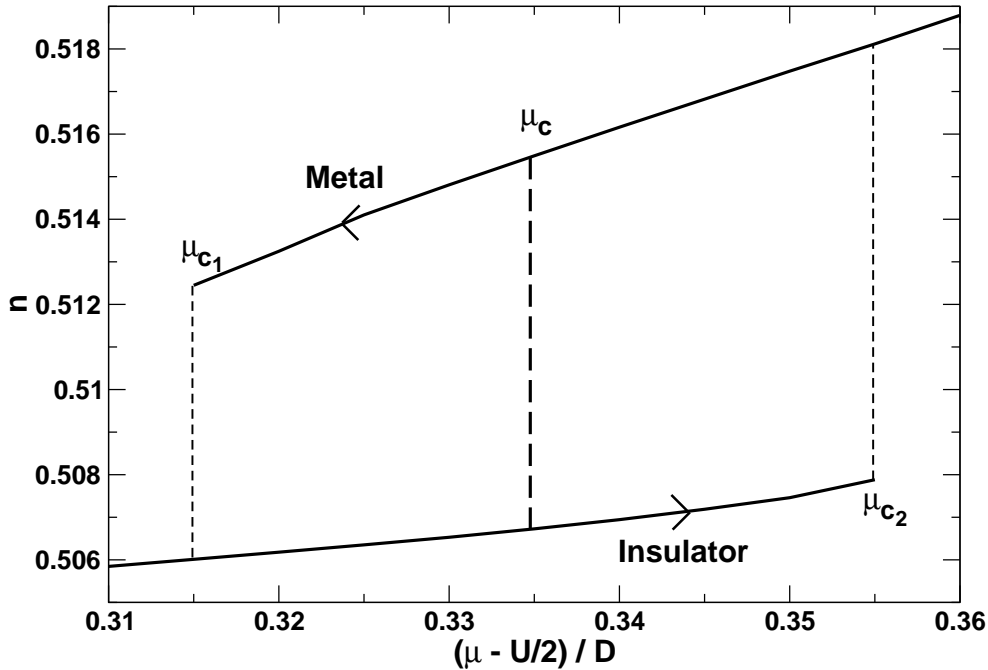


Figure 4.2: Hysteresis of the occupation n as a function of the chemical potential μ , calculated with DMFT/IPT at $T = 0.02D$ and $U = 2.5D > U_{c2}$ on a three-dimensional cubic lattice. Starting from an insulating DMFT solution and increasing the chemical potential, the system stays insulating until the critical potential μ_{c2} is reached, where the system jumps to a metallic solution with a different occupation. If one starts with the metallic solution and decreases μ , the system stays metallic until μ_{c1} is reached. The actual transition occurs at μ_c . The insulating solution for $\mu > \mu_c$ and the metallic solution for $\mu < \mu_c$ are thermodynamically unstable, corresponding to undercooled gas and overheated liquid, respectively.

4.1.2 Mott transition away from half filling

The results from the previous section are directly applicable to the Mott transition. One needs to identify the pressure P with the chemical potential μ and the volume v with the filling n . The graph corresponding to Fig. 4.1 is shown in Fig. 4.2.

In the context of DMFT, one can understand the jump of the occupation at the critical values of the chemical potential by the following argument. Suppose, for an interaction $U > U_{c2}$, one starts with the half-filled insulating solution and starts to increase the chemical potential. For $T > 0$, the gap of the local density of states $A(\omega) \equiv -(1/\pi)\text{Im}G_{\text{lat}}(\omega)$ is thermally activated and the occupation increases slightly. When μ reaches the upper Hubbard band, the local density of states at the chemical potential $A(\mu)$ strongly increases, leading to an increase of the hybridization function (2.9) at the chemical potential $\Delta(\mu)$ in the corresponding impurity model (this connection can directly be seen for the Bethe lattice where $\Delta(\omega) = t^2 G_{\text{lat}}(\omega)$ [10], but also holds for other lattices). The Kondo temperature

4.1.

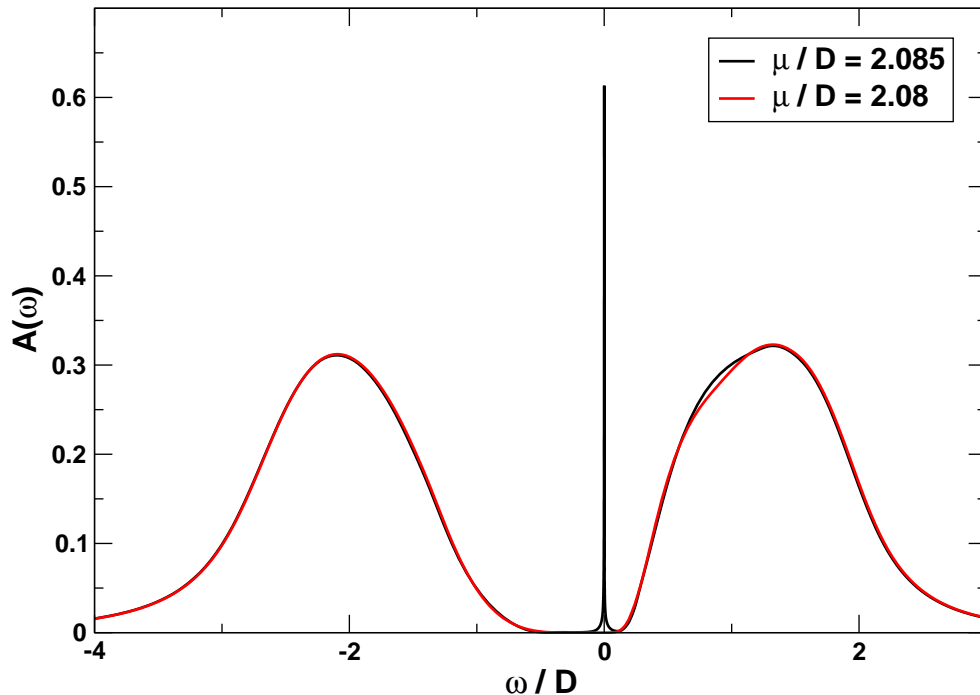


Figure 4.3: Local density of states $A(\omega) \equiv -(1/\pi)\text{Im}G_{\text{lat}}(\omega)$ calculated with DMFT/NRG for $T = 0$, $U = 3.4D$, and two different chemical potential μ close to the lower edge of the upper Hubbard band. For $\mu = 2.08D$ the system is still insulating and $A(\mu) = 0$. If μ is slightly increased, it reaches the upper Hubbard band and the system becomes metallic. Since T_K is arbitrarily small, the weight of the peak at the transition vanishes. To verify this numerically, one has to be careful to include enough shells in the NRG calculation to obtain the desired accuracy. Here 80 shells are used and the filling of the two solutions differs by less than 0.001.

$T_K \propto \Delta(\mu)$. Hence the Kondo resonance appears when the point $T_K = T$ at $\mu = \mu_{c_2}$ is reached. The Kondo peak, corresponding to the quasi-particle peak in the lattice Green's function, enhances itself through the self-consistency loop. Since its width is finite and given by T_K , the jump in the occupation is finite. For the same reason does the jump from the metallic to the insulating solution occur at a smaller chemical potential $\mu_{c_1} < \mu_{c_2}$. Through the self-consistency loop the Kondo peak sustains itself for $\mu > \mu_{c_1}$. The resulting loop represents a typical hysteresis effect of a first order phase transition. The actual transition occurs at an intermediate μ_c such that the free energy is minimized. The insulating solution for $\mu > \mu_c$ and the metallic solution for $\mu < \mu_c$ are thermodynamically unstable, corresponding to undercooled gas and overheated liquid, respectively. Let us shortly comment on what happens to the above argument at the second order endpoint at $T = 0, U = U_c$. At $T = 0$, there is no thermal activation of the gap in $A(\omega)$. Starting at half filling and increasing μ , $A(\mu)$ becomes finite when μ reaches the upper Hubbard band. This will immediately lead to a finite T_K and thus to a Kondo resonance in the

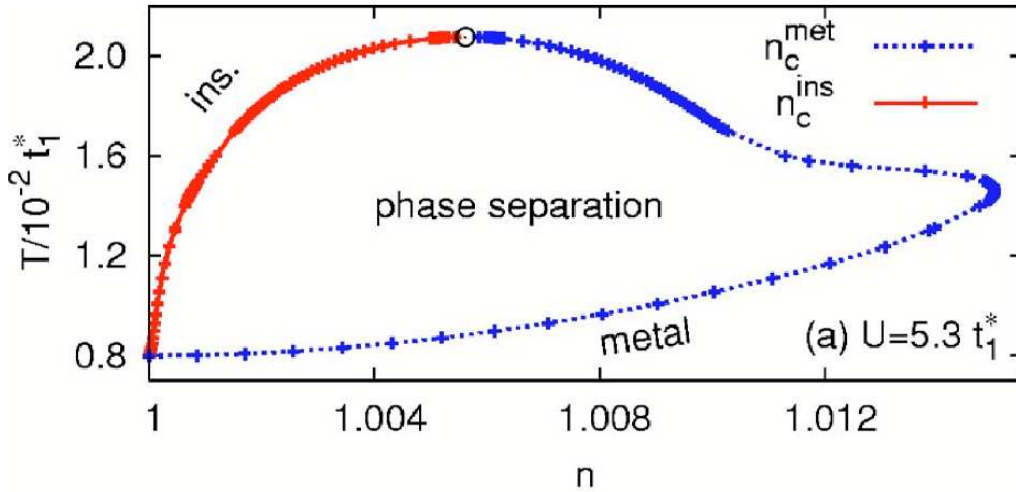


Figure 4.4: Phase diagram of the Mott transition at finite doping, determined by Eckstein et al. by the self-energy functional approximation method [20]. Here a Bethe lattice with only nearest neighbor hopping t_1^* has been considered, where the interaction $U = 5.3t_1^* > U_c$. For temperature $T > 0.810^{-2}t_1^*$, the system is insulating at half filling. For increasing n , a region of phase separation is entered, where the metallic phase and the insulating phase are separated according to the Maxwell construction. For large n , the system is metallic. Picture taken from [68].

impurity model, since $T = 0$. However, T_K and hence also the width of the resonance will be arbitrarily small and the occupation $n(\mu)$ will be continuous. This discussion is corroborated by DMFT/NRG results for $T = 0$ in Fig. 4.3.

In general, with the usual DMFT it is possible to find the hysteresis for a thermodynamic variable of the Mott transition. E.g., one can determine μ_{c_1} or μ_{c_2} for fixed U , T in the way described above. In general, one starts with a metallic (insulating) solution and varies one thermodynamic variable X while keeping the other fixed. The value of X where the metallic (insulating) solution jumps to the insulating (metallic) solution is identified as X_{c_2} (X_{c_1}). However, to obtain the actual critical value of X , where the thermodynamic phase transition occurs, is rather complicated. One needs to determine the thermodynamic potential $F(X)$ to find its minimum. There are several ways to compute $F(X)$ with the available quantities, i.e. the one-particle Green's functions and the self-energy, but they are all more or less afflicted with numerical inaccuracy. The self-energy functional approximation method (SFA) invented by Potthoff et al. is better applicable. As described in Section 2.3, in the SFA the solution to the lattice problem is found by directly minimizing the thermodynamic potential in the DMFT approximation. Thus it is well suited to evaluate the critical quantities of the transition. With the SFA, Eckstein et al. [68] were able to determine the phase diagram of the Mott transition at finite doping, see Fig. 4.4. Since the Bethe lattice with only nearest neighbor hopping is particle-hole symmetric, the phase diagram is symmetric with respect to the $n = 1$ axis. In Fig. 4.5, the phase diagram

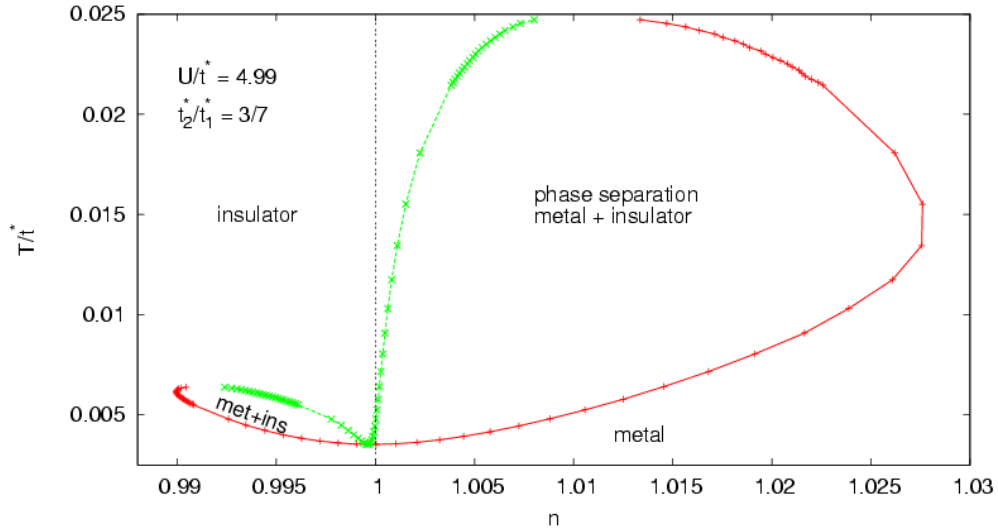


Figure 4.5: Phase diagram of the Mott transition at finite doping for broken particle-hole symmetry, determined by Eckstein et al. by the self-energy functional approximation method [20], cf. Fig. 4.4. Here particle-hole symmetry is broken by introducing a next-nearest neighbor hopping t_2^* . Hence the phase diagram is not symmetric with respect to the $n = 1$ axis. Picture taken from [68].

for the Bethe lattice is shown, where particle-hole symmetry is broken by introducing a next-nearest neighbor hopping. Note that the lowest stable point of the insulating phase (T_{\min}, n_{\min}) is shifted away from the $n = 1$ axis. Remarkably, the transition from metal to insulator occurs without phase separation at this point. The existence of such a point is guaranteed by the Clausius-Clapeyron Eq. (4.8), which in this case reads

$$\frac{d\mu_c(T)}{dT} = \frac{S_{\text{met}} - S_{\text{ins}}}{n_{\text{ins}} - n_{\text{met}}} \Big|_{T, \mu_c(T)}. \quad (4.9)$$

Since the insulator is destabilized by both electron and hole doping, generally a minimum of $\mu_c(T)$ exists, where $d\mu_c/dT = 0$, which corresponds to the point (T_{\min}, n_{\min}) in the (n, T) phase diagram.

4.2 Microphase separation

In this section we study the phase separated region of the Mott transition at finite doping, see Fig. 4.4, using the inhomogeneous DMFT. Since the metallic and the insulating phases have different filling, a macroscopic separation of phases is precluded by the Coulomb force, which leaves the possibility of two different scenarios. On the one hand, the system can pass through a direct first order transition between the two competing uniform phases. On the other hand it can form a mixture of microdomains on the order of only a few

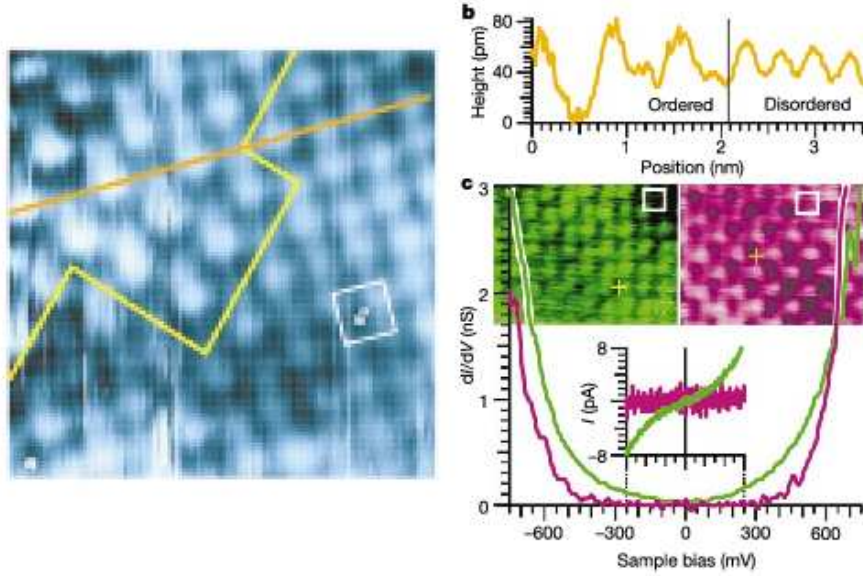


Figure 4.6: Tunneling microscope measurements of the paramagnetic phase of $Bi_{0.24}Ca_{0.76}MnO_3$ at $299K$. The experiments show a microphase separation of metallic and insulating domains (left panel) with different dI/dV characteristics (right panel). Picture taken from [70].

lattice constants. Jamei et al. find a critical value of the Coulomb force above which no microphase separation occurs [69]. The possibility of a microphase separation scenario is supported by tunneling microscope measurements of transition-metal perovskite oxides [70], see Fig. 4.6. Hence let us consider a system with a Coulomb interaction below the critical value. This still leaves the question of what shape the microdomains have. Lorenzana studied the phase separation of two phases with different filling and a uniform background charge. They investigated two different possible shapes: a layer geometry and a spherical drop geometry [71]. They find that only for very similar fractions of metal and insulator, $c_{\text{metal}} \approx c_{\text{ins}} \approx 1/2$, cf. Eq. 4.7, the layer geometry is energetically favorable. To study the domains with the inhomogeneous DMFT, we choose the layer set up described in Section 3.1. However, we have no intention to focus only on the layer geometry. We rather intend to obtain an estimate of the cost to form a domain wall. This cost, in competition with the Coulomb force, will determine the size of the domains.

Before turning to the results, let us first comment on the question if the inhomogeneous DMFT is appropriate to study the issue of phase separation and domain walls. Since the DMFT becomes exact in the limit of infinite dimensions, one could be tempted to think that a domain wall between two different phases cannot be treated within this approximation. Let us consider a hypercubic lattice, as shown in Fig. 4.7 (a), where a domain wall separates a red phase on the left and a green phase on the right. A site in the domain wall is connected to $2(d-1)$ sites parallel to the domain wall and only 2 sites perpendicular to the domain wall. Considering the bath of the site in a DMFT calculation, one could

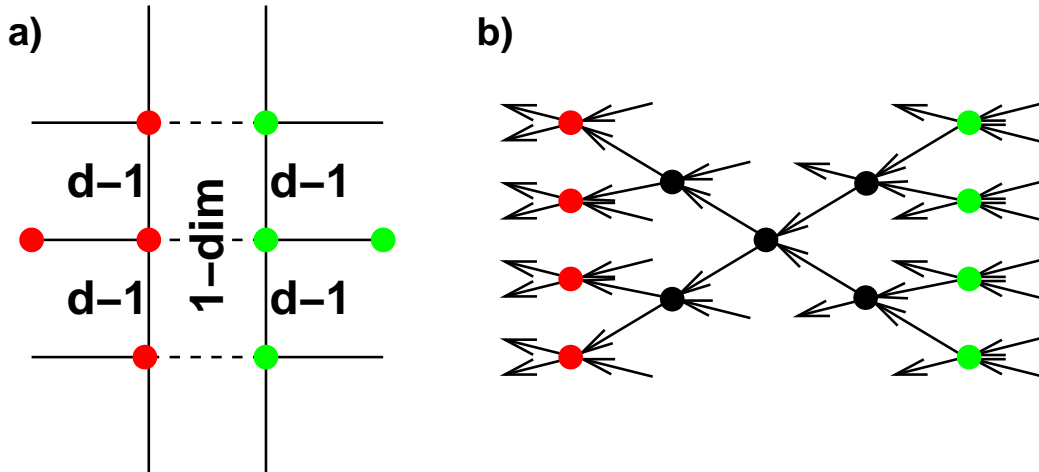


Figure 4.7: (a) For a hypercubic lattice, a site at a domain wall between two phases (red and green) has $2(d - 1)$ neighbors parallel to the domain wall and only two neighbors perpendicular to the domain wall. Hence the neighbors perpendicular to the wall play no role in the limit $d \rightarrow \infty$. (b) A Bethe lattice with connectivity $z = 4$ is depicted. Every site has two “incoming” and two “outgoing” connections, defining a distance (the distance between the red and the green phase is four). For this case the domain wall survives the limit of infinite dimensions $z \rightarrow \infty$.

certainly neglect the dimensions perpendicular to the domain wall in the limit $d \rightarrow \infty$ and an extended domain wall could not exist. However, one can also consider a different $d \rightarrow \infty$ limit, as shown in Fig. 4.7 (b). There a Bethe lattice with connectivity $z = 4$ is shown. Regarding a Bethe lattice with even connectivity z , one can define that a site has $z/2$ “incoming” connections and $z/2$ “outgoing” connections. In this sense a distance can be defined. E.g., in the figure the red and the green phase are separated by a distance of four connections. Taking the limit of infinite dimensions $z \rightarrow \infty$, one obtains a reasonable extended domain wall structure.

As a first test of the method let us investigate a half-filled system consisting out of 100 layers. In the particle-hole-symmetric half-filled case, no phase separation occurs. We will create a domain wall artificially by fixing the boundary conditions. We fix the self-energies of the first 10 and the last 10 layers in the following way. With DMFT/IPT, we compute the solution of the bulk problem for the temperature $T = 0.015D$ and two different values of interaction, $U_1 = 2.28D$ and $U_2 = 2.48D$, where both values are in the coexistence regime, $U_{c_1} < U_1 < U_2 < U_{c_2}$. We both determine the insulating and the metallic solution. The self-energy of the metallic solution is used to fix the first 10 layers, whereas the self-energy of the insulating solution is used to fix the last ten layers. The solution for the 80 middle layers is then found by using the inhomogeneous DMFT/IPT for the layer structure. The results are shown in Fig. 4.8, where the local density of states at the chemical potential $A(\omega = 0)$ is plotted for each layer to differentiate between the metal and the insulator. As already mentioned, with the usual DMFT method it is rather

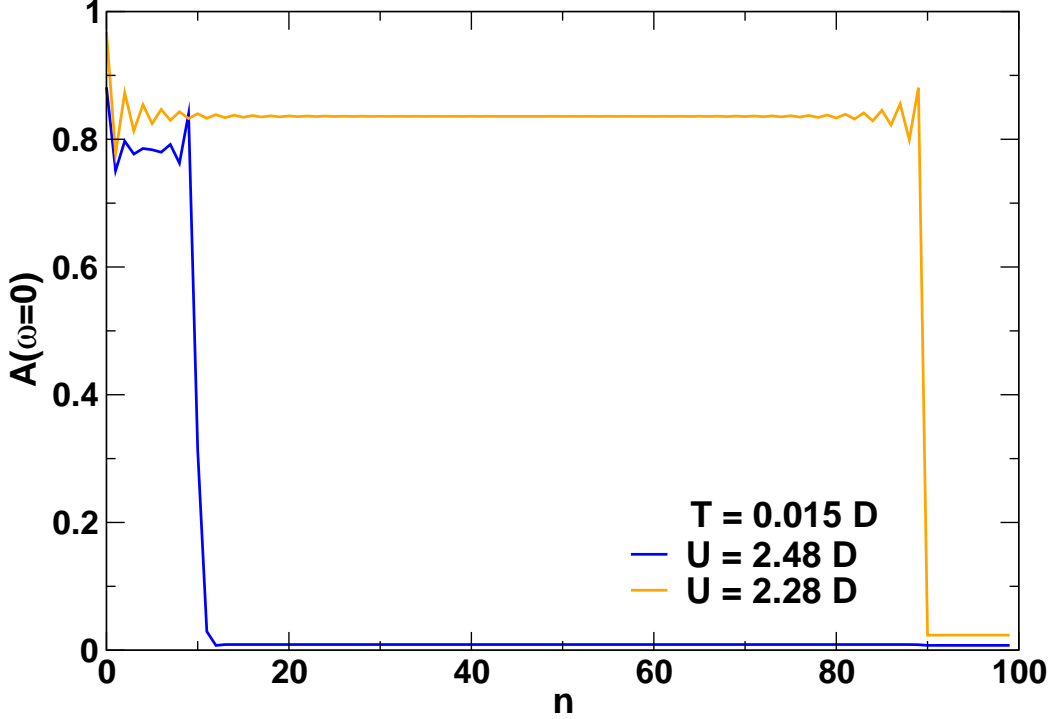


Figure 4.8: Local spectral function at the chemical potential $A(\omega = 0)$ as a function of layer n for a system of 100 layers calculated with the inhomogeneous DMFT/IPT. Two curves at temperature $T = 0.015D$ and different values of interaction U are depicted. The self-energies of the first and the last ten layers are kept fixed in the calculation. For a discussion see text.

complicated to determine the value of U_c . Yet, obviously, $U_1 < U_c < U_2$, since, for U_1 , the metallic phase eliminates the insulating phase, whereas for U_2 , the insulating phase eliminates the metallic phase. For $U = 2.48D$, the layers 9 to 12 represent a domain wall between the metallic and the insulating phase. As shown in Fig. 4.9, the transition is not abrupt but the wall has an internal structure. The spectral functions (left panel) of layer 10 and 11 are very dissimilar to both the metallic and the insulating solution found for the bulk system, which resemble the spectral functions of layer 9 and 12, respectively. Recalling the definition of the quasi-particle weight,

$$Z = \left(1 - \frac{\partial \text{Re}\Sigma(\omega)}{\partial \omega} \Big|_{\omega=0} \right)^{-1}, \quad (4.10)$$

the real part of the self-energy (right panel) also illustrates that both layer 10 and 11 have intermediate values of Z .

To study the phase separation, we will choose the following set up. For a temperature T and an interaction U , we determine the n vs. μ hysteresis. Then we do an inhomogeneous DMFT calculation at fixed occupation \bar{n} , such that \bar{n} lies in the gap. Since we are away from half-filling, particle-hole symmetry is broken. The numerical solution spontaneously

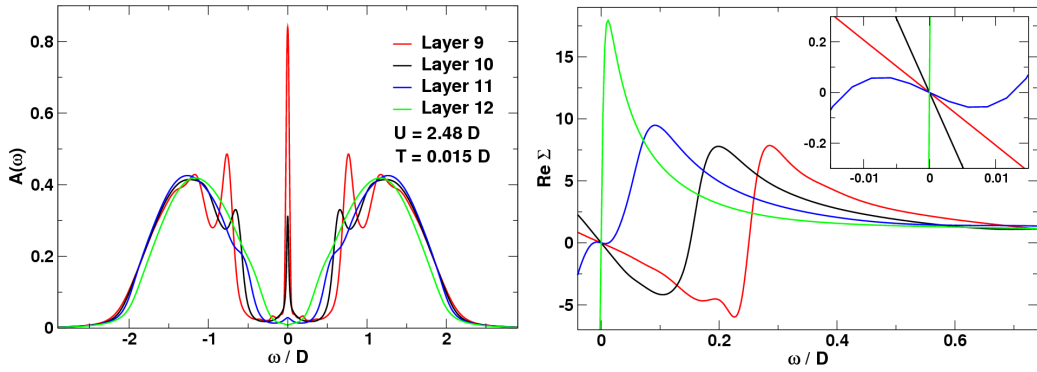


Figure 4.9: Spectral functions $A(\omega)$ (left panel) and real part of the self-energy $\text{Re}\Sigma(\omega)$ (right panel) for the layers 9, 10, 11 and 12 of the system depicted in Fig. 4.8 ($T = 0.015D$ and $U = 2.48D$). For a discussion see text.

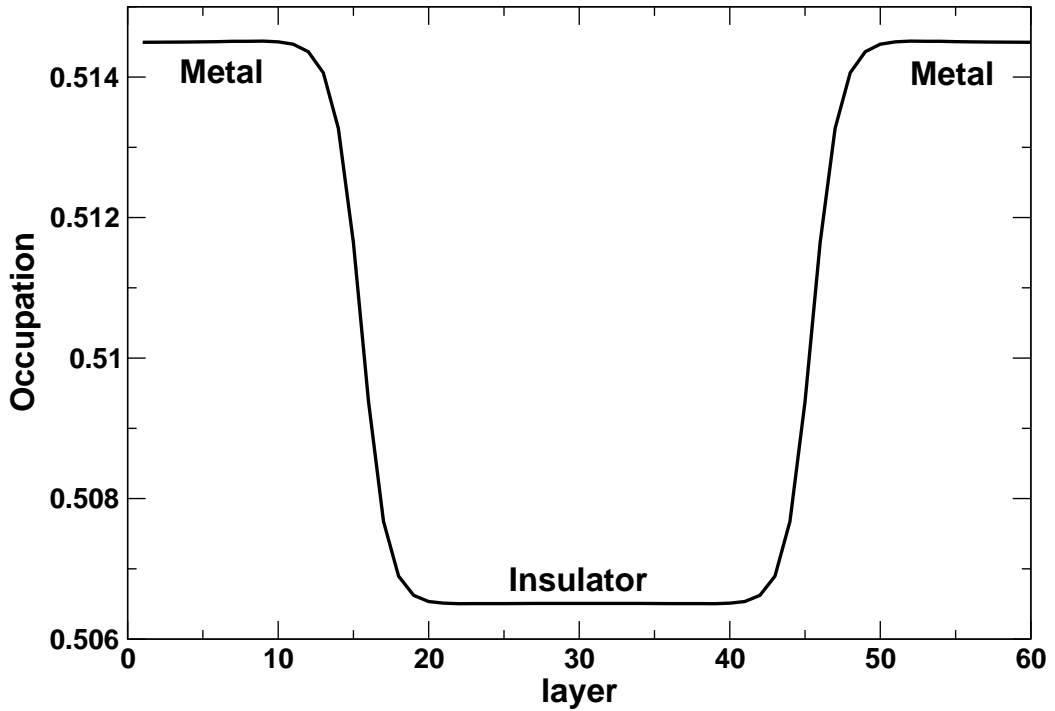


Figure 4.10: Occupation as a function of layer number for a system of 60 layers for $T = 0.02D$, $U = 2.5D$ and a fixed average occupation per layer $\bar{n} = 0.5105$. The calculation was done using periodic boundary conditions. The system separates into a metallic region with filling $n \approx 0.5142$ and an insulating region with filling $n \approx 0.5063$.

separates into a metallic and a insulating region, see Fig. 4.10. In analogy to the artificial domain wall, the two depicted domain walls extend over a few layers, where the local spectral functions of the intermediate layers are very dissimilar from the bulk solutions.

Let us turn on the Coulomb force. The Coulomb Hamiltonian in second quantization has the form

$$\mathcal{H}_{\text{Coulomb}} = \frac{1}{2} \int d^3r d^3r' V(\mathbf{r}, \mathbf{r}') \psi^\dagger(\mathbf{r}) \psi^\dagger(\mathbf{r}') \psi(\mathbf{r}') \psi(\mathbf{r}), \quad (4.11)$$

where $\psi^\dagger(\mathbf{r})$ creates an electron at \mathbf{r} and $V(\mathbf{r}, \mathbf{r}') = \frac{4\pi e^2}{|\mathbf{r}-\mathbf{r}'|}$. We will treat it in a Hartree approximation,

$$\begin{aligned} \mathcal{H}_{\text{Coulomb}} &\rightarrow \int d^3r d^3r' V(\mathbf{r}, \mathbf{r}') \psi^\dagger(\mathbf{r}) \psi(\mathbf{r}) \langle \psi^\dagger(\mathbf{r}') \psi(\mathbf{r}') \rangle \\ &= \int d^3r n(\mathbf{r}) \phi(\mathbf{r}), \end{aligned} \quad (4.12)$$

where $n(\mathbf{r}) = \psi^\dagger(\mathbf{r}) \psi(\mathbf{r})$ is the charge density and we have introduced the electrostatic potential $\phi(\mathbf{r}) \equiv \int d^3r' V(\mathbf{r}, \mathbf{r}') \langle n(\mathbf{r}') \rangle$. We can absorb ϕ into an electrochemical potential $\mu_{\text{elec}}(\mathbf{r}) = \mu + \phi(\mathbf{r})$.

In the case of the layer geometry, one layer, extended along the x - and y - direction and located at $z = 0$, has the electric field $\mathbf{E} = 4\pi q_A \mathbf{e}_z \text{sgn}(z)$, according to Gauss' theorem, where q_A is the charge per area. Hence the electrostatic potential of a layer located at z_i is $\phi(z) = -4\pi |z - z_i| q_A$. Thus the total electric potential reads

$$\phi(z) = -4\pi\alpha \sum_i q_i |z - z_i|, \quad (4.13)$$

where q_i is the charge per area of the layer at $z = z_i$ and a constant α was introduced to vary the strength of the Coulomb force. This can be motivated, e.g., by including screening effects in the material, which can crudely be captured by such a constant. If one defines the lattice constant of the cubic two-dimensional layer to be 1, $q_i = n_i - \bar{n}$, where $n_i = \int d\omega A_i(\omega) f(\omega, \mu, T)$ and \bar{n} is the background charge. Here $f(\omega, \mu, T)$ is the Fermi function and $A_i(\omega)$ is the spectral function of layer z_i . In order for the algorithm to converge, it is important to fix the total occupation $n = \sum_i n_i$ to be equal to the occupation $\sum_i \bar{n}$ of the background charge in each cycle of the self-consistency loop. Here it is necessary to repeat the step one of the self-consistency loop (2.18), $\{\Sigma_i\} \rightarrow \hat{G}_{\text{lat}}$, until $\sum_i n_i = \sum_i \bar{n}$ by adjusting the chemical potential μ . The results for a system with 60 layers with periodic boundary conditions for two different values of α are shown in Fig. 4.11. For a small strength of the Coulomb force, $\alpha = 0.006$, the results agree with the ones shown in Fig. 4.10. The system separates into a metallic and insulating region with different fillings. If the strenght of the Coulomb force is increased to $\alpha = 0.02$, two new domain walls appear (note that the periodic boundary conditions were not implemented for the Coulomb force). The size of the domains are determined by the competition of the Coulomb force and the cost of building up new domain walls. Due to the periodic boundary conditions, only integer numbers of domains will appear. To really estimate the cost of a

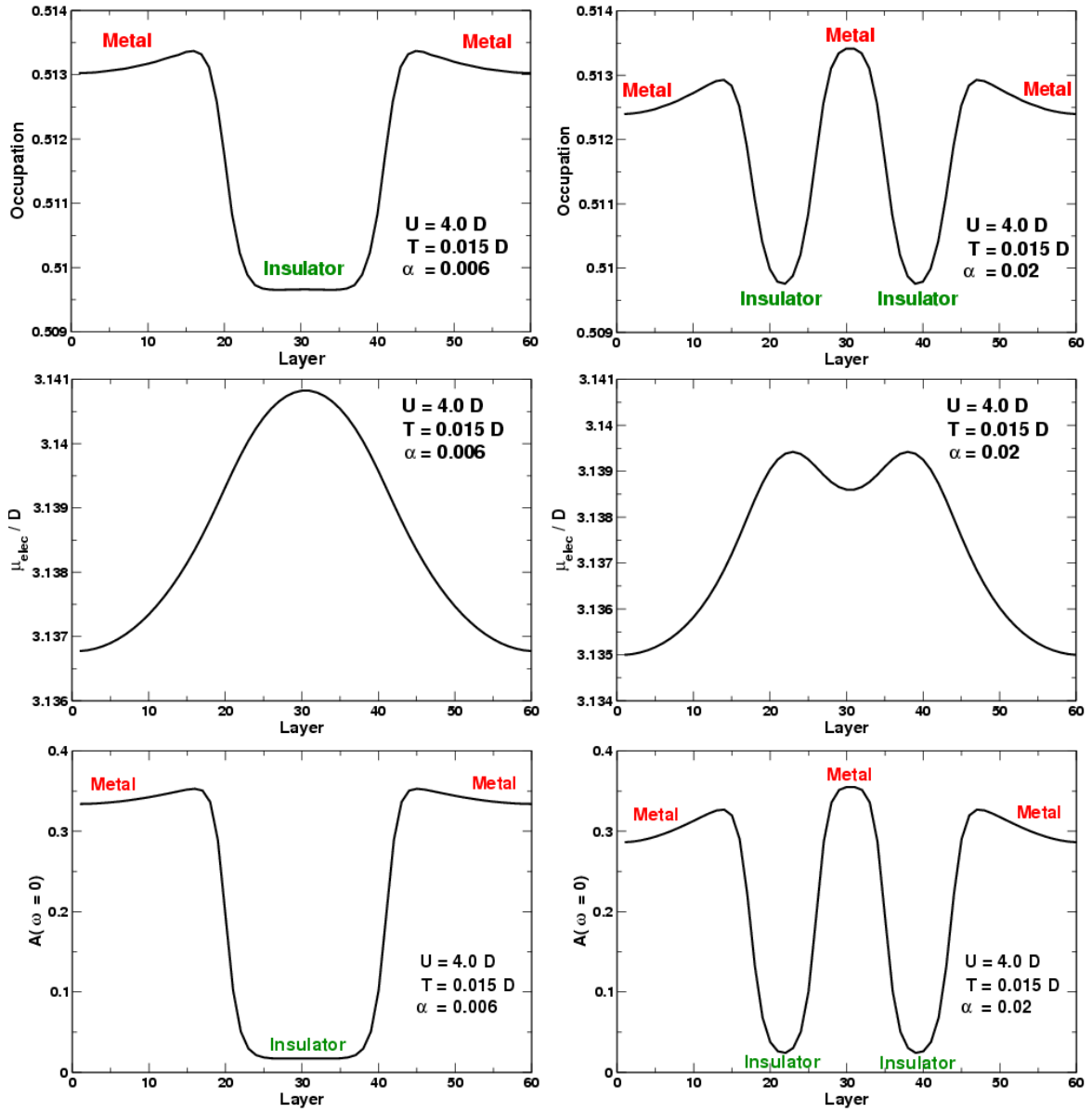


Figure 4.11: Domain structure for a system consisting out of 60 layers at $U = 4.0D$ and $T = 0.0015D$ for two different values of α , cf. Eq. (4.13), $\alpha = 0.006$ (left panels) and $\alpha = 0.02$ (right panels). Top panels: occupation as a function of layer position. Middle panels: electrochemical potential as a function of layer position. Bottom panels: height of the spectral function at the chemical potential. The curves are produced with DMFT/IPT. For a discussion see text.

domain wall, it would be necessary to compute the free energy per layer for systems with different numbers of layers, which is difficult with DMFT/IPT.

Chapter 5

Metal-Insulator Transition in Optical Lattices

5.1 Experimental Background: Optical Lattices

As mentioned in chapter 2.1, it is very difficult to make theoretical predictions for the Hubbard model (2.6) for a arbitrary choice of parameters. One has to make further assumptions or simplifications to make further progress. E.g., one has to neglect off-diagonal entries of the self-energy in DMFT in order to describe the Mott metal-insulator transition (MMIT). However, regarding compounds which exhibit strongly correlated physics such as the MMIT, the Hubbard model (2.6) is still an oversimplification of the real experimental situation. In these materials, the presence of other bands (two-band Hubbard model, etc., see e.g. [72]), distortions of the lattice (e.g. Peierls transition, etc.), interaction induced next-nearest neighbor hopping and many other effects play an important role. Thus, these materials cannot be used to rigorously test theoretical predictions for the simple one-band Hubbard model (2.6). Therefore, condensed-matter theorists joyfully follow the remarkable progress in the field of cold atom physics. With fermionic atoms in optical lattices, it seems not only possible to build an experimental system exactly described by the Hubbard model (2.6), but one also has full control to most of the important parameters. In this section, we will give a short overview of the exciting world of cold atom systems.

The rapid progress in the field of cold atoms was boosted by the first realization of a Bose-Einstein condensate, which was rewarded with a Nobel-prize for Eric A. Cornell, Wolfgang Ketterle and Carl E. Wieman [73, 74]. For our purposes, we need fermionic instead of bosonic atoms. Fermionic atoms are much more difficult to cool down since the equilibration time is very long. This is caused by the lack of collisions of fermions due to the Pauli principle. Thus, the experimental progress in experiments with cold fermions is always a step behind compared to experiments with cold bosons. Since a fermion must have odd spin, neutral atoms consisting of the same number of electrons and protons must have an odd number of neutrons. Candidates frequently used in experiments are ^6Li and ^{40}K [75]. The atoms are elaborately cooled down using methods such as laser cooling or

evaporative cooling and finally trapped in a magnetic trap with a harmonic potential [75]. In addition to the harmonic potential, one can create an optical lattice with standing laser waves [75].

If an atom is exposed to laser light, the atom absorbs and emits photons which causes virtual excitations of the atomic ground state. Therefore the ground state energy of the atom will be shifted. A simple estimate for the shifts, referred to as "ac Stark shifts", can be given by second order perturbation theory [75],

$$V_g = \frac{\hbar\Omega_R^2\delta}{\delta^2 + \Gamma_e^2/4}. \quad (5.1)$$

Here $\delta = \omega - \omega_{eg}$ is called the "detuning" of the laser frequency ω with respect to the transition frequency ω_{eg} defined by $\hbar\omega_{eg} = E_e - E_g$, where E_g and E_e are the energies of the atomic ground state and excited state, respectively. The "Rabi frequency" Ω_R is given by the matrix element $\Omega_R = |\langle e|\vec{d}\cdot\vec{\mathcal{E}}_\omega|g\rangle|/\hbar$ of the perturbing part of the Hamiltonian, $\mathcal{H}_{\text{pert}} \propto \vec{d}\cdot\vec{\mathcal{E}}_\omega$, between the ground state $|g\rangle$ and the excited state $|e\rangle$, where \vec{d} is the dipole operator and $\vec{\mathcal{E}}_\omega$ is the amplitude of the laser field. Finally, Γ_e is the inverse lifetime of the excited state. One can create a time-independent, spatially varying amplitude $\mathcal{E}_\omega(\vec{x})$ with counter-propagating laser fields. The ground state energy shift of the atom can be viewed as an effective potential for the atom with a depth V_g . With a three-dimensional set-up of many counter-propagating laser waves, a 3D cubic lattice can be created. The hopping matrix element between two neighboring sites, termed t in the Hubbard model (2.6), can be varied by changing the depth of the lattice V_g , which is directly proportional to the laser field intensity. Yet not only the hopping can be tuned, but also the on-site repulsion U in (2.6). The magic word is Feshbach resonance.

Since atoms have an internal structure, inelastic scattering between two atoms can take place which will change the internal states of the atoms. If the two atoms are initially in the states $|\alpha\rangle$ and $|\beta\rangle$, they can be scattered into the states $|\alpha'\rangle$ and $|\beta'\rangle$, respectively. Energy conservation leads to,

$$E = \epsilon_\alpha + \epsilon_\beta + \frac{\hbar^2 k_{\alpha,\beta}^2}{2m_r} = \epsilon_{\alpha'} + \epsilon_{\beta'} + \frac{\hbar^2 k_{\alpha',\beta'}^2}{2m_r}, \quad (5.2)$$

where E is the total available energy, ϵ_α is the energy of the state $|\alpha\rangle$ of an atom, $k_{\alpha,\beta}$ is the relative momentum and $\hbar^2 k_{\alpha,\beta}^2/2m_r$ is the kinetic energy of the relative motion of the two atoms. The scattering from an initial state into a certain final state, $\alpha\beta \rightarrow \alpha'\beta'$, is called 'channel'. A channel $\alpha\beta \rightarrow \alpha'\beta'$ is termed 'closed' if $\hbar^2 k_{\alpha',\beta'}^2/2m_r = \epsilon_\alpha + \epsilon_\beta + \hbar^2 k_{\alpha,\beta}^2/2m_r - \epsilon_{\alpha'} - \epsilon_{\beta'} \leq 0$. The threshold energy for scattering into this channel is $E_{\text{th}}(\alpha'\beta') = \epsilon_{\alpha'} + \epsilon_{\beta'}$. Scattering in an 'open' channel can be significantly altered if the total available energy E is close to a bound state of a closed channel, see Fig. 5.1. Since different internal states of the atoms correspond to different hyperfine states, the energy difference between the threshold energy E_{th} of an open channel and the energy of a bound state E_{res} can be changed by applying a magnetic field,

$$E_{\text{th}} - E_{\text{res}} \approx (\mu_{\text{res}} - \mu_\alpha - \mu_\beta)(B - B_0), \quad (5.3)$$

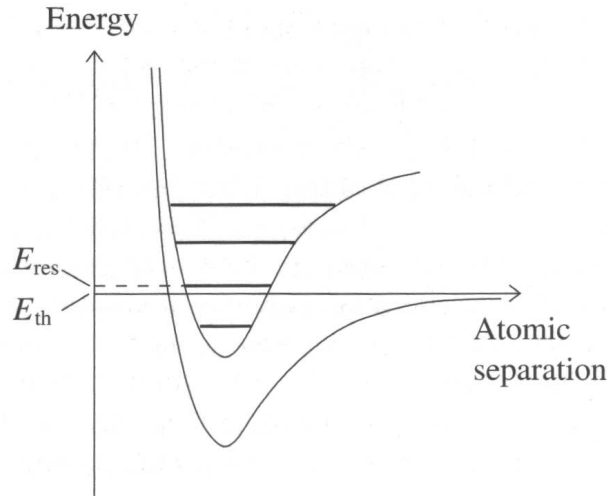


Figure 5.1: Feshbach resonance: the potential energy curves for two different channels are shown, where E_{th} is the threshold energy of the lower channel. If the total available energy is close to the energy E_{res} of a bound state in the upper channel, the upper channel will be closed while the lower channel will be open. However, scattering in the lower channel will be significantly altered by the presence of the bound state in the upper channel. Picture taken from Ref. [75].

where μ_α, μ_β and μ_{res} are the magnetic moments of the atomic states $|\alpha\rangle, |\beta\rangle$ and of the bound state, respectively, and B_0 is the magnetic field strength where the bound state is on resonance. If a_{nr} is the scattering length of an open channel not influenced by a closed channel, the scattering length a can be changed by the presence of the closed channel according to [75]

$$a = a_{\text{nr}} \left(\frac{\Delta B}{B - B_0} \right), \quad (5.4)$$

where

$$\Delta B = \frac{m}{4\pi\hbar^2 a_{\text{nr}}} \frac{|\langle \psi_{\text{res}} | \mathcal{H}_{QP} | \psi_0 \rangle|^2}{(\mu_{\text{res}} - \mu_\alpha - \mu_\beta)}. \quad (5.5)$$

Here, $|\psi_{\text{res}}\rangle$ is the bound state, $|\psi_0\rangle = |\alpha\rangle|\beta\rangle$ and $\mathcal{H}_{PQ} = P\mathcal{H}_{\text{hf}}Q$, where Q and P are the projectors to the space of the open and closed channel, respectively, and \mathcal{H}_{hf} is the atomic hyperfine Hamiltonian. Thus, with the help of a magnetic field, the Coulomb repulsion U of the atoms in the open channel (which is directly related to the scattering length) can not only be tuned to desired values, but also be made attractive or repulsive.

Light absorption measurements are used frequently to probe atoms in an optical trap. The 'column density' $n_z(x, y) = \int dz n(\vec{r})$ of the atomic cloud, i.e. the density $n(\vec{r})$ integrated along the z -axes, can be measured by shining laser light on the probe along the z -direction and measuring the absorption. Also time-of-flight experiments are very popular to directly measure the projected momentum distribution $n_{\vec{k}}^{\text{tof}} = \int dk_z n_{\vec{k}}/2\pi$ [76, 77],

where

$$n_{\vec{k}} = -\frac{1}{N} \sum_{i,j} \int \frac{d\omega}{\pi} f(\omega) e^{i\vec{k}(\vec{r}_i - \vec{r}_j)} \text{Im}G_{ij}(\omega). \quad (5.6)$$

In the measurement, the harmonic and the lattice potential are switched off. The atoms can now propagate with the velocity $\vec{v} = \vec{k}/m$. After a time Δt the absorption of the expanding cloud is measured, which directly gives $n(x, y) = \int dz n(\vec{r}) \propto \int dk_z n(\Delta t \vec{k}/m) \propto \int dk_z n(\vec{k})$.

Despite the rapid progress in the last decades, the Mott metal-insulator transition has not been observed in fermionic cold atoms experiments yet. The experimental challenge for this experiment is quite high, since, in addition to the problems with fermions mentioned above, one needs two different species of fermionic atoms to model the spin $S = 1/2$. However, recent progress gives hope that the Mott transition will be observed soon. For example, the Fermi-surface of atoms in an optical lattice was observed lately [78]. Also, experiments studying the BEC-BCS crossover, which use two different species of fermionic atoms in an optical lattice, have successfully been conducted [79, 80]. For bosonic atoms, the Mott-transition has already been observed in 2002 [76].

5.2 Group Theory of the Cubic Lattice

Since the fermionic atoms in an optical lattice are confined by a harmonic potential, the system is inhomogeneous. The value of the chemical potential μ_0 is absorbed into the external potential $\mu(r) = \mu_0 - V(r)$ including the harmonic potential $V(r)$ for a site in the optical lattice at distance r from the origin. In principle, we can directly apply the DMFT method for inhomogeneous Hubbard models introduced in Chapter 2 to study the Mott transition of fermionic atoms in an optical lattice. However, despite the inhomogeneous harmonic potential, there is still a high redundancy left, namely the symmetry group of the cubic lattice. In this section we will give an overview how group theory can be used to highly reduce the numerical effort.

To implement the inhomogeneous DMFT method for the optical trap, we have to follow the self-consistency loop Eq. (2.18), c.f. Fig. 2.6. We start with a set of self-energies $\{\Sigma_i\}$ for all sites of the lattice. We can now compute the lattice Green's function $G_{\text{lat}}(i, j, \omega)$ according to Eq. (2.20) and a set of bath functions $\mathcal{G}_{0,i}$ using Equation (2.21). Solving the Anderson model for each site i , defined by $\mathcal{G}_{0,i}$, we arrive at a new set of self-energies. Realistic optical lattice systems host several thousand atoms, which would imply that it is necessary to solve several thousand Anderson impurity models. But in fact, many sites are related by symmetry and are therefore equivalent. Since the symmetry group of the cubic lattice contains 48 symmetry operations, it is sufficient to describe only the one 48th part of the lattice. This wedge can then be used to construct the whole lattice by the symmetry operations. This reduces the number of impurity problems by roughly a factor of 48 (the factor will be less since lattice sites on symmetry surfaces can belong to two or more wedges). However, group theory can not only help us to identify equivalent sites, but also help us to change to a basis where the lattice Green's function will be block

diagonal, which will highly reduce the amount of time needed to invert the matrix. Each block corresponds to a irreducible representation R_r of the symmetry group. Since several blocks can belong to the same R_r , the blocks can be labeled by two numbers (r, m) , where r is the number of the irreducible representation R_r and m labels the blocks belonging to this R_r . If there are $n_{\text{inequivalent}}$ sites in the wedge, the block (r, m) will have the size

$$\dim \text{Block}_{(r,m)} = n_{\text{inequivalent}} \dim(R_r) \quad (5.7)$$

where $\dim(R_i)$ is the dimension of the irreducible representation R_i . For educational purposes, we will first show how one can use group theory for a 1D cubic lattice in a harmonic potential, which is just a 1D array of points with mirror symmetry. We will then demonstrate how one can implement the inhomogeneous DMFT method for a 2D cubic lattice. The symmetry group for the 2D cubic lattice is not abelian (e.g., rotating the vector $\vec{r} = (x = 1, y = 0)$ first by 90 degrees and then reflecting it at the y -axis gives a different result as first reflecting it at the y -axis, which has no effect, and then rotating it), and is thus very similar to the symmetry group of the 3D cubic lattice used in the remaining sections of this chapter. Since the similarity and the more cumbersome notation for the 3D lattice, we will just focus on the 2D cubic lattice.

For a one dimensional system with mirror symmetry, we have only two "wedges". Let us start with only one site per wedge, i.e. a two-site system. For this system, our lattice Green's function would have the form

$$G_{\text{lat}}^{-1}(\omega) = \begin{pmatrix} \omega + \mu & t \\ t & \omega + \mu \end{pmatrix}, \quad (5.8)$$

Of course the use of group symmetry is an overkill in this simple situation, but let us derive the unitary matrix, which encodes the change of basis to "block diagonal" form, for educational reasons with the help of the 1D mirror symmetry group G_{1D} . The symmetry group has only two elements, $\dim(G_{1D}) = 2$, the unit element g_1 and the mirror element g_2 . Since G_{1D} is abelian, there must be two one-dimensional irreducible representations $R_{r=1}$ and $R_{r=2}$, namely $R_1(g_1) = R_1(g_2) = 1$ and $R_2(g_1) = 1, R_2(g_2) = -1$. Not surprisingly, according to equation (5.7) the blocks in the "block diagonal" form will have dimension one. In the regular representation g_1 and g_2 are represented by the matrices

$$R_{\text{reg}}(g_1) = \begin{pmatrix} 1 & 0 \\ 0 & 1 \end{pmatrix}, R_{\text{reg}}(g_2) = \begin{pmatrix} 0 & 1 \\ 1 & 0 \end{pmatrix}. \quad (5.9)$$

The unitary matrix is given by the two eigenvectors \hat{u}_1 and \hat{u}_2 ,

$$U = \begin{pmatrix} \hat{u}_1 \\ \hat{u}_2 \end{pmatrix}, \quad (5.10)$$

where \hat{u}_r are normalized vectors, $\hat{u}_r = \vec{u}_r / (\vec{u}_r \cdot \vec{u}_r)$, with

$$\vec{u}_r = \frac{\dim(R_r)}{\dim(G_{1D})} \sum_{i=1}^{\dim(G_{1D})} R_r(g_i) R_{\text{reg}}(g_i) \vec{e}_1, \quad (5.11)$$

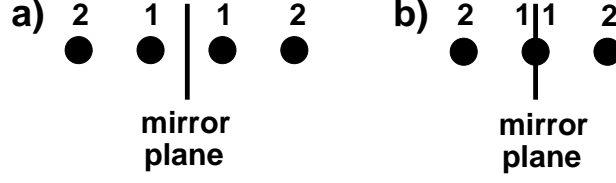


Figure 5.2: The one-dimensional cubic lattice in a harmonic potential is simply a string of sites with a mirror symmetry. a) Four-site system with two sites per wedge. b) Three-site system with a site on the mirror-plane, which is split up in two fictitious sites, one belonging to each wedge.

and $\vec{e}_1 = (1, 0)$. Indeed, this reproduces the well-known symmetric and anti-symmetric eigenvector $\vec{u}_{\text{sym}} = \frac{1}{\sqrt{2}}(1, 1)$ and $\vec{u}_{\text{assym}} = \frac{1}{\sqrt{2}}(1, -1)$, respectively, which are the basis for the diagonal form,

$$G_{\text{lat}}^{-1}(\omega) = \begin{pmatrix} \omega + \mu + t & 0 \\ 0 & \omega + \mu - t \end{pmatrix} = \left(\frac{1}{\sqrt{2}} \right)^2 \begin{pmatrix} 1 & 1 \\ 1 & -1 \end{pmatrix} \begin{pmatrix} \omega + \mu & t \\ t & \omega + \mu \end{pmatrix} \begin{pmatrix} 1 & 1 \\ 1 & -1 \end{pmatrix}, \quad (5.12)$$

where the new basis is (r, m) , i.e. the "blocks" can be labeled by $(1, 1)$ and $(2, 1)$. The reasoning behind equation (5.11) will become more obvious in the two-dimensional case, see below.

If there are several sites $n_{\text{inequivalent}}$ in one wedge, all sites in the lattice can be labeled by (w_i, p_i) , where w_i is the wedge number and p_i is the site number in the wedge. In real space, the coordinates of the Green's function can then be written as $G_{\text{lat}}^{-1}(\omega)((w_1, p_1), (w_2, p_2))$. According to (5.7), in the case of the one-dimensional system, the two blocks in the block-diagonal form will have the dimension $n_{\text{inequivalent}}$. All entries in the lattice Green's function matrix can then be labeled by (r, p_1, p_2) , where again $r = 1, 2$ labels the irreducible representation and p_1, p_2 are the coordinates in the block, with $1 \leq p_1, p_2 \leq n_{\text{inequivalent}}$. The unitary transformation takes the following form

$$G_{\text{lat}}^{-1}(\omega)(r, p_1, p_2) = \sum_{i_1=1}^{\dim(G_{1D})} \sum_{i_2=1}^{\dim(G_{1D})} (\hat{u}_r)_{i_1} G_{\text{lat}}^{-1}(\omega)((w_{i_1}, p_1), (w_{i_2}, p_2)) (\hat{u}_r)_{i_2}. \quad (5.13)$$

As an example let us consider the four-site system depicted in part a of Fig. 5.2. In the real space basis (w_i, p_i) , where w_i labels the wedge and p_i the sites in the wedge according to Fig. 5.2, the inverse lattice Green's function takes the form

$$G_{\text{lat}}^{-1}(\omega) = \begin{pmatrix} (1, 1) & (1, 2) & (2, 1) & (2, 2) \\ \omega + \mu(r_1) - \Sigma_1 & t & t & 0 \\ t & \omega + \mu(r_2) - \Sigma_2 & 0 & 0 \\ t & 0 & \omega + \mu(r_1) - \Sigma_1 & t \\ 0 & 0 & t & \omega + \mu(r_2) - \Sigma_2 \end{pmatrix} \quad (5.14)$$

Using the transformation Eq. (5.13), we obtain the inverse lattice Green's function in the basis (r, p) ,

$$G_{\text{lat}}^{-1}(\omega) = \begin{pmatrix} & (1, 1) & (1, 2) & (2, 1) & (2, 2) \\ \begin{pmatrix} \omega + \mu(r_1) - \Sigma_1 + t & t & 0 & 0 \\ t & \omega + \mu(r_2) - \Sigma_2 & 0 & 0 \\ 0 & 0 & \omega + \mu(r_1) - \Sigma_1 - t & t \\ 0 & 0 & t & \omega + \mu(r_2) - \Sigma_2 \end{pmatrix} \end{pmatrix}, \quad (5.15)$$

where the matrix assumes a block diagonal form, which reduces the numerical effort to invert the matrix considerably. The external potential $\mu(r)$ and the self-energy are the same for the same point number, irrespective of the wedge number. This holds also for the general three-dimensional case. Thus, as mentioned above, it is sufficient to store the self-energy only for the inequivalent points. In the numerical implementation, the hopping matrix, which is independent of the DMFT self-consistency loop, is stored separately and added to the diagonal elements in each separation.

Lattice sites on symmetry planes slightly complicate the situation. In our one dimensional example, this is the case if one lattice site sits at the mirror plane, see part b of Fig. 5.2. This can be solved in the following way. One still obtains $G_{\text{lat}}^{-1}(\omega)(r, p_1, p_2)$ using (5.13), where both $(w = 1, p = 1)$ and $(w = 2, p = 1)$ label the same site, i.e. one notationally splits the site in two sites. Since the site is now labeled by two entries in the basis, in the real-space matrix $G_{\text{lat}}^{-1}(\omega)((w_1, p_1), (w_2, p_2))$, not only the "real" diagonal entries $((w = 1, p = 1), (w = 1, p = 1))$ and $((w = 2, p = 1), (w = 2, p = 1))$, but also the entries $((w = 1, p = 1), (w = 2, p = 1))$ and $((w = 2, p = 1), (w = 1, p = 1))$ are set equal to the diagonal entry for the original site, where a factor $1/2$ is introduced. Furthermore a factor $1/\sqrt{2}$ is used for all hoppings connecting one of the two fictitious sites, represented by the four "diagonal" entries, to other sites. In this way, in the unitary transform the symmetric eigenvector \hat{u}_1 "adds" the two fictitious sites to one with the old diagonal entry, whereas the antisymmetric eigenvector \hat{u}_2 produces a zero diagonal entry, which is completely decoupled from all other sites. Thus, in the (r, p_1, p_2) basis, one has enlarged the matrix by a decoupled zero diagonal entry. In the general case, if a site sits on a symmetry surface belonging to d_i wedges, one splits up the site into d_i copies, one belonging to each wedge, and introduces "degeneracy factors" $1/d_i$ for the diagonal entries and $1/\sqrt{d_i}$ for the hoppings of the site. Only eigenvectors which are symmetric with respect to the wedges hosting the degenerate site will reproduce the old value, whereas antisymmetric eigenvectors will produce decoupled zero entries. Since these entries are physically meaningless, it is helpful to set them to an arbitrary finite value other than zero in the numerical implementation. Otherwise taking the numerical inverse will produce high numerical values which makes the inverse less exact. As an example let us consider the simple system depicted in Fig. 5.2 b. After splitting up the site on the mirror plane in two fictitious sites, the inverse

Green's function in (w_i, p_i) -space takes the form

$$G_{\text{lat}}^{-1}(\omega) = \begin{pmatrix} (1,1) & (1,2) & (2,1) & (2,2) \\ \frac{\omega + \mu(r_1) - \Sigma_1}{2} & \frac{t}{\sqrt{2}} & \frac{\omega + \mu(r_1) - \Sigma_1}{2} & \frac{t}{\sqrt{2}} \\ \frac{t}{\sqrt{2}} & \omega + \mu(r_2) - \Sigma_2 & \frac{t}{\sqrt{2}} & 0 \\ \frac{\omega + \mu(r_1) - \Sigma_1}{2} & \frac{t}{\sqrt{2}} & \frac{\omega + \mu(r_1) - \Sigma_1}{2} & \frac{t}{\sqrt{2}} \\ \frac{t}{\sqrt{2}} & 0 & \frac{t}{\sqrt{2}} & \omega + \mu(r_2) - \Sigma_2 \end{pmatrix}, \quad (5.16)$$

where only the two real sites (1, 2) and (2, 2) are not coupled and the degeneracy factors have been introduced. Using equation (5.13), we obtain the inverse Green's function in (r, p) space,

$$G_{\text{lat}}^{-1}(\omega) = \begin{pmatrix} (1,1) & (1,2) & (2,1) & (2,2) \\ \omega + \mu(r_1) - \Sigma_1 & \sqrt{2}t & 0 & 0 \\ \sqrt{2}t & \omega + \mu(r_2) - \Sigma_2 & 0 & 0 \\ 0 & 0 & 0 & 0 \\ 0 & 0 & 0 & \omega + \mu(r_2) - \Sigma_2 \end{pmatrix}, \quad (5.17)$$

where the (2, 1)(2, 1) entry is 0 and completely decoupled. It can be easily checked that inverting this matrix and transforming back to (w_i, p_i) gives the same result as directly inverting the 3×3 inverse Green's function in real space.

In two dimensions, the symmetry group G_{2D} of the cubic lattice consists of eight symmetry operations, see part a of Fig. 5.3. Thus, the lattice can be split up in eight identical wedges. One can now number the wedges as follows. First, mark an arbitrary wedge as 1. Then, act on it with group element g_i to obtain wedge number i (see Fig. 5.3). Let $(\vec{e}_i)_j = \delta_{i,j}$ be the unit vector labeling the i th wedge. To construct the eigenvectors of the unitary transformation to block form, we again make use of the regular representation $R_{\text{reg}}(g_i)$, which now consists out of 8×8 matrices. More than in the trivial one-dimensional case, one can now appreciate the fact that $R_{\text{reg}}(g_i)\vec{e}_1$ conveniently gives the unit vector \vec{e}_i labeling wedge i . As mentioned above, the main difference between one dimension and two or three dimensions is the fact that the symmetry group of the two- and three-dimensional cubic lattice is not abelian. In two dimensions, one two-dimensional irreducible representation exists, which makes the notation more cumbersome. The eigenvectors are now given by

$$\vec{u}_{r,m,k} = \frac{\dim(R_r)}{\dim(G_{2D})} \sum_{i=1}^{\dim(G_{2D})} (R_r(g_i))_{m,k} R_{\text{reg}}(g_i)\vec{e}_1, \quad (5.18)$$

where the irreducible representation r appears with the multiplicity $1 \leq m \leq \dim(R_r)$ with $1 \leq k \leq \dim(R_r)$ eigenvectors. While in (w_i, p_i) -space one can write down the inverse Green's function matrix as usual, it acquires three additional indices in the reduced space,

$$G_{\text{lat}}^{-1}(\omega)(r, m, p_1, p_2, k_1, k_2) = \sum_{i_1=1}^{\dim(G_{1D})} \sum_{i_2=1}^{\dim(G_{1D})} (\hat{u}_{r,m,k_1})_{i_1} G_{\text{lat}}^{-1}(\omega)((w_{i_1}, p_1), (w_{i_2}, p_2)) (\hat{u}_{r,m,k_2})_{i_2}, \quad (5.19)$$

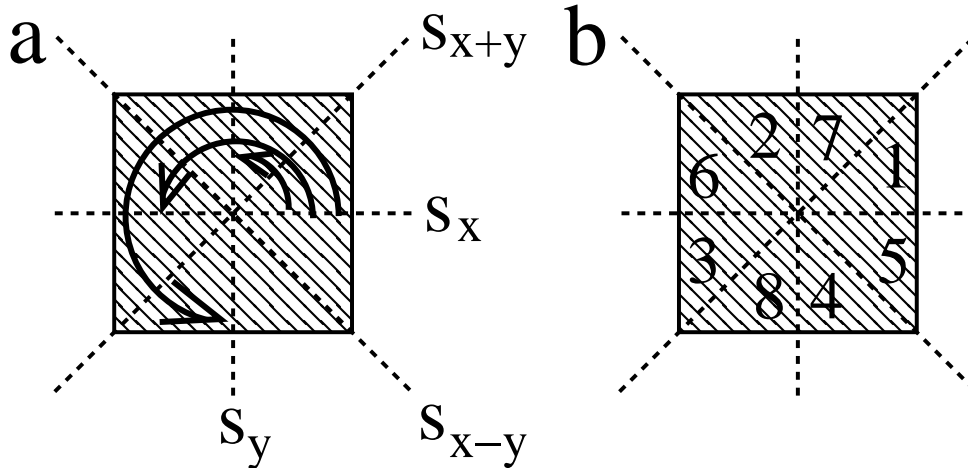


Figure 5.3: Symmetry group of the two-dimensional cubic lattice. Part a: the group contains eight symmetry operations; the identity e , three rotations, $R_{\pi/4}$, $R_{\pi/2}$, $R_{3\pi/4}$, by $\pi/4$, $\pi/2$ and $3\pi/4$, respectively, and four reflections, S_x , S_y , S_{x+y} and S_{x-y} . Part b: the lattice consists of eight identical wedges. If the group elements are put into the order $\{e, R_{\pi/4}, R_{\pi/2}, R_{3\pi/4}, S_x, S_y, S_{x+y}, S_{x-y}\}$ and one arbitrary wedge is identified as wedge "one", one can number the wedges according to the order of the group elements acting on wedge one.

i.ẽ. the Green's function is diagonal in r, m , while each (r, m) -block has dimension $n_{\text{inequivalent}} \dim(R_r)$, according to Eq. (5.7).

For the three-dimensional cubic lattice, there are 48 symmetry operations. Thus the lattice can be split up in 48 wedges. There are four one-dimensional, two two-dimensional and four three-dimensional irreducible representations. The group symmetry can be implemented in complete analogy to the two-dimensional case. The eigenvectors can be constructed using Equation (5.18) and the inverse Green's function can be brought to block diagonal form using Equation (5.19), which reduces the numerical effort considerably, as mentioned above.

5.3 Mott metal-insulator transition in an optical lattice

In contrast to a solid, where the positive background charge of the ions prevent the electrons from leaving the piece of material altogether, in an optical lattice an additional potential is needed to constrain the atoms. In most experiments, an harmonic potential V_{harmonic} is used, which breaks the translational symmetry and makes the system inhomogeneous. The physics displayed in the trap crucially depends on V_{harmonic} . E.g., the boundary sites of the trap necessarily have a small occupation $n_{\text{boundary}} \ll 0.5$ and are therefore always metallic, independently of the choice of the Coulomb repulsion U . Only if V_{harmonic} is deep

and $U > U_c$ is large enough, a Mott insulating region can build up in the center of the trap. If V_{harmonic} is even deeper, the center has an occupation $n_{\text{center}} \approx 1$, and thus will again be metallic. Then, for $U > U_c$, a Mott-insulating region can just be found in an onion shell between center and boundary. We already see that, if we are studying the Mott transition in an optical lattice, we have to deal with strong inhomogeneities and coexisting phases.

For one-dimensional systems, a wide arsenal of theoretical tools exists to describe the Mott transition of fermionic atoms in an optical lattice. E.g., the Density Matrix Renormalization Group and Quantum Monte Carlo methods are commonly used [81–83]. Also analytical methods such as the Bethe-ansatz have been used [81]. However, the physics in one dimension is different from the physics in two or three dimensions. E.g., the aspect of spin-charge separation in the Luttinger liquid away from half filling represents a fundamental difference. Furthermore the Mermin-Wagner theorem prevents symmetry breaking in one dimension. Also Rigol et al. [82, 83] argue that the Mott transition in one-dimensional traps cannot be observed in time-of-flight experiments, in contrast to the results for three-dimensional systems presented below.

A significant part of the theoretical work on three-dimensional optical lattices has been done in the local density approximation (LDA), see e.g. [81], where one describes the lattice locally as a homogeneous system. This approximation should not be confused with the local density approximation in the context of the density functional theory. It is bound to fail at inhomogeneous situations such as a boundary between a metal and a insulator. Our more general method allows us to evaluate the quality of such an approximation.

Using the method described in the previous section, we study a fermionic Hubbard model on a three-dimensional cubic lattice,

$$\mathcal{H} = -t \sum_{\langle ij \rangle, \sigma} c_{i\sigma}^\dagger c_{j\sigma} + U \sum_i n_{i\uparrow} n_{i\downarrow} + V_0 \sum_{i,\sigma} r_i^2 n_{i\sigma}, \quad (5.20)$$

c.f. (2.6). Here $V_0 \sum_{i,\sigma} r_i^2 n_{i\sigma}$ represents the harmonic potential. We consider a lattice with 4224 sites located in a sphere with radius $R = 10$, where we set the lattice distance to unity. The sites are located at $(i + 1/2, j + 1/2, k + 1/2)$ with $i, j, k \in \mathbb{N}$, i.e. the center of the trap is located in the middle of 8 center sites. The strength of the harmonic potential $V_0 = 0.047D$ in units of half the bandwidth D is chosen such that all sites with radius $r > 10$ are unoccupied and therefore can be neglected. Only $n_{\text{inequivalent}} = 118$ of the 4224 sites are inequivalent. Thus, using the group theory described in the previous section, we only have to deal with 118 impurity problems per DMFT iteration. As already mentioned, we restrict ourselves to paramagnetic solutions, simplifying the already very complex numerics. Furthermore temperatures where magnetic ordering is expected are experimentally very hard to reach.

The NRG is used as an impurity solver, see Section 2.4.2. For all results $\Lambda = 1.5$ and 60 shells are used and 800 states are kept. Convergence is reached after roughly 50 iterations, which is surprisingly fast for the complex numerics at hand. Also, the convergence is relatively insensitive to the amount of weight kept from the previous iteration, where values between 20 and 50 percent are used. Two different kinds of calculation are done, one where

the external potential $\mu = \mu_0 - V_0 r^2$ including the chemical potential μ_0 and the harmonic potential $V(r) = -V_0 r^2$ is kept fixed and another one where the overall occupation of the trap is kept fixed. For the latter calculations, in each DMFT iteration the occupation of the inequivalent sites is determined directly in the NRG run as a thermodynamic quantity. The height of the chemical potential μ_0 is then adjusted according to

$$\mu_0 \rightarrow \mu_0 + c(n_{\text{set}} - n_{\text{actual}}), \quad (5.21)$$

where n_{set} is the desired and n_{actual} the actual occupation per site. It turns out that for the constant c values around 2.0 work well. To avoid the use of fitting procedures for the computed self-energies, the same grid for the energy ω is used for all NRG runs. The grid goes from $\omega = -8D$ to $\omega = +8D$ in steps of $0.01D$, except for a region around $\omega = 0$ which is discretized logarithmically to capture the Kondo effect correctly. For high energies in general the resolution of the NRG is not so good and the self-energies and spectral functions are captured rather qualitatively than quantitatively. For values of μ in the band-insulating regime, $\mu \ll -U/2 - D/2$ or $\mu \gg U/2 + D/2$, respectively, the results are improved by the fact that the self-energy goes towards zero, $\Sigma(\omega) \approx 0$. Due to these problems at high energies, the occupation computed from the spectral functions is not very accurate. To normalize the results to the total weight of the spectral function improves the results only slightly. In order to have a good convergence, it is thus important to use the thermodynamically calculated occupation in Equation (5.21) rather than the occupation determined from the spectral functions.

In Fig. 5.4 the occupation of the lattice sites is plotted as a function of the radius. In the main panel, the number of particles $N = 2869$ and the temperature $T = 0$ are held fixed while the interaction U/t is varied. All variables in Fig. 5.4 are given in units of $D = 6t$, which is half the bandwidth. For the limiting case of zero interaction $U = 0$, the Hamiltonian can be diagonalized exactly. In this limit, also the DMFT results are exact, since the self-energy is zero. The center of the trap is band-insulating, up to a radius $r \lesssim 6$, where the metallic regime begins. For radii $r \gtrsim 8$, the system is band-insulating again. One observes that for increasing interaction the atoms are pushed away from the center of the trap. For $6 < r < 7$, the $U = 2.0D$ curve already shows a shoulder, where the compressibility $\partial n / \partial \mu$ is decreasing. At $U = 3.0D$ the transition has occurred and the Mott insulating region manifests itself in plateau where the compressibility has vanished, $\partial n / \partial \mu = 0$. This is consistent with the transition in the bulk which occurs at $U_c = 2.52D$. The incompressible Mott-insulating onion shell extends between $5.5 \lesssim r \lesssim 7.5$. This region grows with increasing U until $U = 4.5D$, where the metallic region in the center of the trap has vanished and is replaced by a Mott-insulator that extends up to $r \lesssim 7.5$. The upper inset of Fig. 5.4 shows the occupation for different particle number at $U = 4.5D$ and $T = 0$. Due to the harmonic potential, $|\partial \mu / \partial r|$ becomes smaller towards the center of the trap. Therefore the metallic onion ring becomes wider for decreasing particle number. In the lower inset, the occupation curves at $N = 2869$ and $U = 4.5D$ are depicted for varying temperatures. Quite surprisingly, the occupation curve is insensitive to increasing the temperature up to values of several T_c , where T_c is the critical temperature of the metal-insulator transition in a homogeneous system. DMFT/NRG results give $T_c \approx 0.035D$,

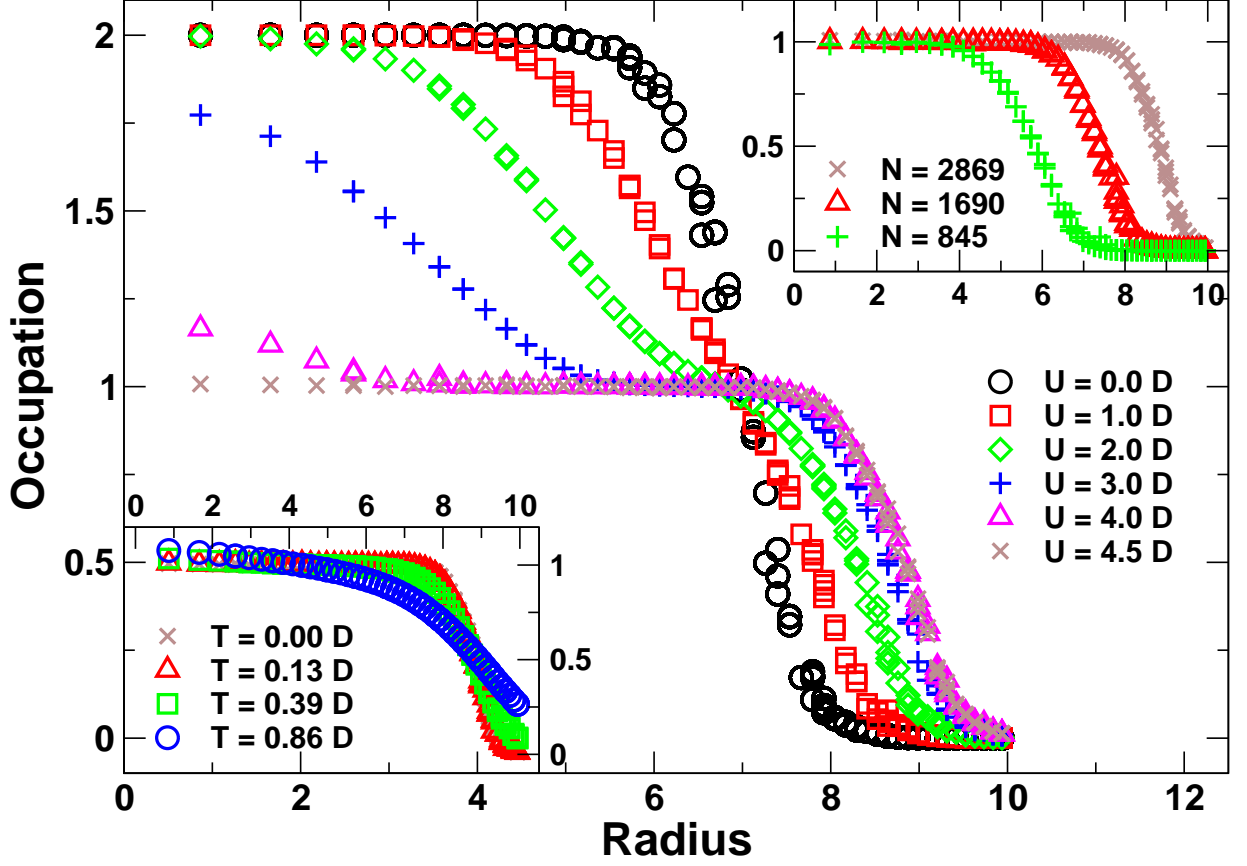


Figure 5.4: The number of fermionic atoms $\langle n_i \rangle = \langle n_{i,\uparrow} + n_{i,\downarrow} \rangle$ per lattice site, as a function of the distance r to the origin. The signature of the Mott insulating phase is the presence of a plateau with $\langle n_i \rangle = 1.0$. Note that there are inequivalent sites with different occupation but the same distance r . Main panel: Crossover from weak to strong interactions for a fixed number $N = 2869$ of particles in the trap at $T = 0$, and $U = 6J$. Upper inset: Dependence on the number of particles for $U = 4.5D$, and $T = 0$. Lower inset: T dependence for $U = 4.5D$, $N = 2869$ (the $T = 0$ and $T = 0.13D$ curves lie on top of each other).

c.f. Fig. 2.3. Due to the exponential thermal activation of the Mott gap with increasing temperature, the Mott plateau is smeared out, which can be observed for the $T = 0.39D$ curve and is clearly visible at $T = 0.86D$.

Fig. 5.5 shows the spectral functions $A_i(\omega) = -\frac{1}{\pi} \text{Im} G_{\text{lat}}(x_i, x_i, \omega)$ of sites along the axis $y = z = 1/2$ from the center to the edge of the trap for $U = 4.5D$, $N = 2869$, and two different temperatures. Since for the higher temperature the occupation at the boundary of the trap increases, c.f. inset of Fig. 5.4, the external potential of the higher temperature is shifted by $-0.1D$, $\mu_{T=0.13D}(r) = \mu_{T=0.0014D}(r) - 0.1D$. Thus all spectral functions of the higher temperature are shifted by about $0.1D$. For this set of parameters, the site $(1/2, 1/2, 1/2)$, representing the eight central sites, is Mott insulating and clearly characterized by the two Hubbard bands. The spectral function in the gap $A(\omega \approx 0)$

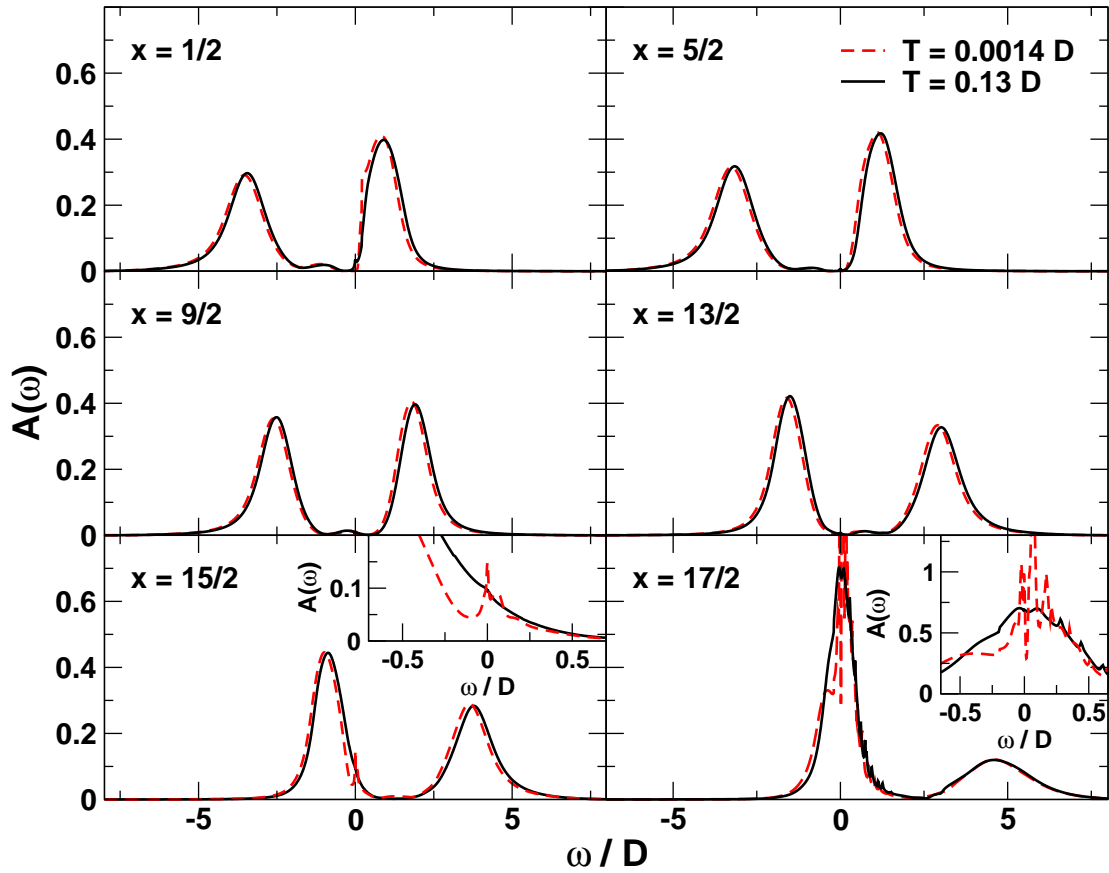


Figure 5.5: Local spectral functions in the Mott insulating phase ($U = 4.5D$, $N = 2869$) for two different T for lattice points with coordinates $(x, 1/2, 1/2)$. Left inset: The coherence peak at the Fermi energy, characteristic for a strongly correlated metal, vanishes with increasing T . Right inset: Close to edge of the atomic cloud, where the potential becomes steep, finite size effects are visible.

becomes very small but never vanishes exactly due to the thermal activation of the gap. The chemical potential sits close to the right Hubbard band. If one goes along the axis to the site $(13/2, 1/2, 1/2)$, the chemical potential is shifted through the gap. Here the problems of the NRG to resolve high energies become obvious. While one shifts the chemical potential through the gap, the form of the Hubbard band should not change. However, in the panels one can observe that the Hubbard band further away of the chemical potential looks smaller and broader since the NRG delivers less energy points and the used broadening is larger. At site $(15/2, 1/2, 1/2)$ the chemical potential reaches the lower Hubbard band and at the lower temperature, a quasi-particle peak becomes visible (see inset). The Kondo temperature T_K in the impurity model is obviously $T_K \ll 0.13D$ and thus the Kondo effect is suppressed at $T = 0.13D$. Strictly speaking, no Mott-insulating regions exists in the trap at temperature $T = 0$, since the neighboring metal always penetrates the insulator, c.f. Chapter 3. However, since the quasi-particle weight drops off rapidly, the quasi-

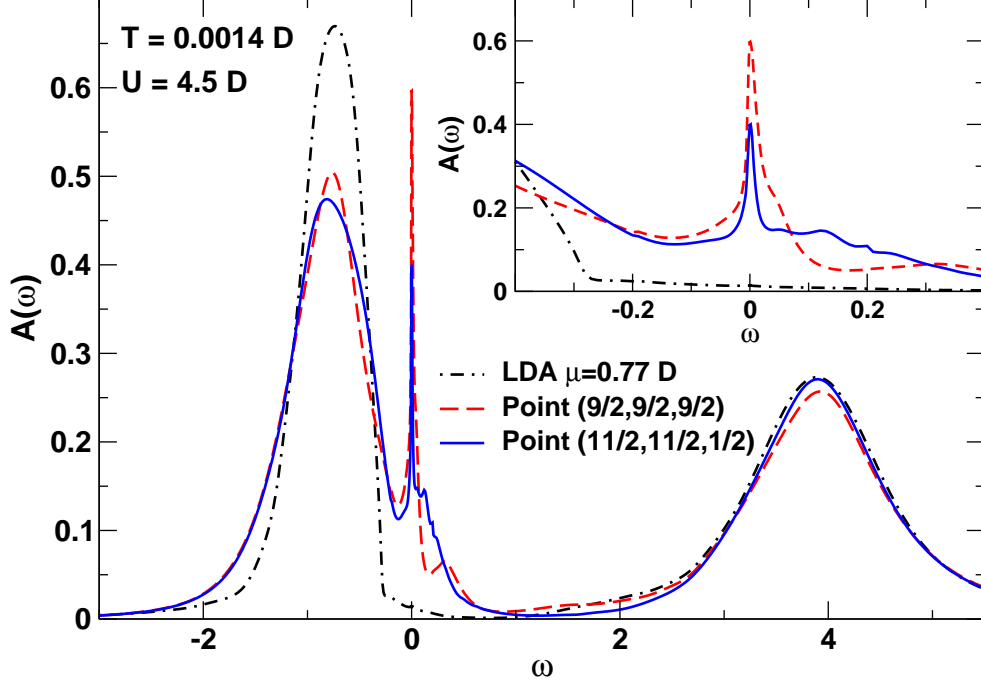


Figure 5.6: Local spectral function of two non-equivalent lattice points at distance 7.794 from the origin at the boundary of the Mott insulating region ($T = 0.0014D$, $U = 4.5D$). Here the LDA (dot-dashed line) fails completely to describe the spectral function but still reproduces the occupation with high accuracy ($n_{1/2(9,9,9)} = 0.481$, $n_{1/2(11,11,1)} = 0.482$, $n_{\text{LDA}} = 0.496$).

particle-peak can hardly be resolved and can be neglected (see Chapter 3). Furthermore, the complete penetration of the metallic phase is a zero temperature artefact. At finite temperature T , all Kondo resonances with Kondo temperature $T_K < T$ will be suppressed. The last panel of Fig. 5.5 shows site $(17/2, 1/2, 1/2)$ where the metallic Fermi liquid regime is reached. The imaginary part of the self-energy becomes zero at $\omega = 0$ and thus finite size effects become visible around $\omega = 0$. As expected, these effects are smoothed out at higher temperatures (see inset).

The spectral functions can presently not be measured experimentally, but they are very interesting from a theoretical point of view. Many theoretical works on optical lattices have been done in the local density approximation (LDA), see above. Our method allows us to evaluate the quality of the LDA. In Fig. 5.6, the spectral functions of the two inequivalent sites $(9/2, 9/2, 9/2)$ and $(11/2, 11/2, 1/2)$ with the same distance 7.794 to the origin for $U = 4.5D$ and $T = 0.0014D$ have been plotted. The sites sit in the metallic regime close to the boundary of the Mott-insulating region. The chemical potential has merged with the lower Hubbard band and a quasi-particle peak can be observed. As comparison, the LDA spectral function is shown, which is computed with a usual bulk DMFT program with the same parameters $U = 4.5D$ and $T = 0.0014D$ and with a chemical potential μ_{bulk} corresponding to the external potential $\mu(r) = \mu_0 - V_0 r^2$ of the two sites above,

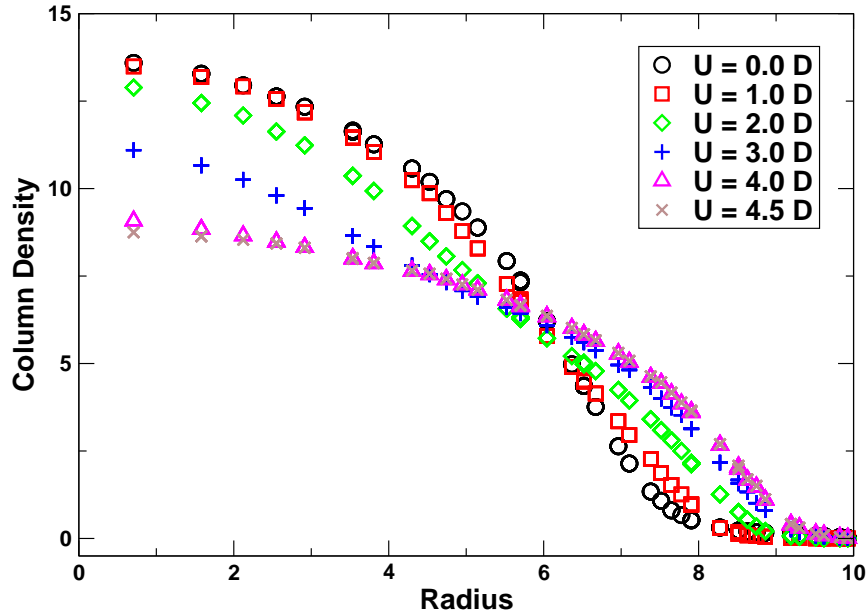


Figure 5.7: Column Density $n_{\text{column}}(x, y) = \int dz n(x, y, z)$ for $T = 0$ and $N = 2869$. The Mott plateau of Fig. 5.4 is washed out and no clear sign of the Mott transition can be observed.

$\mu_{\text{bulk}} = \mu_{1/2(9,9,9)} = \mu_{1/2(11,11,1)} = 0.77D$. In contrast to the other two solutions, the LDA spectral function clearly shows Mott-insulating behavior. The striking difference can be explained by the missing neighboring metallic regime which penetrates the Mott-insulator. Despite the complete failure to describe the spectral function correctly, the LDA still reproduces the occupation correctly, $n_{1/2(9,9,9)} = 0.481$, $n_{1/2(11,11,1)} = 0.482$, $n_{\text{LDA}} = 0.496$. Thus, as expected, the LDA fails close to a boundary between different phases.

The hallmark of the Mott-insulating phase in Fig. 5.4 is the plateau expressing the incompressibility of the insulator. Unfortunately, this plateau cannot be detected directly in an absorption experiment, where the column density is measured, $n_{\text{column}}(x, y) = \int dz n(x, y, z)$. The results for the same parameters as in the main panel of Fig. 5.4, $N = 2869$ and $T = 0$, are shown in Fig. 5.7. The Mott plateau is washed out and no clear signature of the Mott transition can be observed. However, one can design an experiment using the column density in order to detect the Mott transition in the following way (we thank the group of Immanuel Bloch for valuable suggestions). By increasing the harmonic potential V_0 one can probe the compressibility of the atoms in the trap. In Fig. 5.8 the occupation as a function of the radius is plotted for $U = 4.5D$, $T = 0$, $N = 1520(845)$ atoms in the left(right) panel and varying V_0 . With increasing V_0 , the trap potential becomes steeper and the atoms are pressed towards the center of the trap. In the left panel of Fig. 5.8, the incompressibility of the Mott phase is evident, extending from the center of the trap up to a radius of about 6. The occupation in this region remains unchanged with increasing V_0 , until the center of the trap becomes metallic at $V_0 = 0.081D$. While the remaining Mott-insulating onion ring is still incompressible, the metallic center can easily

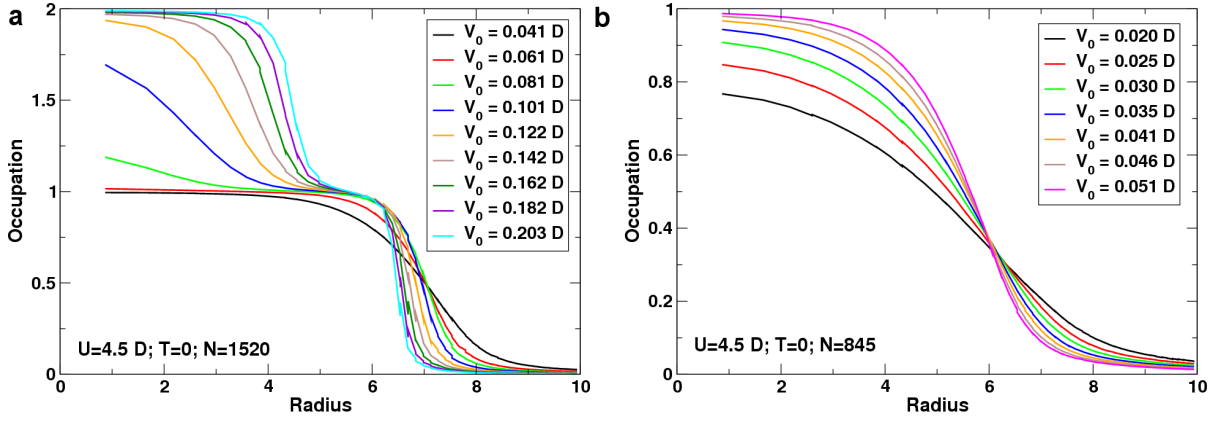


Figure 5.8: The number of fermionic atoms per lattice site, as a function of the distance r to the origin for $U = 4.5D$, $T = 0$, and $N = 1520(845)$ atoms in the trap in the left(right) panel. With increasing V_0 , the trap potential becomes steeper and the particles are pressed towards the center of the trap. One can clearly observe the incompressibility of the Mott phase (see text).

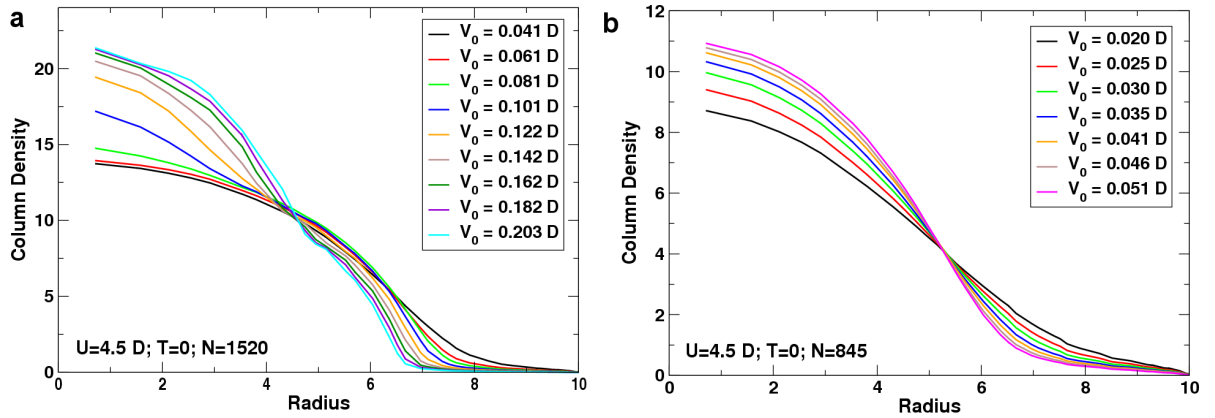


Figure 5.9: Column Density $n_{\text{column}}(x, y) = \int dz n(x, y, z)$ for $U = 4.5D$, $T = 0$, and $N = 1520(845)$ atoms in the trap in the left(right) panel. Comparing with Fig. 5.8, one observes that while the Mott plateau is still washed out, the Mott transition can be detected by looking at the Column density at the center of the trap. With increasing V_0 , the column density at the center remains constant if the center is in the incompressible Mott-insulating or band-insulating phase, respectively.

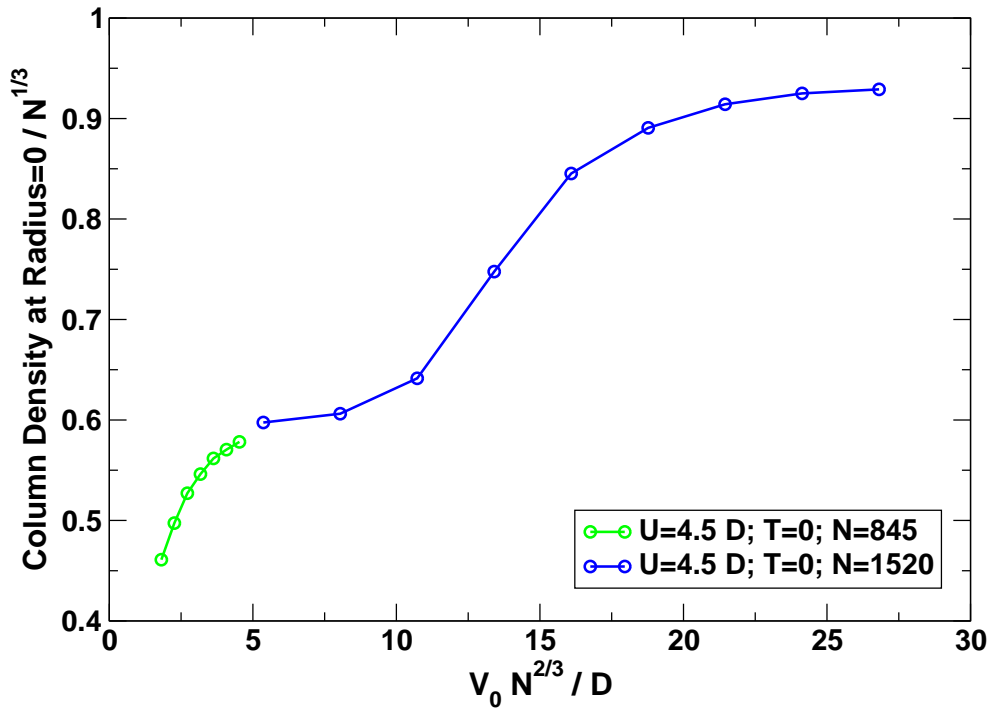


Figure 5.10: The column density at the center of the trap $n_{\text{column}}(0,0)$ as a function of the strength V_0 of the confining harmonic potential. Both axis are scaled such that they are independent of the numbers of atoms in the trap. One clearly observes a plateau of $n_{\text{column}}(0,0)$ as a function of V_0 , a signature of the incompressible Mott phase.

be compressed until it becomes band-insulating at $V_0 = 0.142D$. Having the maximal occupation of two, the band-insulating sites are naturally incompressible as well. Since the numerical effort increases with increasing trap size, only traps up to a radius of 10 are considered. As a consequence, with $N = 1520$ atoms in the trap, the center of the trap is never less than half-filled. To access this regime, the case of $N = 845$ is considered in the right panel of Fig. 5.8. With increasing V_0 , the center of the trap is first metallic and then becomes Mott-insulating, where again it is clearly visible that the metal is compressible while the Mott insulator is incompressible. The Column density for the same parameters as in Fig. 5.8 is plotted in Fig. 5.9. While the Mott plateau is still washed out, the Column density at the center, $n_{\text{column}}(0,0)$, of the trap reflects the incompressibility typical for the Mott- and band-insulator. In the left panel, for $V_0 < 0.081D$, $n_{\text{column}}(0,0)$ remains constant, then increases with increasing V_0 until the band-insulating regime is reached at $V_0 = 0.162D$. In the right panel, $n_{\text{column}}(0,0)$ increases until $V_0 = 0.041D$ is reached. To compare $n_{\text{column}}(0,0)(V_0)$ as a function of V_0 for the two set of parameters, one has to rescale the V_0 -axis and the $n_{\text{column}}(0,0)$ -axis. To see how V_0 scales with N , we first note that for noninteracting particles, the trap is occupied up to a radius r_0 where the external potential $\mu(r) = \mu_0 - V_0 r^2 \sim -V_0 r^2$ reaches the lower band edge, i.e. $V_0 r^2 \sim D$. Since $N \sim r^3$, we have $V_0 \sim D/N^{2/3}$. Approximately, one can regard $n_{\text{column}}(0,0)$ as an integral

over a constant density, i.e. $n_{\text{column}}(0,0) \sim r \sim N^{1/3}$. In Fig. 5.10, $n_{\text{column}}(0,0)/N^{1/3}$ is plotted as a function of $V_0/(D/N^{2/3})$. To a good approximation, all data points seem to lie on one general curve. This curve clearly shows a plateau corresponding to the incompressible Mott phase, which could be a promising way to detect the Mott transition experimentally.

In the following, we show that a signature of the Mott-transition can also be found in time-of-flight experiments. To calculate $n_{\vec{k}}^{\text{tof}} = \int dk_z n_{\vec{k}}/(2\pi)$, we first need to calculate $n_{\vec{k}}$,

$$n_{\vec{k}} = \frac{1}{N} \sum_{i,j} \int d\omega f(\omega) e^{i\vec{k}(\vec{r}_i - \vec{r}_j)} A_{ij}(\omega), \quad (5.22)$$

where $f(\omega)$ is the Fermi function and $A_{ij}(\omega) \equiv -\frac{1}{\pi} \text{Im} G_{ij}(\omega)$ is the spectral function. In the numerical implementation, one works in the reduced space using the group theory of the cubic lattice. I. e., one stores the inverse Green's function $G_{\text{lat}}(\omega)$ as a function of $(r, m, p_1, p_2, k_1, k_2)$, see Section 5.2. It is numerical more efficient to implement Eq. 5.22 in the reduced space,

$$n_{\vec{k}} = -\frac{1}{N} \int \frac{d\omega}{\pi} \sum_{r,m,p_1,p_2,k_1,k_2} \sum_{w_1,w_2} f(\omega) \exp[i\vec{k}\vec{r}(w_1,p_1)] \exp[-i\vec{k}\vec{r}(w_2,p_2)] \text{Im} G_{\text{lat}}(\omega)(r, m, p_1, p_2, k_1, k_2), \quad (5.23)$$

where $\vec{r}(w_i, p_i)$ is the vector pointing to site (w_i, p_i) . The term

$$\sum_{w_1,w_2} \exp[i\vec{k}\vec{r}(w_1,p_1)] \exp[-i\vec{k}\vec{r}(w_2,p_2)] \quad (5.24)$$

can be computed once and stored in an array as a function of (p_1, p_2) , which saves a considerable amount of computing time. In Fig. 5.11 the time-of-flight density $n_{\vec{k}}^{\text{tof}}$ are shown for the same parameters as in Fig. 5.4: $T = 0, N = 2869$. In the band insulator and the Mott insulator, all atoms are localized in real space. Therefore, one expects their wavefunctions to be constant in \vec{k} -space and thus also the time-of-flight density $n_{\vec{k}}^{\text{tof}}$. For the metal, the distribution in \vec{k} -space is not as obvious since there is no Fermi surface due to the harmonic potential. A free particle in the harmonic potential has a Gaussian wave function. Thus, one expects for a free particle also a Gaussian distribution in \vec{k} -space, which is renormalized by interactions. Thus, the metallic $n_{\vec{k}}$ is maximal at $\vec{k} = 0, 0, 0$ and declines towards the edge of the Brillouin zone. Since metallic and insulating regions always coexist, in Fig. 5.4 and Fig. 5.11, the time-of-flight density $n_{\vec{k}}^{\text{tof}}$ is always a mixture of the constant and the Gaussian distribution. For $U = 0.0D$ and $U = 4.5D$, only an onion ring with diameter two is metallic ($6 < r < 8$ for $U = 0.0D$ and $8 < r$ for $U = 4.5D$), while the trap is in a predominately insulating phase (band-insulating or Mott-insulating, Fig. 5.4). For $U = 2.0D$ and $U = 3.0D$, the atoms in the trap are mostly metallic, only small regions of band insulator ($r < 2$ for $U = 2.0D$) and Mott insulator ($5.5 < r < 7.5$

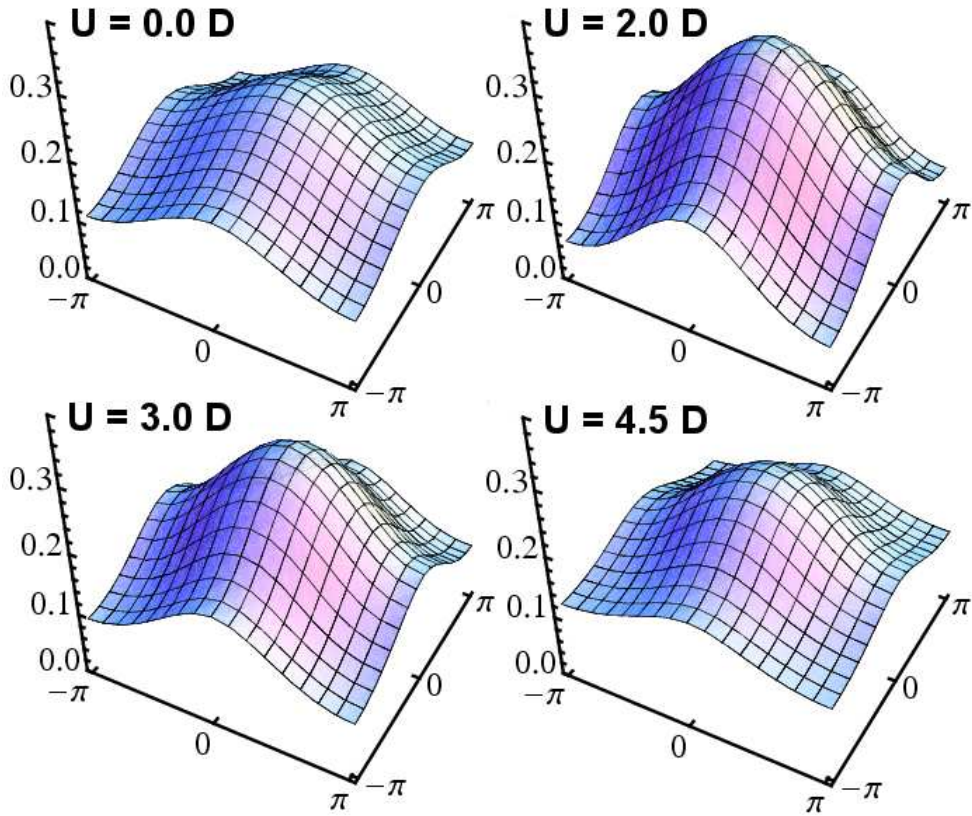


Figure 5.11: Momentum distribution $n_{\vec{k}}^{\text{tof}}$ for $N = 2869$, $T = 0$, and varying $U/D = 0, 2, 3, 4.5$. Both in the predominantly band-insulating phase ($U/D = 0$) and Mott insulating phase ($U/D = 4.5$) the curves are considerably flatter than for $U/D = 2, 3$ where most fermions are in the metallic phase.

for $U = 3.0D$) exist. This leads to a considerably flatter $n_{\vec{k}}^{\text{tof}}$ for $U = 0.0D$ and $U = 4.5D$ in Fig. 5.11.

Since in the homogeneous DMFT the self-energy is \vec{k} -independent, the Fermi surface is always a structureless sphere and only the Fermi energy is renormalized by the interactions [12]. Thus, $n_{\vec{k}}$ is only a function of $\epsilon_{\vec{k}}$. This does not hold for the inhomogeneous DMFT calculations for the optical lattice, due to the harmonic potential. Nevertheless, it turns out that if $n_{\vec{k}}$ or $n_{\vec{k}}^{\text{tof}}$ is plotted as a function of $\epsilon_{\vec{k}} = 2t(\cos(k_x) + \cos(k_y) + \cos(k_z))$, the curve collapses to a line within a very good approximation, see Fig. 5.12. Only in the curves $n_{\vec{k}}(\epsilon_{\vec{k}})$ a small scatter is visible. Since the LDA uses the homogeneous DMFT, the collapse to a single curve is exact. Therefore, our results suggest that LDA is a very good approximation for the analysis of time-of-flight pictures. Here, the question arises if the collapse of the curves is an artefact of our DMFT approximation, where the \vec{k} -dependence enters only through $\epsilon_{\vec{k}}$ but not through the self-energy. While for the experimentally relevant temperature range this is probably a very good approximation, it is expected to fail very close to the metal-insulator transitions at low T .

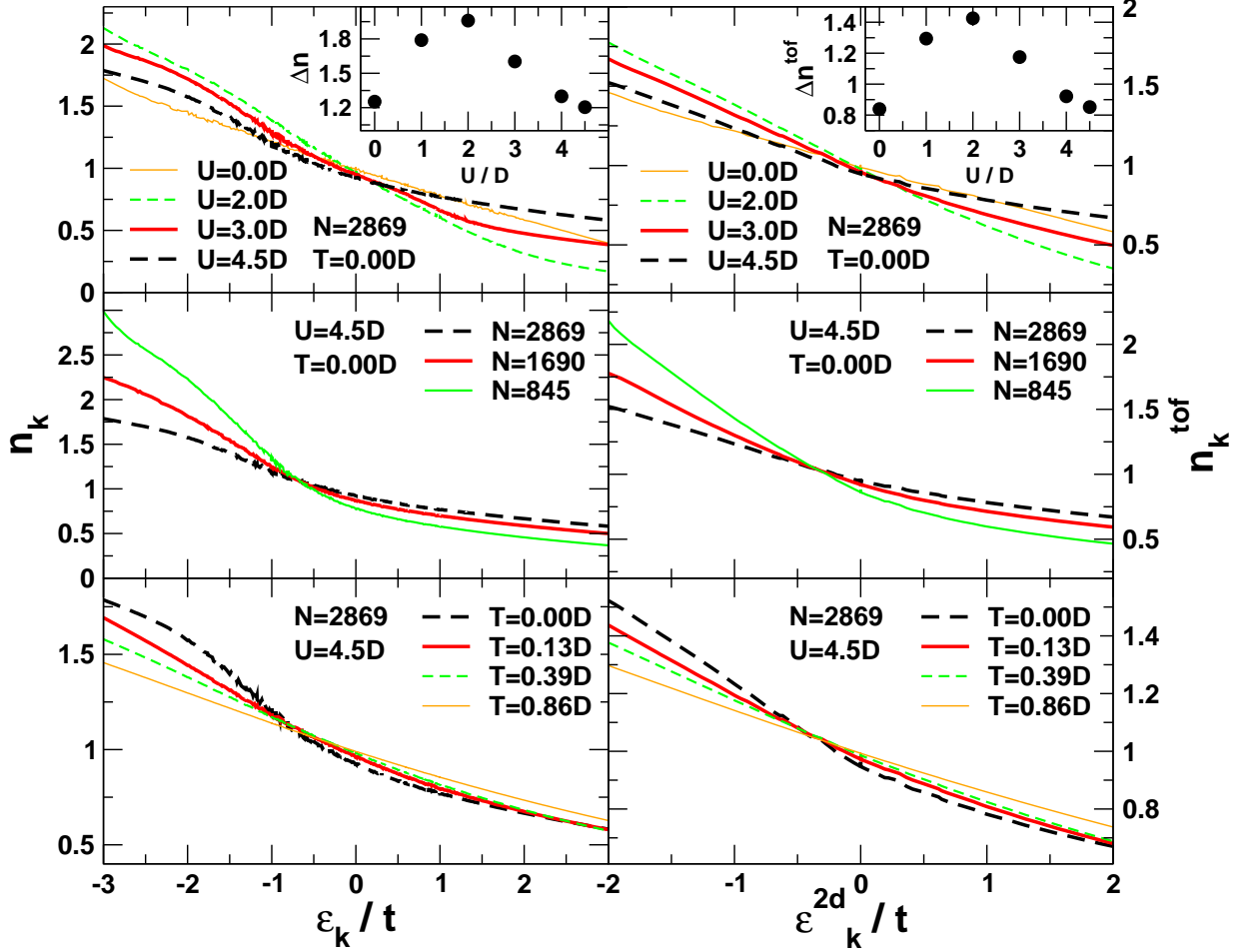


Figure 5.12: $n_{\vec{k}}$ (left panel) and $n_{\vec{k}}^{\text{tof}}$ (right panel) for $\vec{k} = \pi/10(n_x, n_y, n_z)$, $n_{x,y,z} = -10, \dots, 10$, plotted as a function of $\epsilon_{\vec{k}} = -2J(\cos k_x + \cos k_y + \cos k_z)$ and $\epsilon_{\vec{k}}^{2d} = -2t(\cos k_x + \cos k_y)$, respectively, for different values of U , N and T (upper, middle and lower panels, respectively). For a given value of $\epsilon_{\vec{k}}$ a range of values of $n(\epsilon_{\vec{k}})$ exists. Nevertheless, each curve collapses to a single line in good approximation. Inset: $\Delta n = n_{0,0,0} - n_{\pi,\pi,\pi}$ (and $\Delta n^{\text{tof}} = n_{0,0}^{\text{tof}} - n_{\pi,\pi}^{\text{tof}}$) as a function of U . Δn and Δn^{tof} are largest for the predominantly metallic phases and smallest for phases with a large band- (small U) or Mott-insulating (large U) regions.

As mentioned above, one expects $n_{\vec{k}}$ and $n_{\vec{k}}^{\text{tof}}$ to be constant in the insulating phase, where the atoms are localized in real space. In contrast, for the metallic phase one expects a strong dependence on $\epsilon_{\vec{k}}$. Here one has to remind oneself of the homogeneous case, where the density $n(\epsilon_{\vec{k}})$ displays a jump at the chemical potential with the height of the quasi-particle weight Z . Since the harmonic potential $V(r)$ is added to the chemical potential, the external potential $\mu(r)$ varies smoothly within the trap. Hence, the jumps are smeared out. However, the slope of $n(\epsilon_{\vec{k}})$ and $n_{\vec{k}}^{\text{tof}}$ increases if the system becomes more metallic, reminiscent of the homogeneous system where the jump increases with increasing quasi-particle weight. A measure for the slope of $n(\epsilon_{\vec{k}})$ is the difference $\Delta n = n_{0,0,0} - n_{\pi,\pi,\pi}$ or $\Delta n^{\text{tof}} = n_{0,0}^{\text{tof}} - n_{\pi,\pi}^{\text{tof}}$, respectively, which is a good measure of how metallic or insulating the system is. In the upper panels of Fig. 5.12, $n(\epsilon_{\vec{k}})$ and $n_{\vec{k}}^{\text{tof}}$ are shown for the same set of parameters as in Fig. 5.11. As mentioned above, the system is predominately metallic for $U = 0.0D$ and $U = 4.5D$, while for $U = 2.0D$ and $U = 3.0D$ it is predominately insulating, which is reflected by the steeper slopes for the $U = 2.0D$ and $U = 3.0D$ curves. The inset of Fig. 5.12 illustrates how the system evolves from a predominately band-insulating to a predominately Mott-insulating via a metallic phase with increasing U/D . The upper inset of Fig. 5.4 shows how the Mott-insulating region shrinks if the particle number is reduced at $U = 4.5D$. In the middle panels of Fig. 5.12 $n(\epsilon_{\vec{k}})$ and $n_{\vec{k}}^{\text{tof}}$ are plotted for the same set of parameters. Clearly, the reduction of the Mott insulator leads to an increasing slope. The lower panels of Fig. 5.12 show that with increasing temperature, the destruction of quantum coherence leads to a flattening of $n(\epsilon_{\vec{k}})$ and $n_{\vec{k}}^{\text{tof}}$. Note that both $n(\epsilon_{\vec{k}})$ and $n_{\vec{k}}^{\text{tof}}$ are more sensitive to changes of T compared to $\langle n_i \rangle$, see Fig. 5.4.

Bibliography

- [1] N. W. Ashcroft and N. D. Mermin, *Solid State Physics*, Brooks/Cole, 1976.
- [2] A. Altland and B. Simons, *Condensed Matter Field Theory*, Cambridge University Press, 2006.
- [3] W. Kohn, *Rev. Mod. Phys.* **71**, 1253 (1999).
- [4] J. Hubbard, *Proc. Roy. Soc. London Ser. A* **276**, 238 (1963).
- [5] M. C. Gutzwiller, *Phys. Rev. Lett.* **10**, 159 (1963).
- [6] J. Kanamori, *Progress of Theoretical Physics* **30**, 275 (1963).
- [7] D. Pines and P. Nozieres, *The Theory of Quantum Liquids*, W. A. Benjamin, 1966.
- [8] J. W. Negele and H. Orland, *Quantum Many-Particle Systems*, Perseus Publishing, 1998.
- [9] N. F. Mott, *Rev. Mod. Phys.* **40**, 677 (1968).
- [10] A. Georges, G. Kotliar, W. Krauth, and M. J. Rozenberg, *Rev. Mod. Phys.* **68**, 13 (1996).
- [11] W. Metzner and D. Vollhardt, *Phys. Rev. Lett.* **62**, 324 (1989).
- [12] E. Müller-Hartmann, *Zeitschrift für Physik B Condensed Matter* **76**, 211 (1989).
- [13] E. Müller-Hartmann, *Zeitschrift für Physik B Condensed Matter* **74**, 507 (1989).
- [14] E. Müller-Hartmann, *International Journal of Modern Physics B* **3**, 2169 (1989).
- [15] A. Georges and G. Kotliar, *Phys. Rev. B* **45**, 6479 (1992).
- [16] M. Jarrell, *Phys. Rev. Lett.* **69**, 168 (1992).
- [17] A. C. Hewson, *The Kondo Problem to Heavy Fermions*, Cambridge University Press, 1997.
- [18] R. Bulla, T. A. Costi, and D. Vollhardt, *Phys. Rev. B* **64**, 045103 (2001).

- [19] R. Bulla, *Phys. Rev. Lett.* **83**, 136 (1999).
- [20] M. Potthoff and W. Nolting, *Phys. Rev. B* **60**, 7834 (1999).
- [21] M. Potthoff, *European Physical Journal B* **32**, 429 (2003).
- [22] S. Okamoto and A. J. Millis, *Phys. Rev. B* **70**, 241104 (2004).
- [23] A. Georges and W. Krauth, *Phys. Rev. B* **48**, 7167 (1993).
- [24] M. Caffarel and W. Krauth, *Phys. Rev. Lett.* **72**, 1545 (1994).
- [25] H. Schweitzer and G. Czycholl, *Z. Phys. B* **79**, 377 (1990).
- [26] K. Yosida and K. Yamada, *Prog. of Theor. Phys.* **46**, 244 (1970).
- [27] K. Yamada, *Prog. of Theor. Phys.* **53**, 970 (1975).
- [28] K. Yosida and K. Yamada, *Prog. of Theor. Phys.* **53**, 1286 (1975).
- [29] V. Zlatic, B. Horvatic, and D. Sokcevic, *Z. Phys. B* **59**, 151 (1985).
- [30] M. J. Rozenberg, G. Kotliar, and X. Y. Zhang, *Phys. Rev. B* **49**, 10181 (1994).
- [31] H. Kajueter and G. Kotliar, *Phys. Rev. Lett.* **77**, 131 (1996).
- [32] H. Kajueter, G. Kotliar, and G. Moeller, *Phys. Rev. B* **53**, 16214 (1996).
- [33] W. Nolting and W. Borgiel, *Phys. Rev. B* **39**, 6962 (1989).
- [34] M. Potthoff, T. Wegner, and W. Nolting, *Phys. Rev. B* **55**, 16132 (1997).
- [35] A. Martin-Rodero, E. Louis, F. Flores, and C. Tejedor, *Phys. Rev. B* **33**, 1814 (1986).
- [36] J. M. Luttinger and J. C. Ward, *Physical Review* **118**, 1417 (1960).
- [37] J. Kondo, *Progress of Theoretical Physics* **32**, 37 (1964).
- [38] J. R. Schrieffer and P. A. Wolff, *Phys. Rev.* **149**, 491 (1966).
- [39] P. W. Anderson, *J. Phys. C* **3**, 2436 (1970).
- [40] K. G. Wilson, *Rev. Mod. Phys.* **47**, 773 (1975).
- [41] H. R. Krishna-murthy, J. W. Wilkins, and K. G. Wilson, *Phys. Rev. B* **21**, 1003 (1980).
- [42] H. R. Krishna-murthy, J. W. Wilkins, and K. G. Wilson, *Phys. Rev. B* **21**, 1044 (1980).
- [43] H. O. Frota and L. N. Oliveira, *Phys. Rev. B* **33**, 7871 (1986).

- [44] O. Sakai, Y. Shimizu, and T. Kasuya, *J. Phys. Soc. Jpn.* **58**, 3666 (1989).
- [45] T. A. Costi and A. C. Hewson, *Physica B Condensed Matter* **163**, 179 (1990).
- [46] T. A. Costi and A. C. Hewson, *Journal of Physics Condensed Matter* **5**, L361 (1993).
- [47] R. Bulla, T. Costi, and T. Pruschke, arXiv:cond-mat/0701105 (2007).
- [48] W. Hofstetter, *Phys. Rev. Lett.* **85**, 1508 (2000).
- [49] R. Bulla, A. C. Hewson, and T. Pruschke, *Journal of Physics Condensed Matter* **10**, 8365 (1998).
- [50] W.-C. Lee and A. H. MacDonald, *Phys. Rev. B* **74**, 075106 (2006).
- [51] S. S. Kancharla and E. Dagotto, *Phys. Rev. B* **74**, 195427 (2006).
- [52] S. Okamoto and A. J. Millis, *Nature* **428**, 630 (2004).
- [53] S. Okamoto and A. J. Millis, *Phys. Rev. B* **72**, 235108 (2005).
- [54] A. Ohtomo, D. A. Muller, J. L. Grazul, and H. Y. Hwang, *Nature* **419**, 378 (2002).
- [55] J. K. Freericks, *Phys. Rev. B* **70**, 195342 (2004).
- [56] T. Oka and N. Nagaosa, *Phys. Rev. Lett.* **95**, 266403 (2005).
- [57] S. Okamoto, *Phys. Rev. B* **76**, 035105 (2007).
- [58] M. Potthoff and W. Nolting, *Phys. Rev. B* **59**, 2549 (1999).
- [59] A. Liebsch, *Phys. Rev. Lett.* **90**, 096401 (2003).
- [60] K. Maiti, P. Mahadevan, and D. D. Sarma, *Phys. Rev. Lett.* **80**, 2885 (1998).
- [61] K. Maiti et al., *Europhys. Lett.* **55**, 246 (2001).
- [62] M. Potthoff, *Phys. Rev. B* **64**, 165114 (2001).
- [63] G. Moeller, Q. Si, G. Kotliar, M. Rozenberg, and D. S. Fisher, *Phys. Rev. Lett.* **74**, 2082 (1995).
- [64] D. S. Fisher, G. Kotliar, and G. Moeller, *Phys. Rev. B* **52**, 17112 (1995).
- [65] X. Y. Zhang, M. J. Rozenberg, and G. Kotliar, *Phys. Rev. Lett.* **70**, 1666 (1993).
- [66] R. Bulla and M. Potthoff, *European Physical Journal B* **13**, 257 (2000).
- [67] F. Schwabl, *Statistical Mechanics*, Statistical Mechanics, by Franz Schwabl. ISBN 3-540-32343-0. Berlin: Springer, 2006., 2006.

- [68] M. Eckstein, M. Kollar, M. Potthoff, and D. Vollhardt, *Phys. Rev. B* **75**, 125103 (2007).
- [69] R. Jamei, S. Kivelson, and B. Spivak, *Phys. Rev. Lett.* **94**, 056805 (2005).
- [70] C. Renner, G. Aeppli, B.-G. Kim, Y.-A. Soh, and S.-W. Cheong, *Nature* **416**, 518 (2002).
- [71] J. Lorenzana, C. Castellani, and C. D. Castro, *Phys. Rev. B* **64**, 235127 (2001).
- [72] A. Liebsch and T. A. Costi, *European Physical Journal B* **51**, 523 (2006).
- [73] W. Ketterle, *Rev. Mod. Phys.* **74**, 1131 (2002).
- [74] E. A. Cornell and C. E. Wieman, *Rev. Mod. Phys.* **74**, 875 (2002).
- [75] C. J. Pethick, H. Smith, and T.-L. Ho, *Physics Today* **56**, 62 (2003).
- [76] M. Greiner, O. Mandel, T. Esslinger, T. W. Hänsch, and I. Bloch, *Nature* **415**, 39 (2002).
- [77] F. Gerbier, S. Foelling, A. Widera, and I. Bloch, *Visibility of a bose-condensed gas released from an optical lattice at finite temperatures*, 2007.
- [78] M. Köhl, H. Moritz, T. Stöferle, K. Günter, and T. Esslinger, *Phys. Rev. Lett.* **94**, 080403 (2005).
- [79] C. A. Regal, M. Greiner, and D. S. Jin, *Phys. Rev. Lett.* **92**, 040403 (2004).
- [80] M. W. Zwierlein et al., *Phys. Rev. Lett.* **92**, 120403 (2004).
- [81] X.-J. Liu, P. D. Drummond, and H. Hu, *Phys. Rev. Lett.* **94**, 136406 (2005).
- [82] M. Rigol, A. Muramatsu, G. G. Batrouni, and R. T. Scalettar, *Phys. Rev. Lett.* **91**, 130403 (2003).
- [83] M. Rigol, R. T. Scalettar, P. Sengupta, and G. G. Batrouni, *Phys. Rev. B* **73**, 121103 (2006).

Danksagung

Prof. Dr. Achim Rosch gilt an dieser Stelle mein ganz besonderer Dank für die Vergabe und Betreuung dieser Arbeit. Sein mitreißender Enthusiasmus für die Physik haben die Zusammenarbeit mit ihm zu etwas Besonderem gemacht. Er war immer ansprechbar und stand jederzeit mit hilfreichen Diskussionen zur Seite. Sein unerschöpfliches Wissen über Physik sowie seine Intuition für physikalische Fragestellungen haben maßgeblich zum Gelingen dieser Arbeit beigetragen.

Bei Dr. Theo Costi bedanke ich mich herzlich für die Betreuung des großen numerischen Anteils dieser Arbeit, sowie für die Bereitstellung seines Quellcodes und das Vermitteln vieler numerischer Tricks.

Bedanken möchte ich mich auch bei Prof. Dr. Matthias Vojta für hilfreiche Diskussionen und die Begutachtung der Arbeit. Prof. Dr. M. Braden danke ich für Übernahme des Prüfungsvorsitzes.

Ebenfalls bedanken möchte ich mich bei Andreas Sindermann, der bei allen Hard- und Softwareproblemen mit Rat und Tat zur Seite stand.

Für die große moralische Unterstützung bedanke ich mich bei den Kellerkindern Fabrizio Anfuso, Benedikt Binz, Ricardo Doretto, Andrej Fischer, Inga Fischer, Markus Garst, Andreas Hackl, Lucas Hollender, Peter Jung, Tobias Lück, Tobias Micklitz, Jan Müller, Jakob Müller-Hill, David Rasch, Tanja Rindler-Daller, Friedmar Schütze, Matthias Sitte, Heidrun Weber, Alexander Wollny und Mario Zacharias. Die äußerst netten und freundschaftlichen Beziehungen im Untergeschoss haben erheblich zum Spaß beim Arbeiten beigetragen.

Bei Alexander Altland bedanke ich mich für seine Motivierung zum Laufen, dank der sich mein Gewicht selbst während der Schlussphase in einem erträglichen Bereich gehalten hat.

Ebenfalls ein ganz besonderer Dank gilt meinen Zimmergenossen Inga Fischer, Theo Costi, Peter Jung und David Rasch für die sehr persönliche und äußerst angenehme Arbeitsatmosphäre im Büro.

Erklärung

Ich versichere, daß ich die von mir vorgelegte Dissertation selbständig angefertigt, die benutzten Quellen und Hilfsmittel vollständig angegeben und die Stellen der Arbeit — einschließlich Tabellen, Karten und Abbildungen, die anderen Werken im Wortlaut oder dem Sinn nach entnommen sind — in jedem Einzelfall als Entlehnung kenntlich gemacht habe; daß diese Dissertation noch keiner anderen Fakultät oder Universität zur Prüfung vorgelegen hat, daß sie — abgesehen von unten angegebenen Teilpublikationen — noch nicht veröffentlicht worden ist sowie, daß ich eine solche Veröffentlichung vor Abschluß des Promotionsverfahrens nicht vornehmen werde. Die Bestimmungen der Promotionsordnung sind mir bekannt. Die von mir vorgelegte Dissertation ist von Herrn Prof. Dr. Achim Rosch betreut worden.

Köln, den 13. November 2007

Teilpublikationen

- P. Jung, R.W. Helmes and A. Rosch, *Transport in Almost Integrable Models: Perturbed Heisenberg Chains*, Phys. Rev. Lett. **96**, 067202 (2006).
- R.W. Helmes, T.A. Costi and A. Rosch, *Mott transition of fermionic atoms in a three-dimensional optical trap*, arXiv:0709.1669(2007).

Lebenslauf

Persönliche Daten

Name	Rolf Walter Helmes
Geburtsdatum	14. Dezember 1977
Geburtsort	Siegen
Familienstand	ledig
Staatsangehörigkeit	deutsch

Schulbildung

1984–1988	Grundschule Daaden
1988–1989	Schulartübergreifende Orientierungsstufe der Geschwister-Scholl-Realschule, Betzdorf
1990–1994	Städtisches Gymnasium am Giersberg, Siegen
1994–1995	Weatherford High School, Texas, U.S.A.
1995–1997	Städtisches Ganztagsgymnasium Siegen
Juni 1997	Abitur

Wehrdienst

Sept. 1997 – Juni 1998	Wehrdienst bei der 19. Kompanie der Technischen Schule der Luftwaffe, Erndtebrück
------------------------	--------------------------------------------------------------------------------------

Hochschulstudium

Oktober 1998	Immatrikulation an der Technischen Universität München Studiengang: Allgemeine Physik (Diplom)
Okt. 2000	Vordiplom
Mai 2004	Diplom
seit Sept. 2004	Anfertigung der vorliegenden Dissertation

Arbeitsverhältnisse

März 2000 - Juli 2000	Werkstudent am Lehrstuhl E17 für Biophysik Analyse von Proteinstrukturen
Nov. 2002 - Dez. 2002	Werkstudent bei Siemens, Materials & Manufacturing, München Abscheidung dünner Schichten, Photolithographische Strukturierung
Oktober 2003–Mai 2004	Wissenschaftliche Hilfskraft am Institut für Theoretische Physik an der Ludwigs-Maximilians-Universität München
seit Sept. 2004	Wissenschaftlicher Mitarbeiter am Institut für Theoretische Physik, Universität zu Köln